

MASTER

Non-Linear Data-Driven Identification of a Peltier-Based Setup

Surie, R.N.

Award date:
2021

[Link to publication](#)

Disclaimer

This document contains a student thesis (bachelor's or master's), as authored by a student at Eindhoven University of Technology. Student theses are made available in the TU/e repository upon obtaining the required degree. The grade received is not published on the document as presented in the repository. The required complexity or quality of research of student theses may vary by program, and the required minimum study period may vary in duration.

General rights

Copyright and moral rights for the publications made accessible in the public portal are retained by the authors and/or other copyright owners and it is a condition of accessing publications that users recognise and abide by the legal requirements associated with these rights.

- Users may download and print one copy of any publication from the public portal for the purpose of private study or research.
- You may not further distribute the material or use it for any profit-making activity or commercial gain



DEPARTMENT OF MECHANICAL ENGINEERING
RESEARCH GROUP: CONTROL SYSTEMS TECHNOLOGY

Non-Linear Data-Driven Identification of a Peltier-Based Setup

MSc. THESIS

R.N. Surie 0810262

Supervisors:

Dr. Ir. D. J. H. Bruijnen^{††}

Dr. Ir. E. Evers[†]

Dr. Ir. R.W. van Gils^{††}

Dr. Ir. J.M.M.G. Noël[†]

Dr. Ir. T.A.E. Oomen[†]

[†] Eindhoven University of Technology - Research Group: Control Systems Technology

^{††} Philips Innovation Services - Mechatronics Department

Eindhoven, January 25, 2021

Preface

This thesis comprises the graduation project of Raoul Surie to fulfill the requirements of the Master's degree in Mechanical Engineering at Eindhoven University of Technology. This work was performed between March 1st 2020 and February 9th 2021 at Philips Innovation Services, Eindhoven. The project was supervised by Rob van Gils, Dennis Bruijnen, Enzo Evers, Jean-Philippe Noël, and Tom Oomen.

With this work nearing completion, so is my time at TU/e. I feel privileged to have been able to study at this amazing university, and to have met some incredible people along the road. I would like to thank a few people in particular. Firstly, my family. Without you, I would not even have dreamt of accomplishing what I have so far. Thank you for your endless support and belief in me. Thank you Tom, for guiding me in my Master, with the choice for an internship in Czech Republic, as well as the graduation project at PInS. Rob, Dennis, Enzo, JP, you all invested many hours of your time to help me. Thank you all for your input and wisdom during this graduation project. Thank you to all my friends, not only for the distractions from my thesis, but also for the many beers and all the adventures we went on over the past years. Lastly, a massive thank you to Armijn. Your unconditional love, positive mindset and calmness gave me the energy to keep going, especially during the challenging times.

Summary

High-precision thermal management applied through thermoelectric coolers, or Peltier elements, has become a field of growing interest in research and development, especially in high-power lighting, semiconductor, and medical fields. Since the thermodynamics of Peltiers are non-affine as function of state and input, identification of the modeling parameters of the Peltier elements is hard, which makes them, combined with the nonlinear thermodynamics present, difficult to control. In thermal control, physics-based modeling is preferred because of project risk reduction, explainability, and tunability of these models. Different methodology than physics-based modeling for estimating the input-output behavior of the plant is data-driven identification. Data-driven models are in general more accurate, but hard to interpret. It is therefore interesting to investigate what modeling performance can be achieved with a data-driven identification of Peltiers, and to compare the resulting models with a physics-based model approach in terms of practical applicability, such as modeling effort or observer design. In this work, a data-driven identification is applied to a Peltier-based setup that consists of two Peltier elements that can be individually actuated. The main objective of this thesis is to perform a data-driven identification on a Peltier-based setup in a temperature range of 5 °C to 80 °C, and to compare the resulting models with a physics-based modeling approach in terms of accuracy, robustness with respect to the ambient temperature, and practical applicability.

To compare both modeling approaches fairly, the most accurate models for both methods, while maintaining a minimal amount of parameters, are obtained. An in-depth analysis on the contribution of the Thomson effect is done on an existing physics-based model of the Peltier-based setup, as well as a sensitivity analysis on the found model parameters. By applying data-driven modeling techniques and using physical insight from the physics-based model, a data-driven model is obtained. Furthermore, inclusion of the ambient temperature in the model structure is considered for various scenarios. After carefully designing a set of multisine experiments, the obtained input-output data is used to estimate a nonparametric best linear approximation in least-squares sense. By using a frequency-domain subspace identification algorithm, a parametric linear model is obtained, after which the quality of the found model is improved by nonlinear optimization. Then, a full nonlinear model is estimated, using a nonlinear search routine.

Concludingly, by performing an in-depth analysis on the contribution of the Thomson effect, the most accurate physics-based model is obtained, while maintaining a minimal amount of parameters. Then, the most accurate data-driven model is obtained, while maintaining a minimal amount of parameters. The input-output behavior is described more accurately for the final data-driven models, while the knowledge on the underlying behavior of the system is lost. Both methods are robust with respect to the ambient temperature, although the interaction between the ambient temperature and the setup cannot be calibrated. If the goal is purely to describe the IO-thermodynamics as accurately as possible, while maintaining a minimal amount of modeling parameters, the data-driven modeling approach can be beneficial for the identification of a thermal system, since these outperform the physics-based model in terms of error margins. The applicability for controller or observer design for these models still needs to be investigated more thoroughly.

Table of Contents

List of Figures	v
List of Tables	vii
1 Introduction	1
1.1 Background & motivation	1
1.2 Objectives & approach	2
1.3 Outline thesis	3
2 Peltier-based setup	5
2.1 Experimental setup	5
2.2 Architecture	7
3 Physics-based model	11
3.1 Physics-based model: overview	11
3.2 In-depth analysis on the contribution of the Thomson effect	13
3.3 Sensitivity analysis physics-based modeling parameters	19
3.4 Conclusion	19
4 Data-driven modeling: methodology	21
4.1 Excitation signal	21
4.2 Nonlinear state-space model structure	21
4.3 Identification procedure	22
4.3.1 Best Linear Approximation	22
4.3.2 Frequency domain subspace identification	24
4.3.3 Nonlinear optimization of the linear model	29
4.3.4 Estimation full nonlinear model	29
4.4 Conclusion	30
5 Data-driven model: results	31
5.1 Excitation signal design	31
5.2 Model structure settings and validation profiles	33
5.2.1 Model structure settings for identification of the Peltier-based setup	34
5.2.2 Validation and test profiles	35
5.3 Best linear approximation & linear model estimation	37
5.3.1 Best linear approximation: SISO	37
5.3.2 Estimation and optimization of a parametric linear model	38
5.4 Resulting U2-SISO nonlinear models	42
5.5 Resulting SD-SISO models	44
5.6 Resulting SD-DC-SISO models	48
5.7 Increasing robustness with respect to the ambient temperature	52
5.7.1 Resulting SD-MISO models	53
5.7.2 Validation method through offline experiments	60
5.8 Conclusion	64
6 Comparison physics-based and data-driven model	67

6.1	Modeling accuracy	67
6.2	Model robustness & interpretability models	70
6.3	Practicability methods	71
6.3.1	Possibility for controller / observer design	71
6.3.2	Modeling effort	72
6.4	Conclusion	73
7	Conclusion & recommendations for future research	74
7.1	Conclusions	74
7.1.1	Obtain the most accurate physics-based & data-driven model, while maintaining a minimal amount of modeling parameters	74
7.1.2	Comparison physics-based & data-driven models	74
7.2	Recommendations	75
	Bibliography	76
	Appendices	80
A	Sensitivity analysis physics-based modeling parameters	80
B	Determination time constant Peltiers	83
B.1	Dominant time constant	83
B.2	Slowest time constant	84

List of Figures

1	A schematic of the Peltier-based setup [39].	5
2	Picture of a L100 Peltier element (left), and a side view of two Peltier elements on top of each other.	6
3	Schematic overview of the architecture of the Peltier-based setup.	7
4	Schematic overview of a Wheatstone bridge circuit [39].	8
5	Linearity of both amplifiers used with the Peltier-based setup.	9
6	Expected current I_{in} versus the measured current I_{out} for both amplifiers of the Peltier-based setup.	10
7	Current error profile for both amplifiers. Original (a), and zoomed-in (b).	10
8	Schematic overview of a Peltier element [39].	11
9	Single Peltier element through which a current flows [46].	14
10	Schematic overview of the Peltier-based setup, (by) courtesy of [39].	17
11	State-space lump division of the Peltier-based setup [39].	18
12	Dedicated experimental setup from [39] to determine temperature dependent modeling parameters.	19
13	Four realizations of the input multisine current profile for Peltier 1 in both time and frequency domain.	33
14	Output for both Peltiers after exciting it with the designed multisine realizations.	33
15	Magnitude of the diagonal elements of the RGA for the Peltier-based setup.	34
16	u_{test} for both Peltiers.	36
17	y_{test} for both Peltiers.	36
18	Nonparametric BLA, the total sample covariance due to stochastic nonlinear contributions and noise, and noise sample covariance for both Peltiers.	38
19	Cost function for (optimized) subspace models for different n and r for Peltier 1. Model order 1 in blue, 2 in orange, 3 in yellow, and 4 in purple. Subspace models are plotted as dots, and optimized models as stars. Stabilized subspace models are encircled in gray, while unstable optimized models are encircled in color.	38
20	Cost function for (optimized) subspace models for different n and r for Peltier 2. Model order 1 in blue, 2 in orange, 3 in yellow, and 4 in purple. Subspace models are plotted as dots, and optimized models as stars. Stabilized subspace models are encircled in gray, while unstable optimized models are encircled in color.	39
21	Zoomed in bottom part of Figure 19, to visualize the optimized models for Peltier 1 more optimal.	39
22	Zoomed in bottom part of Figure 20, to visualize the optimized models for Peltier 2 more optimal.	40
23	Resulting parametric BLA for both Peltiers: SISO.	41
24	Frequency validation for both Peltiers: U2-SISO.	42
25	Time validation MS for both Peltiers: U2-SISO	43
26	Output and errors for MS validation for both Peltiers: U2-SISO.	43
27	Frequency validation for both Peltiers: SD-SISO.	45
28	Time validation MS for both Peltiers: SD-SISO.	46
29	NL error MS validation profile for both Peltiers: SD-SISO.	46

30	Output for test profile for both Peltiers: SD-SISO.	47
31	NL error test profile for both Peltiers: SD-SISO.	47
32	Frequency validation for both Peltiers: SD-DC-SISO.	49
33	Time validation MS for both Peltiers: SD-DC-SISO.	50
34	NL error MS validation profile for both Peltiers: SD-DC-SISO.	50
35	Output for test profile for both Peltiers: SD-DC-SISO.	51
36	NL error test profile for both Peltiers: SD-DC-SISO.	51
37	Nonparametric BLA and its sample covariance for T_{amb} to T_{POI} for both Peltiers: SD-MISO.	53
38	Cost function for (optimized) MISO subspace models for different n and r for Peltier 1. Model order 1 in blue, 2 in orange, 3 in yellow, and 4 in purple. Sub- space models are plotted as dots, and optimized models as stars. Stabilized subspace models are encircled in gray, while unstable optimized models are encircled in color.	54
39	Cost function for (optimized) MISO subspace models for different n and r for Peltier 2. Model order 1 in blue, 2 in orange, 3 in yellow, and 4 in purple. Sub- space models are plotted as dots, and optimized models as stars. Stabilized subspace models are encircled in gray, while unstable optimized models are encircled in color.	54
40	Zoomed in bottom part of Figure 38, to visualize the optimized models for Peltier 1 more optimal.	55
41	Zoomed in bottom part of Figure 39, to visualize the optimized models for Peltier 2 more optimal.	55
42	Resulting parametric linear BLA for both Peltiers: SD-MISO.	56
43	Frequency validation for both Peltiers: SD-MISO.	57
44	Time validation MS for both Peltiers: SD-MISO.	58
45	NL error MS validation profile for both Peltiers: SD-MISO.	58
46	Output for test profile for both Peltiers: SD-MISO.	59
47	NL error test profile for both Peltiers: SD-MISO.	59
48	Frequency validation and time validation on MS validation profile for Peltier 1: SD-MISO-OFFLINE.	61
49	NL error for MS validation profile for Peltier 1: SD-MISO-OFFLINE.	62
50	Measured output (grey), linear model output (blue), and nonlinear SD-MISO- OFFLINE model output (green) for test profiles #1 and #2.	62
51	Measured output (grey), linear model output (blue), and nonlinear SD-MISO- OFFLINE model output (green) for test profiles #3 and #4.	63
52	Nonlinear error for the SD-MISO-OFFLINE model for test profiles #1 and #2.	63
53	Nonlinear error for the SD-MISO-OFFLINE model for test profiles #3 and #4.	63
54	Validation on temperature profile for the physics-based model for both Peltiers. The top part shows the experimental output (solid), model output (dashed), and the bottom part shows the corresponding error.	68
55	Validation on temperature profile for the SD-MISO model for both Peltiers. The top part shows the experimental output (solid), model output (dashed), and the bottom part shows the corresponding error.	69
56	Simulated output with original parameters.	80
57	Sensitivity analysis w.r.t. K_M for Peltier 1.	81
58	Sensitivity analysis w.r.t. R_M for Peltier 1.	81

59	Sensitivity analysis w.r.t. S_M for Peltier 1.	81
60	Error of simulated model for both original and deviated parameters for sensitivity analysis.	82
61	Step response of both Peltiers in the Peltier-based setup.	83
62	Step response of both Peltiers in the Peltier-based setup, zoomed.	83
63	Step responses used to determine slowest time-constants of Peltier 1 and 2. . .	84

List of Tables

1	Limit values of the experimental setup Peltiers.	6
2	Natural frequencies and damping of the poles of the resulting parametric models of both Peltier 1 and Peltier 2.	41
3	Error margins for SD-SISO model for P1.	48
4	Error margins for SD-SISO model for P2.	48
5	Error margins for SD-DC-SISO model for P1.	52
6	Error margins for SD-DC-SISO model for P2.	52
7	Error margins for SD-MISO model for P1.	60
8	Error margins for SD-MISO model for P2.	60
9	Error margins for SD-MISO offline model: MS, validation profile #1 and #2.	64
10	Error margins for SD-MISO offline model: validation profile #3 and #4.	64
11	Error margins for all data-driven models for both the validation profile and the test profile for Peltier 1.	65
12	Error margins for all data-driven models for both the validation profile and the test profile for Peltier 2.	65
13	Error margins for both the physics-based and the SD-MISO data-driven models for the temperature profile for both Peltiers.	69

1 Introduction

1.1 Background & motivation

High-precision thermal management has become a field of growing interest in research and development, especially in high-power lighting, semiconductor, and medical fields. From societal demands, extensive research on obtaining the best performance possible continues, therewith complicating mechatronic devices every year. In the medical field, the challenges can range from developing new diagnostics platforms for common diseases throughout the world [44] to designing handheld devices for diagnosing extremely small fluid volumes (for example saliva, blood), where thermal devices are used to perform a genetic amplification technique [18]. Furthermore, thermal control is a critical aspect in the mechatronic design for semiconductor mass production, to achieve a positioning accuracy of nanometres [4]. Also, light-emitting diodes (LEDs) have been gaining increasing interest as light sources. LED performance in light output, light quality, and lifetime all suffer from an increase in temperature. Therefore, there has been a growing need to actively control high-power LED lighting, to maintain correct light quality and expected lifetime [19].

Thermoelectric coolers (TECs) have become increasingly popular in thermal control, because of their compact dimensions, capability to both heat and cool, and lack of moving parts. Still, TECs are sensitive to mechanical stresses and power inefficient. However, by mechanical design principles, the mechanical stresses can be reduced, and the power inefficiency is of less essence, as the maximum cooling capacity is below 100 Watt. A synonym for TECs is Peltier elements, or in short ‘Peltiers’, because of the Peltier effect causing the heat transfer within these elements. By electrically connecting N- and P-type semiconductors in series, and applying a direct current (DC) through the element, heat is pumped from one side to the other. The direction of the DC determines the cooling direction. Since the thermodynamics of Peltiers are non-affine as function of state and input, identification of the modeling parameters of the Peltier elements is hard, which makes them, combined with the nonlinear thermodynamics present, difficult to control.

A wide variety of studies has investigated identification and thermal control of Peltier elements [7][10][11][18][21][39][47][48]. Most thermal control focuses on the cold side of the Peltier elements. Furthermore, the usage of (switching) PID controllers is common, because of its simplicity in design and implementation [21], but is not robust [18]. In [11], a static identification method for the Peltier parameters is applied and a generic input-output (IO) linearizing feedback law is used, taking the practical limitations of the used setup into account. The work in [11] is extended in [39] by including the temperature-dependency of the model parameters. Temperature-dependency of Peltiers is not necessarily taken into account for thermal modeling. In [45][46], it is stated that it is important and necessary to take the temperature-dependency of thermoelectric (TE) materials into account when designing high-performance TE modules for $-13\text{ }^{\circ}\text{C} \leq T \leq 67\text{ }^{\circ}\text{C}$. In thermal control, physics-based modeling is preferred because of project risk reduction, the explainability, and tunability of these models.

Different methodology than physics-based modeling for estimating the input-output behavior of the plant is data-driven identification, or black-box modeling. Black-box modeling

implies the application of a model structure that is as flexible as possible, since no information about the internal structure of the device is utilized [31]. However, physical structures of physics-based models (also referred to as white-box modeling approach) provide some guidance in choosing structures and designs of experiments [43]. In [29], a grey-box identification method is used, where the amount of nonlinear basis functions used is limited, based on physical insights. The compromise between capturing complex nonlinearities of the fitted model and the ability to possess a low number of parameters is one of the challenges in data-driven identification techniques [29].

Modeling systems with physical laws is often too time consuming, because of so many small parts and their interactions, while in practice, for many purposes, such as control, a mathematical model properly describing the input-output dynamics suffices [43]. It is therefore interesting to investigate what modeling performance can be achieved with a data-driven identification of Peltiers, and to compare it with the physics-based modeling approach in terms of complexity and accuracy. This thesis aims to do so with a Peltier-based setup, built to investigate the thermodynamics of Peltier elements.

1.2 Objectives & approach

As systems and their interactions are often too time consuming to model with physical laws and properly describing the IO-dynamics suffices [43], it is worthwhile to investigate a data-driven approach for the Peltier-based setup researched in [11][39] as well. In order to obtain the IO-thermodynamics, a nonlinear data-driven modeling approach will be utilized. Therefore, the only information of the internal structure of the setup that will be used, is the fact that the nonlinearities are, according to the physics-based model, of a certain order. This is done to apply a model structure that is as flexible as possible [31], while utilizing the available knowledge.

The question then arises whether a data-driven modeling approach will be able to capture the setup thermodynamics better or worse than a physics-based model. It is also interesting to investigate whether the data-driven approach can be of use in practice, to aid in product analysis for example. Furthermore, the data-driven modeling approach might result in a model with states that are non-interpretable, but describe the IO-thermodynamics very well. The possibilities for observer design, feedback linearization or controlling the setup, like done for the physics-based model in [11][39] are alluring to research as well. These questions are all incorporated into the research question.

Research question: *To what extent can nonlinear data-driven identification aid with or be used solely for the identification of a Peltier-based setup?*

This research question has been divided into separate research objectives.

Research objectives

1. *Obtain the most accurate physics-based model & data-driven model, while maintaining a minimal amount of modeling parameters*

To eventually make a fair comparison between the two methods, the most accurate models for both methods, while maintaining a minimal amount of modeling parameters, are needed.

Perform an in-depth analysis on the contribution of the Thomson effect

The physics-based model obtained in [39] excluded the Thomson effect, based on [14]. One of the recommendations of [39] was to investigate the Thomson effect in more detail in future research on Peltiers, since its effect is probably larger than claimed in [14]. Therefore, an in-depth analysis on the contribution of the Thomson effect is done.

Obtain the data-driven model

In order to obtain a nonlinear data-driven model, the approach from [29] is used, utilizing the work from [31],[25], and [35]. Following [29], a proper model structure is chosen. Then, using the methodology from [31], a nonparametric best linear approximation in a mean square sense is determined from the experimental data. Utilizing this approximation, a parametric linear model is estimated, using the frequency domain subspace identification algorithm from [25], while employing the sample covariance matrix instead of the true covariance, as presented in [35]. The quality of the found parametric linear models is improved by nonlinear optimization, after which a full nonlinear model is estimated.

2. *Develop a fair comparison of the data-driven identification vs. the physics-based model for the Peltier-based setup*

In thermal control, physics-based modeling is preferred because of project risk reduction, the explainability, and tunability of these models. Black-box models are in general more accurate, but hard or impossible to interpret [33]. In order to get a fair comparison between both models, several aspects need to be compared.

Comparison physics-based & data-driven: accuracy & robustness

For both models, the accuracy will be compared in terms of the modeling error. To do so, the modeled output is compared with the experimental output for a validation trajectory that resembles a typical temperature profile for the Peltier to follow when used in handheld devices like in [18], and covers most of the operating temperature range. In order for a model of the Peltier-based setup to be of use in practice, it needs to be robust with respect to the ambient temperature. The robustness is checked by analyzing the knowledge of the found models on the ambient temperature.

Comparison physics-based & data-driven: model complexity & method practicability

If a modeling procedure is really complex, it will not be used in practice, unless the obtained accuracy improves drastically. Both methods are compared in terms of easy adaptation to identify different types of TECs by analyzing the amount of work needed to identify a different (type of) Peltier.

1.3 Outline thesis

This thesis consists of 7 chapters. The Peltier-based setup is introduced in Chapter 2. The research objectives described in Section 1.2 and the methods to achieve these will be treated

in Chapters 3 to 6. Conclusions and recommendations for future research will be given in Chapter 7.

In Chapter 2 the Peltier-based setup is introduced. The hardware and the specifications that need to be considered for identification of the setup are discussed. Then, Chapter 3 introduces the physics-based model found in [39] and gives an in-depth analysis on the contribution of the Thomson effect as well as a sensitivity analysis of the Peltier device parameters. The final physics-based model is used for the comparison with the data-driven model. Next, in Chapter 4, the methodology on how to obtain a nonlinear data-driven model for a thermal system is discussed. The methodology is used to construct the data-driven model of the Peltier-based setup in Chapter 5. Subsequently, Chapter 6 compares the resulting data-driven models obtained for the Peltier-based setup with the physics-based model from [39]. Finally, Chapter 7 gives an overview of conclusions of this work, and lists the recommendations for future research.

2 Peltier-based setup

In this chapter the Peltier-based setup is introduced. The hardware and the specifications that need to be considered for identification of the setup are discussed. In Section 2.1 the components of the experimental setup are given. In Section 2.2 the architecture of the setup is described in terms of data acquisition platform, sensors, amplifiers, and current control.

2.1 Experimental setup

Previous research within Philips Innovation Services (PInS) [11] focused on building a Peltier-based experimental setup to investigate the thermodynamics of Peltier elements. The setup represents a simplified diagnostic platform used to investigate different control strategies [11][39]. A schematic overview of this setup is given in Figure 1.

Peltier elements are used in a variety of temperature ranges, differing per application. The focus of this research lies in controlling both Peltiers individually, since in diagnostic platforms where fluid samples are processed by sequential heating and cooling, multiple Peltiers, although thermally coupled, still require individual temperature control. For this setup, a temperature range from 5 °C to 90 °C is relevant, therefore including the majority of applications.

Two individually actuated Peltier elements are thermally coupled by a stainless steel bottom plate. To reduce complexity of the setup, this plate is used for temperature control instead of using real fluid volumes. The hot sides of the Peltiers are connected by an aluminum top plate, which are thermally conditioned with an actively fanned heat sink (note that when the bottom temperature rises quickly, the top temperature drops, resulting in the heat sink briefly heating the Peltier instead of cooling). The objective is to thermally control both points of interest (POI) on the bottom plate. The setup has previously been modelled using a physics-based modelling approach.

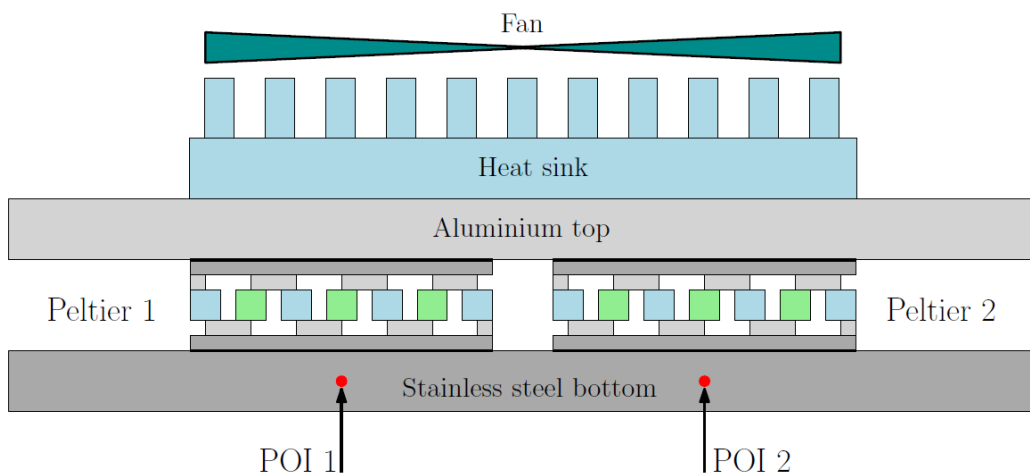
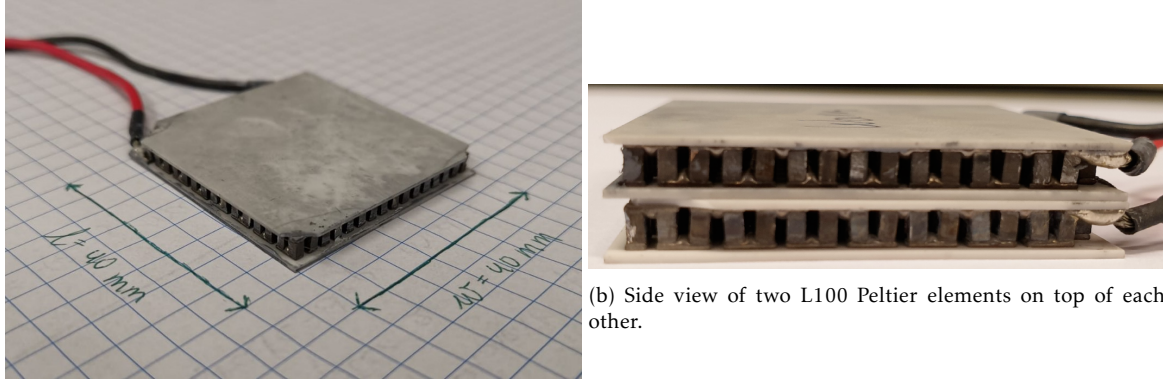


Figure 1: A schematic of the Peltier-based setup [39].

Two Peltier elements are at the core of this setup. When applying a current to them, heat is transferred from one side to the other. The amount of heat transferred depends on the type of Peltier element. A Peltier element of type L100 is provided in Figure 2a, and Figure 2b shows the side view of two Peltier elements on top of each other. The width and length of this L100 Peltier element are both equal to 40 mm and it is 5 mm in height. The side view shows the difference in pellets and solder due to the production process.



(a) Picture of a L100 Peltier element.

Figure 2: Picture of a L100 Peltier element (left), and a side view of two Peltier elements on top of each other.

Other specifications of a Peltier element are the maximum temperature T_{\max} , the maximum heat difference ΔT_{\max} , occurring at the maximum current I_{\max} , and the maximum amount of heat that can be transported from the cold side to the hot side Q_{\max} , when $\Delta T = 0$ and $I = I_{\max}$.

Throughout this research, two different types of Peltiers have been used. The first type is the same as used in [39] for the physics-based model. This was assumed to be the L100 type, but throughout this research it was found that this is not the case. The true type of these Peltier elements is unknown. For the remainder of this thesis, it will be referred to as TEC-[39]. The latter type of Peltier element is of the type L100. The L100 Peltiers are used for the data-driven identification in Chapter 5. The limit values for both types of Peltier elements are given in Table 1.

	L100 [9]	TEC-[39]
T_{\max} [°C]	95	90
ΔT_{\max} [°C]	75	70
I_{\max} [A]	4.1	3.3
Q_{\max} [W]	39	29.3

Table 1: Limit values of the experimental setup Peltiers.

2.2 Architecture

The architecture of the Peltier-based setup is depicted in Figure 3. It consists of a Windows-based PC running Matlab Simulink, a data acquisition platform, two electrical amplifiers, two Peltier elements, two passive resistors, thermocouples, NTCs and Wheatstone bridges.

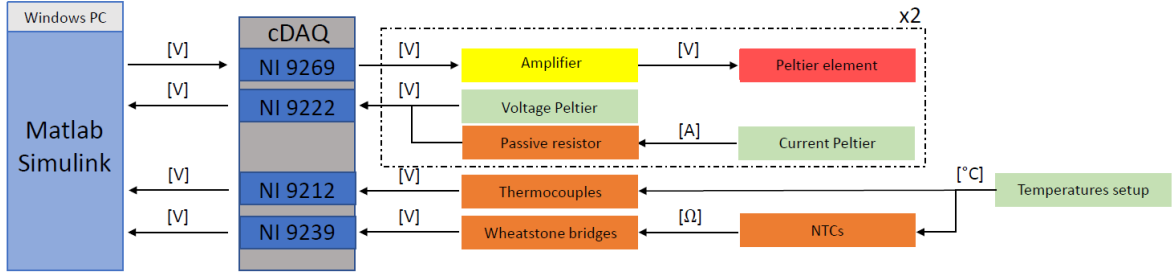


Figure 3: Schematic overview of the architecture of the Peltier-based setup.

Data acquisition platform

The sensor measurements and controlling the amplifiers is done by using a CompactDAQ (cDAQ) platform from National Instruments with 8 modules for either input or output. The different modules used can be found in Figure 3. The cDAQ is read by a Windows-based PC running Matlab Simulink. The cDAQ and Simulink communicate via PInS in-house developed software. Since the internal clock of the cDAQ is used for equidistant time sampling, Simulink can be simply run by a single simulation Simulink license (no real-time license required).

Temperature sensors

Temperatures are measured with 8 thermocouples (TC) sensors and 4 thermistors with a negative temperature coefficient (NTC) sensors. The relative accuracy of the TC and NTC sensors has been estimated in [39], resulting in a relative error with respect to a zero point of ± 0.1 °C for the TC sensors, and ± 0.05 °C for the NTC sensors. Both the TCs and NTCs are sampled at 10 Hz.

Wheatstone bridge

In order to determine the resistance of the NTC sensors a Wheatstone bridge is used, related to the measured temperature by the Steinhart-Hart relation [40]. Figure 4 shows the electrical circuit of a Wheatstone bridge, consisting of a constant input voltage V_{in} of 5 V, which is measured in the setup as well, output voltage V_{out} [V], measured by the cDAQ, constant resistors R_1 , R_2 , and R_3 of 10 k Ω , and the variable NTC resistance R_t [Ω].

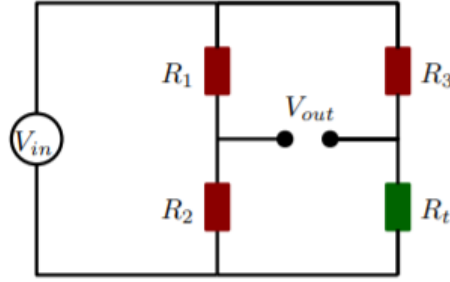


Figure 4: Schematic overview of a Wheatstone bridge circuit [39].

In this way the voltage difference over the Wheatstone bridge is equal to

$$V_{out} = \left(\frac{R_2}{R_1 + R_2} - \frac{R_t}{R_t + R_3} \right) V_{in}. \quad (1)$$

The resistances R_{1-3} are not exactly $10 \text{ k}\Omega$, and therefore were calibrated, according to the procedure described in Appendix A of [39].

Electrical current sensors

To measure the applied current to the Peltier elements, a passive resistor is used in series with each Peltier element. By measuring the voltage drop over the resistor and applying Ohms law, the current is determined. A passive resistor R_p of type WH50-2RJI with a resistance of $2.2 \text{ }\Omega$ is used so the current can be directly measured without an operational amplifier. The NI 9222 module of the cDAQ can measure a voltage from -10 V to 10 V , which corresponds to a current ranging from -4.54 A to 4.54 A .

Electrical current amplifiers

Both Peltiers in the Peltier-based setup are actuated individually by sending a voltage signal to a linear amplifier. These voltages V_{in} are converted into currents I_{out} , which are then sent to the Peltiers. The type TA115 amplifier output ranges from $-4\text{A} \leq I_{out} \leq 4\text{A}$, where the input ranges from $-10 \text{ V} \leq I_{in} \leq 10\text{V}$. The amplifier gain K_P therefore is expected to be 0.4 A per V .

Current control

Since the linear amplifiers are required to be used in closed loop, the amplifier gain slightly differs over its power range. To correct for the error in amplifier gain, a proportional–integral (PI) controller is used. In order to investigate the linear relation for the amplifiers, as well as the differences in proportional gain K_P over the power range, a stairs signal for V_{in} ranging from -6 V to 6 V has been applied, while measuring the output I_{out} . A linear function is fitted through the found data, and is given in Figure 5.

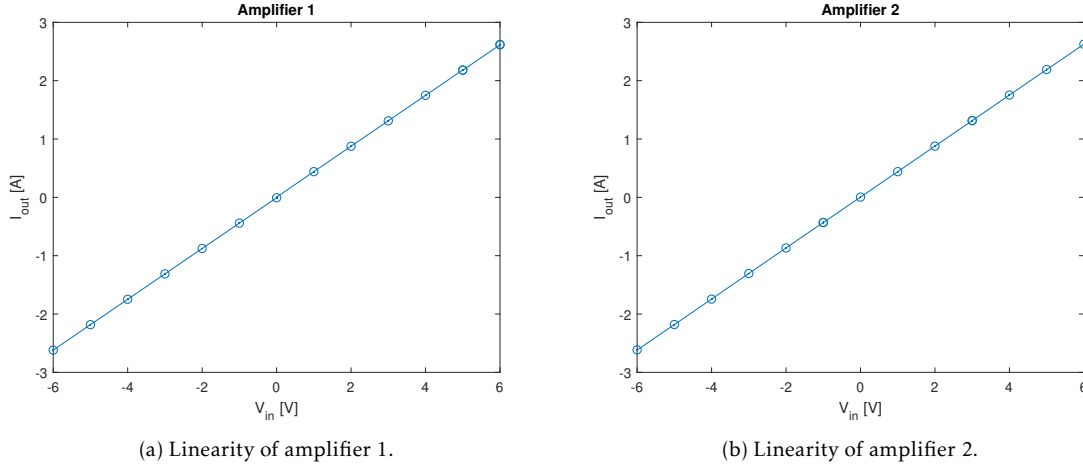


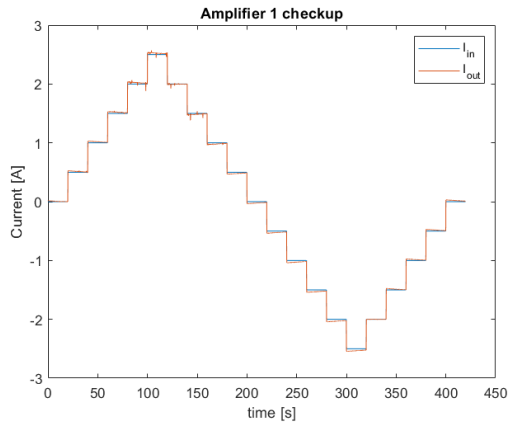
Figure 5: Linearity of both amplifiers used with the Peltier-based setup.

Figure 5 shows that the proportional gain is linear and consistent for the range of interest. In [39] it was already found that the power supply for the amplifiers has inadequate power for $-6 \text{ V} > V_{\text{in}} > 6 \text{ V}$ for the amplifiers. After analysis of the data from this experiment it can be concluded that this is indeed the case.

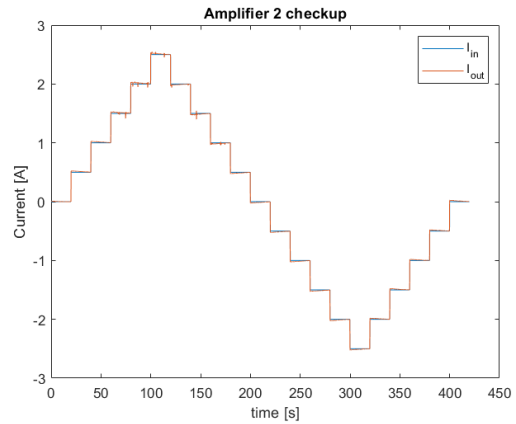
To limit the integral action, a saturation function is used, only removing offset close to the reference setpoint. The saturated integral gain K_I was tuned using experimental data. The PI-controller is implemented and validated in [39].

Another experiment is conducted to investigate the amplifiers more thoroughly. Figure 6 shows the expected current I_{in} versus the measured current I_{out} for both amplifiers, when applying a stairstep profile in steps of 0.5A, in the range $-2.5 \text{ A} \leq I_{\text{in}} \leq 2.5 \text{ A}$. The current error profile for both amplifiers, defined as $I_{\text{out}} - I_{\text{in}}$, is provided in Figure 7. It is clear to see from Figure 6 that both amplifiers have a mismatch in behavior when $I_{\text{in}} \geq 2 \text{ A}$, where I_{in} equals the input voltage V_{in} [V] multiplied with the amplifier gain K_p . This is then compared with the output I_{out} , which is the output voltage measured [V] divided by the passive resistance value R_p [Ω]. It is therefore decided that the maximum allowed I_{in} for both amplifiers is set to 2 A instead of 4 A, as described by the amplifier specifications.

Furthermore, the cause for the small spikes in the I_{out} profiles in Figures 6a and 6b is unknown, and should be investigated in the future. The large peaks in the error profiles in Figure 7a are caused by delay between reference current and measured current, and are part of the plant thermodynamics. Figure 7b shows that during smooth trajectories, the current error is below 0.015 A.

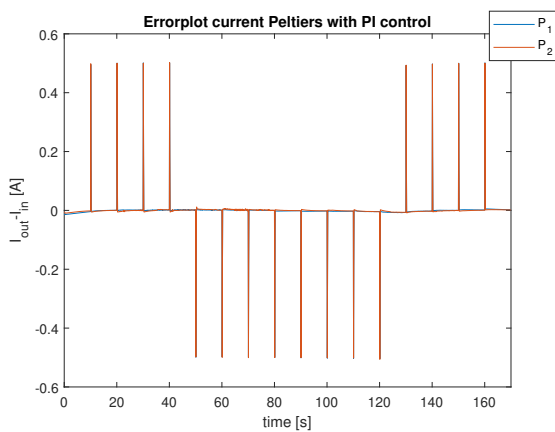


(a) Amplifier 1.

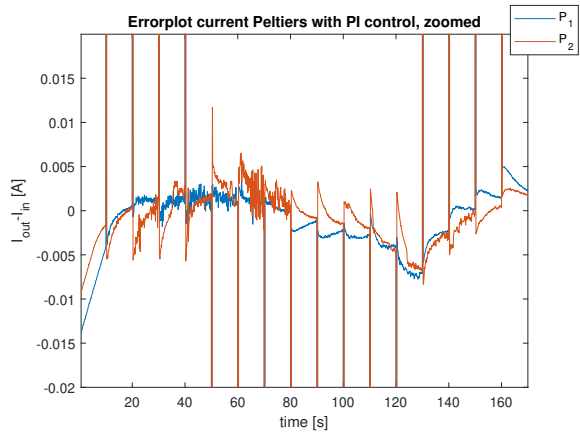


(b) Amplifier 2.

Figure 6: Expected current I_{in} versus the measured current I_{out} for both amplifiers of the Peltier-based setup.



(a) Current error I_{in} minus I_{out} for both amplifiers.



(b) Zoomed-in part of the current error plot in Figure 7a for both amplifiers.

Figure 7: Current error profile for both amplifiers. Original (a), and zoomed-in (b).

For the data-driven identification and validation, only amplifier 2 has been used. Multiple Peltiers of type TEC-[39] broke during testing, and amplifier 1 is believed to be the cause. In order to prevent more broken Peltiers, only amplifier 2 has been used in the remainder of the research. The precise reason for this mismatch in amplifier behavior has not been investigated in this research. In order to use the setup to its full extent, it is recommended for PINs to investigate this issue in the future.

3 Physics-based model

In this chapter the physics-based model is discussed. Firstly, the physics-based model constructed in [39] is introduced in 3.1. Then, an in-depth analysis on the contribution of the Thomson effect is given in Section 3.2. Next, a sensitivity analysis on the found model parameters is provided in Section 3.3. Concluding, it is discussed whether the most optimal physics-based model to compare with the data-driven model is obtained.

3.1 Physics-based model: overview

In order to do an in-depth analysis on the contribution of the Thomson effect on the physics-based model from [39], the modeling procedure, and therefore the physics of the setup itself, need to be understood. A Peltier element consists of electrically in series, thermally in parallel connected semiconductors of type N and P. Its thermodynamics are described by thermal and electrical effects. When an electrical power P_{in} [W] is applied to it, it transfers heat from one side to another. A schematic overview of a Peltier element is depicted in Figure 8.

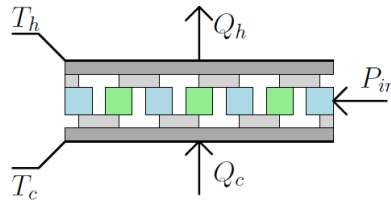


Figure 8: Schematic overview of a Peltier element [39].

Whether the Peltier element heats or cools, depends on the direction of the current. In Figure 8, it absorbs heat Q_c [J] at the cold side, and transfers heat Q_h [J] to the hot side. This configuration will be considered for the composition of the equations in this chapter.

The heat transfer dynamics depend on the amount of applied electrical power P_{in} . In steady-state, the energy balance is

$$P_{in} = Q_h - Q_c, \quad (2)$$

where $\dot{T} = 0$. The energy balance is described by four thermal/electrical effects: the Seebeck/Peltier effect, the Joule effect, the Fourier effect, and the Thomson effect.

The **Seebeck/Peltier effect** can be described in two different ways, known as the Seebeck and Peltier effect respectively. According to the first way, known as the Seebeck effect, the Seebeck effect generates a electric power P_{out} [W] due to a difference in temperature between the hot and cold side of the Peltier element. Connecting two dissimilar conductors in series and maintaining them at different temperatures generates an electric power caused by an electromotive force V_{S_M} [V]. This electric power is generated because of the Seebeck effect, and equals

$$P_{S_M} = V_{S_M} I = S_M(T_{AVG})(T_h - T_c)I, \quad (3)$$

with P_{S_M} the power due to the Seebeck/Peltier effect [W], $T_{AVG} = \frac{1}{2}(T_h + T_c)$ the average pellet temperature [K], T_h the hot side temperature [K], T_c the cold side temperature [K], $S_M(T_{AVG})$ the Seebeck coefficient [V/K] depending on T_{AVG} [K], and I the electrical current supplied to the Peltier element [A]. The second way, known as the Peltier effect, is the Seebeck effect reversed. Applying an electrical power P_{in} [W] to the Peltier element results in a generated heat flow. This heat flow, generated by the Peltier effect, is equal to

$$Q_P(T) = S_M(T_{AVG})TI, \quad (4)$$

with Q_P the rate of heat flow due to the Seebeck/Peltier effect [W], and $T \in \{T_c, T_h\}$ [°C]. The Seebeck effect thus generates electrical power equal to the net heat flow generated by the Peltier effect. The Seebeck/Peltier effect is therefore described by

$$P_{S_M} = Q_P(T_h) - Q_P(T_c). \quad (5)$$

The **Joule effect** generates heat when an electrical current runs through a conductor. The applied electrical power is equal to the generated heat dissipation Q_J [W] and is described by

$$P_{R_M} = Q_J = R_M(T_{AVG})I^2, \quad (6)$$

with P_{R_M} the power due to the Joule effect [W], Q_J the rate of heat flow due to the Joule effect [W], and $R_M(T_{AVG})$ the electrical resistance [Ω], depending on T_{AVG} .

The **Fourier effect** is the conductive heat transfer from hot to cold side of the Peltier element, described by

$$Q_F = K_M(T_{AVG})(T_h - T_c), \quad (7)$$

with Q_F the rate of heat flow due to the Fourier effect, and $K_M(T_{AVG})$ the thermal conductance of a Peltier element [W/K] depending on T_{AVG} . The dimensions and thermal conductivity of the pellets and ceramic plates determine the thermal conductance of a Peltier element.

The **Thomson effect** generates additional heating or cooling when an electrical current flows in the direction of the temperature gradient in a homogeneous conductor. The heat flow caused by this effect is equal to

$$Q_T = \tau I(T_h - T_c), \quad (8)$$

where τ is the Thomson coefficient [V/K].

The Thomson effect was omitted in [39] based on [14], and it was recommended to investigate the effect of its inclusion on the modeling results. This is done in Section 3.2.

Combining (3)-(7), the energy balance of (2) can be completed. The electrical power P_{in} applied to a Peltier element is described by

$$P_{in} = P_{R_M} + P_{S_M} = R_M(T_{AVG})I^2 + S_M(T_{AVG})(T_h - T_c)I. \quad (9)$$

Applying this electrical power results in the rate of heat transfer absorbed at the cold side Q_c given by

$$Q_c = Q_P - \frac{1}{2}Q_J - Q_F = S_M(T_{AVG})T_c I - \frac{1}{2}R_M(T_{AVG})I^2 - K_M(T_{AVG})(T_h - T_c), \quad (10)$$

and in a rate of heat transfer dumped at the hot side Q_h , given by

$$Q_h = Q_P + \frac{1}{2}Q_J - Q_F = S_M(T_{AVG})T_h I + \frac{1}{2}R_M(T_{AVG})I^2 - K_M(T_{AVG})(T_h - T_c). \quad (11)$$

It is assumed that the heat generated by the Joule effect is equally divided between the cold and hot heat flow, commonly done in Peltier thermodynamical modelling [5] [13].

3.2 In-depth analysis on the contribution of the Thomson effect

It was recommended in [39] to investigate the effect of the incorporation of the Thomson effect in the the physics-based model.

The Thomson coefficient is related to the Seebeck coefficient through the Kelvin relationship

$$\tau = \frac{dS_m}{dT}T. \quad (12)$$

Using [5], where it is assumed that the Thomson effect is equally distributed over the cold and the hot side, the differential equations (DEs) for a single Peltier are given as

$$m_c c_{p,c} \dot{T}_c = S_m(T_{AVG})T_c I - \frac{1}{2}R_M(T_{AVG})I^2 + \frac{1}{2}\tau(T_{AVG})I(T_h - T_c) - K_M(T_{AVG})(T_h - T_c), \quad (13)$$

with m_c the mass on the cold side, $c_{p,c}$ the specific heat capacity on the cold side, and

$$m_h c_{p,h} \dot{T}_h = S_m(T_{AVG})T_h I + \frac{1}{2}R_M(T_{AVG})I^2 - \frac{1}{2}\tau(T_{AVG})I(T_h - T_c) - K_M(T_{AVG})(T_h - T_c), \quad (14)$$

with m_h the mass on the hot side, $c_{p,h}$ the specific heat capacity on the hot side.

In [39], temperature dependent parameters S_M and R_M are identified by applying a step in current on a single Peltier, and taking advantage of the fast electrical and slow thermal behavior. Using (2), the applied electrical power P_{in} is equal to

$$P_{in} = Q_h - Q_c = m_h c_{p,h} \dot{T}_h - m_c c_{p,c} \dot{T}_c. \quad (15)$$

Filling in (13) and (14) gives

$$P_{in} = (S_M(T_{AVG}) - \tau(T_{AVG}))I(T_h - T_c) + R_M(T_{AVG})I^2. \quad (16)$$

By rewriting (16) using Ohms law, the voltage over the Peltier element V_P [V] is described by

$$V_P = V_{R_M} + V_{S_M} = (S_M(T_{AVG}) - \tau(T_{AVG}))(T_h - T_c) + R_M(T_{AVG})I, \quad (17)$$

with V_{R_M} the voltage due to the Joule effect [V], and V_{S_M} the voltage due to the Seebeck/Peltier effect [V]. By utilizing the fast electrical and slow thermal behavior, the electrical resistance, Seebeck coefficient and Thomson coefficient can be determined with

$$R_M(T_{AVG}) = \frac{V_{R_M}}{\delta I}, \quad (18)$$

$$S_M(T_{AVG}) - \tau(T_{AVG}) = \frac{V_{S_M}}{\bar{T}}, \quad (19)$$

with δI a step in current, and \bar{T} the average temperature during the steady-state period. Using

$$\tau = \frac{dS_M}{dT} T, \quad (20)$$

this would result in $S_M(T_{AVG})$ obtained in [39] to be equal to $S_M(T_{AVG}) - \tau(T_{AVG})$.

In [46], it is claimed that if the Seebeck coefficient for a TEC can be expressed as a function of T_{AVG} and T_{AVG}^2 , it can be transformed into a Seebeck coefficient evaluated at both the hot and the cold side. Consider the Peltier element shown in Figure 9. The heat rate equations for the hot and cold side respectively are given as

$$Q_h = S_M(T_h)T_h I - \frac{1}{2}\tau I \Delta T + \frac{1}{2}I^2 R_M - K_M \Delta T, \quad (21)$$

$$Q_c = S_M(T_c)T_c I + \frac{1}{2}\tau I \Delta T - \frac{1}{2}I^2 R_M - K_M \Delta T, \quad (22)$$

with Q_h the transferred heat to the hot junction of the Peltier [W], Q_c the absorbed heat at the cold junction of the Peltier [W], and $\Delta T = T_h - T_c$.

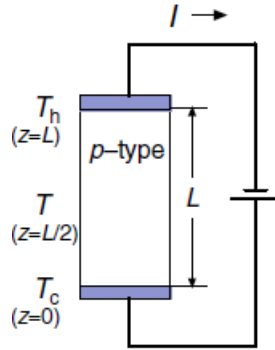


Figure 9: Single Peltier element through which a current flows [46].

Combining the first and second term of (21) and (22) gives

$$Q_h = \sigma_h T_h I + \frac{1}{2}I^2 R_M - K_M \Delta T, \quad (23)$$

with

$$\sigma_h = S_M(T_h) - \frac{\tau(T_h)\Delta T}{2T_h}, \quad (24)$$

and

$$Q_c = \sigma_c T_c I - \frac{1}{2} I^2 R_M - K_M \Delta T, \quad (25)$$

with

$$\sigma_c = S_M(T_c) + \frac{\tau(T_c)\Delta T}{2T_c}. \quad (26)$$

Assuming a linear temperature distribution in the pellet (which is accurate in steady-state), the temperature along the length of the Peltier can be expressed as a function of $z \in \{0, L\}$

$$T_z = T + \left(z - \frac{L}{2}\right) \frac{\Delta T}{L}, \quad (27)$$

where $T_z(z = L)$ corresponds to T_h , $T_z(z = 0)$ corresponds to T_c , and $T_z(z = L/2)$ corresponds to T . When S_M is expressed as a quadratic function of temperature, $S_M(T_z)$ can be expanded in a power series and therefore written as

$$S_M(T_z) = S_M(T) [1 + A_1(T_z - T) + A_2(T_z - T)^2], \quad (28)$$

with A_1 and A_2 the expansion coefficients of $S_M(T_z)$. Now, $S_M(T_h)$ can be determined as

$$S_M(T_z)|_{T_z=T_h} = S_M(T) [1 + A_1(T_h - T) + A_2(T_h - T)^2], \quad (29)$$

$$S_M(T_h) = S_M(T) \left[1 + A_1 \left(T_h - \frac{T_h + T_c}{2} \right) + A_2 \left(T_h - \frac{T_h + T_c}{2} \right)^2 \right], \quad (30)$$

$$S_M(T_h) = S_M(T) \left[1 + A_1 \left(\frac{T_h - T_c}{2} \right) + A_2 \left(\frac{T_h - T_c}{2} \right)^2 \right], \quad (31)$$

$$S_M(T_h) = S_M(T) \left[1 + \frac{A_1}{2} \Delta T + \frac{A_2}{4} (\Delta T)^2 \right]. \quad (32)$$

In a similar way, $S_M(T_c)$ can be determined as

$$S_M(T_z)|_{T_z=T_c} = S_M(T) [1 + A_1(T_c - T) + A_2(T_c - T)^2], \quad (33)$$

$$S_M(T_c) = S_M(T) \left[1 - \frac{A_1}{2} \Delta T + \frac{A_2}{4} (\Delta T)^2 \right]. \quad (34)$$

Following up on this, the Thomson coefficients can be determined for the hot side as

$$\tau(T_h) = T_h \frac{dS_M(T_z)}{dT_z} \Big|_{T_z=T_h} = T_h \frac{d}{dT_z} \left(S_M(T) [1 + (T_z - T)A_1 + (T_z - T)^2 A_2] \right) \Big|_{T_z=T_h}, \quad (35)$$

$$\tau(T_h) = T_h (S_M(T) [A_1 + (2T_h - 2T)A_2]), \quad (36)$$

$$\tau(T_h) = T_h \left(S_M(T) \left[A_1 + (2T_h - 2 \frac{T_h + T_c}{2}) A_2 \right] \right), \quad (37)$$

$$\tau(T_h) = T_h S_M(T) [A_1 + \Delta T A_2], \quad (38)$$

and for the cold side as

$$\tau(T_c) = T_c \frac{dS_M(T_z)}{dT_z} \Big|_{T_z=T_c} = T_c \frac{d}{dT_z} \left(S_M(T) \left[1 + (T_z - T)A_1 + (T_z - T)^2 A_2 \right] \right) \Big|_{T_z=T_c}, \quad (39)$$

$$\tau(T_c) = T_c (S_M(T) [A_1 + (2T_c - 2T)A_2]), \quad (40)$$

$$\tau(T_c) = T_c \left(S_M(T) \left[A_1 + (2T_c - 2 \frac{T_h + T_c}{2}) A_2 \right] \right), \quad (41)$$

$$\tau(T_c) = T_c S_M(T) [A_1 - \Delta T A_2]. \quad (42)$$

Then, σ_h can be determined as

$$\sigma_h = S_M(T_h) - \frac{\tau(T_h)\Delta T}{2T_h}, \quad (43)$$

$$\sigma_h = S_M(T) \left[1 + \frac{A_1}{2}\Delta T + \frac{A_2}{4}(\Delta T)^2 \right] - \frac{T_h S_M(T)\Delta T [A_1 + \Delta T A_2]}{2T_h}, \quad (44)$$

$$\sigma_h = S_M(T) \left[1 + \frac{A_1}{2}\Delta T + \frac{A_2}{4}(\Delta T)^2 - \frac{A_1}{2}\Delta T - \frac{A_2}{2}(\Delta T)^2 \right], \quad (45)$$

$$\sigma_h = S_M(T) \left[1 - \frac{A_2}{4}(\Delta T)^2 \right], \quad (46)$$

and σ_c can be determined as

$$\sigma_c = S_M(T_c) + \frac{\tau(T_c)\Delta T}{2T_c}, \quad (47)$$

$$\sigma_c = S_M(T) \left[1 - \frac{A_1}{2}\Delta T + \frac{A_2}{4}(\Delta T)^2 \right] + \frac{T_c S_M(T)\Delta T [A_1 - \Delta T A_2]}{2T_c}, \quad (48)$$

$$\sigma_c = S_M(T) \left[1 - \frac{A_1}{2}\Delta T + \frac{A_2}{4}(\Delta T)^2 + \frac{A_1}{2}\Delta T - \frac{A_2}{2}(\Delta T)^2 \right], \quad (49)$$

$$\sigma_c = S_M(T) \left[1 - \frac{A_2}{4}(\Delta T)^2 \right]. \quad (50)$$

Therefore,

$$\sigma_h = \sigma_c = S_M(T) \left[1 - \frac{A_2}{4}(\Delta T)^2 \right]. \quad (51)$$

Using (51) in (23) and (25) gives the new heat rate equations as

$$Q_h = S_M(T) \left[1 - \frac{A_2}{4}(\Delta T)^2 \right] T_h I + \frac{1}{2} I^2 R_M - K_M \Delta T, \quad (52)$$

$$Q_c = S_M(T) \left[1 - \frac{A_2}{4}(\Delta T)^2 \right] T_c I - \frac{1}{2} I^2 R_M - K_M \Delta T. \quad (53)$$

The electrical power is then equal to

$$P_{in} = Q_h - Q_c = S_M(T) \left[1 - \frac{A_2}{4}(\Delta T)^2 \right] \Delta T I + R_M(T_{AVG}) I^2. \quad (54)$$

Using (54), the procedure used in [39] for the identification of the temperature dependent parameters of a single Peltier can be redone as

$$V_P = V_{R_M} + V_{S_M} = R_M(T_{AVG})I_P + S_M(T) \left[1 - \frac{A_2}{4}(\Delta T)^2 \right] \Delta T, \quad (55)$$

$$R_M(T_{AVG}) = \frac{V_{R_M}}{\delta I_P}, \quad (56)$$

$$S_M(T_{AVG}) = S_M(T) \left[1 - \frac{A_2}{4}(\Delta T)^2 \right]. \quad (57)$$

This does not result in a change for the parameter S_M , but does clarify that the Thomson effect was already incorporated in the model of [39]. The data obtained for the parameter S_M is actually the ‘effective’ Seebeck coefficient, which has the Thomson effect embodied in it, if S_M is considered a function of temperature. If S_M is considered to have no temperature-dependency, (20) clearly shows that τ equals 0. Therefore, the model as created in [39] for a single Peltier element is valid and the lumped-capacitance model created needs no alteration.

Following [16], a lumped-capacitance model of the Peltier-based setup was created in [39], depicted in Figure 10. The lumps x_{1-18} correspond to the elements as indicated in Figure 1. The heat sink is divided into x_{1-4} , the aluminum top plate into x_{5-8} , the hot and cold side of Peltier 1 into respectively x_9 and x_{11} , the hot and cold side of Peltier 2 into respectively x_{10} and x_{12} , and the stainless steel bottom plate into x_{13-18} .

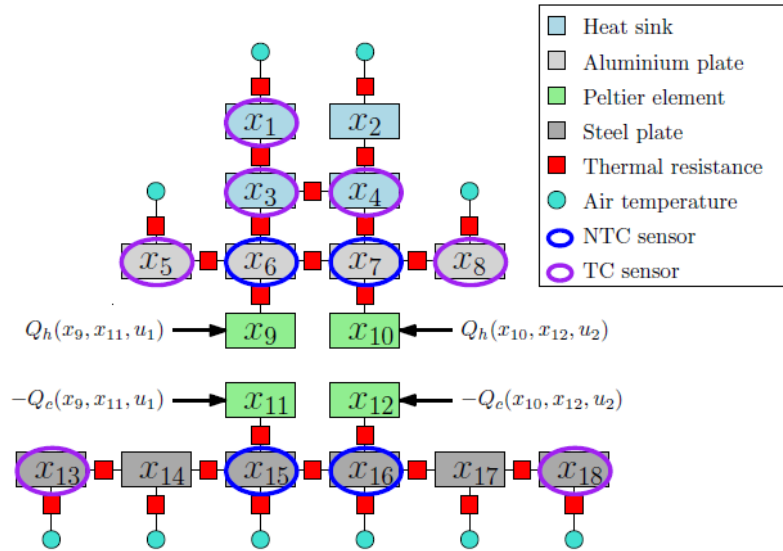


Figure 10: Schematic overview of the Peltier-based setup, (by) courtesy of [39].

In this model, for the sake of modelling simplicity, the width of the lumps adjacent to the Peltiers are assumed to be of the same width as the Peltiers themselves. Moreover, the spatial discretization of the heat sink has not been subjected to a Biot number analysis.

Now, rewriting the DEs into matrix formulation using the theory from [16] results in

$$E \begin{bmatrix} \dot{x}_{L_1} \\ \dot{x}_h \\ \dot{x}_c \\ \dot{x}_{L_2} \end{bmatrix} = \begin{bmatrix} A_1 & \emptyset \\ \emptyset & A_2 \end{bmatrix} \begin{bmatrix} x_{L_1} \\ x_h \\ x_c \\ x_{L_2} \end{bmatrix} + \begin{bmatrix} B_1 w \\ f_h(x_h, x_c, u_1, u_2) \\ f_c(x_h, x_c, u_1, u_2) \\ B_2 w \end{bmatrix}, \quad (58)$$

where E is the thermal capacitance matrix, $x_h = [x_9 \ x_{10}]^\top$ and $x_c = [x_{11} \ x_{12}]^\top$ are the lump temperatures of the hot and cold sides of the Peltiers respectively, $x_{L_1} = x_{1-8}$, and $x_{L_2} = x_{13-18}$ are the remaining lump temperatures connected to Peltier 1 and 2, respectively. An overview of the state-space lump division x_{L_1} , x_h , x_c , and x_{L_2} is given in Figure 11.

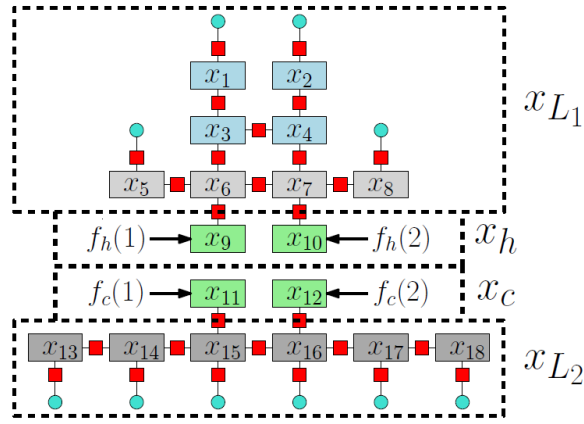


Figure 11: State-space lump division of the Peltier-based setup [39].

Furthermore, the heat transfer matrices A_1 and A_2 and heat load matrices B_1 and B_2 contain the appropriate thermal resistances to model the thermal coupling between the lumps, w denotes the ambient temperature, and u_1 and u_2 represent the applied currents to the Peltiers. The nonlinear thermodynamics of the Peltiers are captured in f_h and f_c and are described by

$$f_h = \begin{bmatrix} Q_h(x_9, x_{11}, u_1) \\ Q_h(x_{10}, x_{12}, u_2) \end{bmatrix} = \begin{bmatrix} S_M x_9 u_1 + \frac{1}{2} R_M u_1^2 - K_M (x_9 - x_{11}) \\ S_M x_{10} u_2 + \frac{1}{2} R_M u_2^2 - K_M (x_{10} - x_{12}) \end{bmatrix}, \quad (59)$$

and

$$f_c = \begin{bmatrix} -Q_c(x_9, x_{11}, u_1) \\ -Q_c(x_{10}, x_{12}, u_2) \end{bmatrix} = \begin{bmatrix} -S_M x_{11} u_1 + \frac{1}{2} R_M u_1^2 + K_M (x_9 - x_{11}) \\ -S_M x_{12} u_2 + \frac{1}{2} R_M u_2^2 + K_M (x_{10} - x_{12}) \end{bmatrix}. \quad (60)$$

The output matrix formulation is then

$$y = \begin{bmatrix} C_1 & & & \\ & 0 & & \\ & & \emptyset & \\ & \emptyset & & 0 \\ & & & & C_2 \end{bmatrix} \begin{bmatrix} x_{L_1} \\ x_h \\ x_c \\ x_{L_2} \end{bmatrix}, \quad (61)$$

where C_1 and C_2 are diagonal matrices filled with ones and zeros, according to the measured states through sensors.

3.3 Sensitivity analysis physics-based modeling parameters

The modeling parameters S_M , K_M and R_M have been determined in [39] with a dedicated experimental setup. The setup is provided in Figure 12, and consists of a Peltier element that is sandwiched between two stainless steel blocks, a 3D-printed High Impact PolyStyrene (HIPS) cover, a water cooler that extracts heat from the setup, and an aluminium clamping mechanism. Two NTC sensors are placed in each stainless steel block, to measure the cold and hot side of the Peltier element.

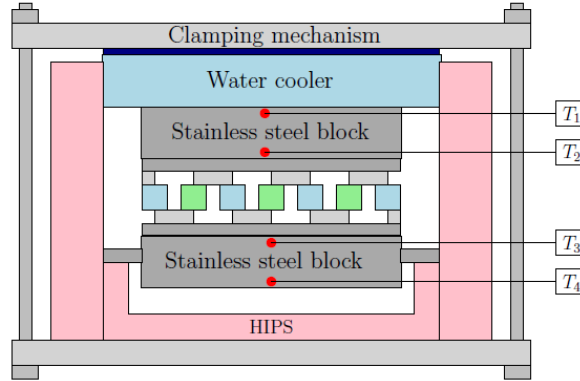


Figure 12: Dedicated experimental setup from [39] to determine temperature dependent modeling parameters.

The calibration of S_M and K_M is done by utilizing the slow thermal dynamics and fast electrical dynamics, and R_M is calibrated by estimating the hot and cold heat flows through the Peltier element, as explained in Sections 4.1.2 and 4.1.3 of [39]. In order to validate the model parameter calibration of a single Peltier, a sensitivity analysis is performed, which can be found in Appendix A.

The sensitivity analysis shows that calibration of the parameters S_M , K_M , and R_M has been done adequately. The output of the experiment is strongly dependent on S_M and K_M being correct. Since S_M is separately identified, for the identified S_M , a fitting K_M can be found by the optimization algorithm.

3.4 Conclusion

In this chapter, the physics-based model from [39] has been discussed. Following recommendation R.3 from [39], it has been observed that the Thomson effect was already incorporated in the model, and therefore no better results in terms of better correlation between model and measurements are obtained. The effective Seebeck coefficients have been identified, by assuming that S_M is temperature-dependent. If this dependency is not considered, based on (12), the Thomson effect falls out of the equations, and is neglected in the model.

Also, sensitivity analyses have been done to validate the model parameter calibration. This validation showed that the determining and optimization of the temperature dependent parameters S_M , R_M , and K_M has been done adequately. Even though the output of the exper-

iment is strongly dependent on S_M and K_M being correct, since S_M is separately identified, for the identified S_M , a fitting K_M can be found by the optimization algorithm.

The other recommendations from [39] concerning the setup or model design have also been considered. The mechanical design of the Peltier-based setup has not been altered for the Peltiers to be installed with constant clamping force. The Peltiers have been installed carefully, applying an as good as identical clamping force to both Peltiers. Also, since there is no desire to track higher frequent reference signals, the lumped-capacitance model is not improved by a finer discretization. Furthermore, the Fourier number has not been used to discretize the setup.

The physics-based model complexity is considered rich enough to make a fair comparison between the physics-based and data-driven model of the Peltier-based setup, which will be constructed in Chapter 5 using the methodology described in Chapter 4.

4 Data-driven modeling: methodology

In this chapter the methodology used to obtain a nonlinear data-driven model of the Peltier-based is described. In Section 4.1 the excitation signal for the identification is discussed. Section 4.2 then elaborates on the model structure, after which Section 4.3 continues on the identification procedure to obtain the data-driven model. Concluding, Section 4.4 summarizes the procedure briefly.

4.1 Excitation signal

For the identification of the Peltier-based setup, multisine excitations are considered. A multisine is a periodic signal with a user-defined amplitude spectrum, and freely adjustable phases. It is a pseudo-random signal, since its appearance features look random in the time domain, and has deterministic amplitudes in the frequency domain. The usage of multisines as excitation signals is inviting, because multisines are periodic, broadband, and by choosing the phases properly, low-crest-factor signals are obtained [34]. The phases are chosen randomly for the MS excitation signal used for the identification of the Peltier-based setup in Chapter 5. The periodicity allows the elimination of leakage in frequency domain identification, and the estimation of the covariance of the noise disturbances directly from data [29]. Furthermore, using multisines allows to distinguish the amount and degree of nonlinearities in a system by using multiple phase realizations.

It is defined as a sum of harmonically related sine waves

$$u(t) = \frac{1}{\sqrt{N}} \sum_{k=-\frac{N}{2}+1}^{\frac{N}{2}-1} U_k e^{j(2\pi f_s \frac{k}{N} t + \phi_k)}, \quad (62)$$

where $U_k = U_{-k}$, $\phi_k = -\phi_{-k}$, N the number of time samples in one period, j the imaginary unit, and f_s the sampling frequency [Hz]. Amplitudes U_k are defined by the user to meet a desired spectrum, and phases ϕ_k are drawn from a uniform distribution on $[0, 2\pi)$, such that $\mathcal{E}(j\phi_k) = 0$, where \mathcal{E} denotes the mathematical expectation. The factor $\frac{1}{\sqrt{N}}$ serves as a scaling factor such that, as $N \rightarrow \infty$, the power of the multisine remains finite, and its Root Mean Square (RMS) value stays constant as N increases [34].

4.2 Nonlinear state-space model structure

In order to obtain a parametric model, a modeling structure needs to be defined. A n_a^{th} order discrete-time state space model is commonly expressed as

$$\begin{cases} \mathbf{x}(t+1) = f(\mathbf{x}(t), \mathbf{u}(t)) \\ \mathbf{y}(t) = g(\mathbf{x}(t), \mathbf{u}(t)) \end{cases}, \quad (63)$$

with $\mathbf{x} \in \mathbb{R}^{n_a}$ the state vector, $\mathbf{u} \in \mathbb{R}^{n_u}$ the input vector, and $\mathbf{y} \in \mathbb{R}^{n_y}$ the output vector.

Consider the general state space model in (63) and apply a functional expansion of the functions f and g . Although various kinds of basis functions can be used for this purpose, here

a set of polynomial basis functions is chosen. The main advantages of polynomials are their easy application in a multi variable framework and their straightforwardness to compute.

Using the Polynomial NonLinear State Space (PNLSS) model as defined in [31], (63) becomes

$$\begin{cases} \mathbf{x}(t+1) = \mathbf{A}\mathbf{x}(t) + \mathbf{B}\mathbf{u}(t) + \mathbf{E}\zeta(t) \\ \mathbf{y}(t) = \mathbf{C}\mathbf{x}(t) + \mathbf{D}\mathbf{u}(t) + \mathbf{F}\boldsymbol{\eta}(t) \end{cases} \quad (64)$$

Here, the coefficients of the linear terms in $\mathbf{u}(t)$ and $\mathbf{x}(t)$ are given by $\mathbf{A} \in \mathbb{R}^{n_a \times n_a}$ and $\mathbf{B} \in \mathbb{R}^{n_a \times n_u}$ in the state equation, and $\mathbf{C} \in \mathbb{R}^{n_y \times n_a}$ and $\mathbf{D} \in \mathbb{R}^{n_y \times n_u}$ in the output equation. Vectors $\zeta \in \mathbb{R}^{n_\zeta}$ and $\boldsymbol{\eta} \in \mathbb{R}^{n_\eta}$ contain nonlinear monomials in $\mathbf{x}(t)$ and $\mathbf{u}(t)$ of degree two up to user-chosen degree d , and matrices $\mathbf{E} \in \mathbb{R}^{n_a \times n_\zeta}$ and $\mathbf{F} \in \mathbb{R}^{n_y \times n_\eta}$ are filled with their associated coefficients. The amount of nonlinear terms in (64) can grow quite rapidly if the order of the model grows, and therefore a trade-off will be made between model accuracy and parameter parsimony. This will be done during the approximation of the best linear model in Section 4.3.

Separating the model structure in a linear and a nonlinear part does not influence the behavior of the model. However, since the first step of the identification procedure consists of estimating a linear model, this distinction will turn out to be very efficient.

4.3 Identification procedure

In order to identify the PNLSS model from (64), the methodology from [31] is followed. Firstly, in Section 4.3.1 a nonparametric best linear approximation is determined in a least-square sense from the experimental data. Secondly, in Section 4.3.2, using this best linear approximation, a parametric linear model is estimated, using the frequency domain subspace identification algorithm from [25] while employing the sample covariance matrix instead of the true covariance, as presented in [35]. Thirdly, the quality of the found parametric linear models is improved by nonlinear optimization in Section 4.3.3. Lastly, in Section 4.3.4, the full nonlinear model is estimated, using a nonlinear search routine.

4.3.1 Best Linear Approximation

Consider the Best Linear Approximation (BLA); the linear model that approximates the system output best in least-squares sense [34], generally varying with input frequency content and RMS value [28]. To obtain the BLA, a set of M experiments can be conducted, each consisting of a different multisine excitation realization, accumulating P steady-state periods of input-output (IO) data [36].

Using periodic excitations, the frequency response function (FRF) estimate $\hat{\mathbf{G}}^{[m]}(j\omega_k) \in \mathbb{C}$, for the m^{th} experiment is obtained as

$$\hat{\mathbf{G}}^{[m]}(j\omega_k) = \hat{\mathbf{Y}}^{[m]}(k) \left(\hat{\mathbf{U}}^{[m]}(k) \right)^{-1}, \quad (65)$$

where \hat{G} denotes the estimated value of G , with

$$\begin{aligned}\hat{\mathbf{Y}}^{[m]}(k) &= \frac{1}{P} \sum_{p=1}^P \mathbf{Y}^{[m,p]}(k), \\ \hat{\mathbf{U}}^{[m]}(k) &= \frac{1}{P} \sum_{p=1}^P \mathbf{U}^{[m,p]}(k),\end{aligned}\tag{66}$$

with $\hat{\mathbf{Y}}^{[m,p]}(k)$ and $\hat{\mathbf{U}}^{[m,p]}(k)$ the discrete Fourier transform (DFT) of the output $\mathbf{y}(t)$ and the input $\mathbf{u}(t)$ for the p^{th} period of experiment m in a periodic excitation setup.

Using the obtained M FRFs, the best linear approximation $\hat{\mathbf{G}}_{BLA}$ can be determined with

$$\hat{\mathbf{G}}_{BLA}(j\omega_k) = \frac{1}{M} \sum_{m=1}^M \hat{\mathbf{G}}^{[m]}(j\omega_k).\tag{67}$$

Due to the periodic nature of the excitation signals, a distinction between the effect of the nonlinear distortions and the measurement noise on the Best Linear Approximation can be made [30]. While variations over P periods arise from the measurement noise, the variations over M experiments are caused by the combination of measurement noise and stochastic nonlinear behavior.

In order to clearly differentiate the two, firstly, the sample covariance of $\hat{\mathbf{G}}_{BLA}$ due to measurement noise is determined. This is done by firstly calculating the sample covariance matrices of the estimated DFT spectra $\hat{\mathbf{U}}(k)^{[m]}$ and $\hat{\mathbf{Y}}(k)^{[m]}$ with

$$\begin{aligned}\hat{\mathbf{C}}_{\hat{\mathbf{U}}^{[m]}} &= \frac{1}{P-1} \sum_{p=1}^P \text{vec}\left(\mathbf{U}^{[m,p]} - \hat{\mathbf{U}}^{[m]}\right) \text{vec}\left(\mathbf{U}^{[m,p]} - \hat{\mathbf{U}}^{[m]}\right)^H, \\ \hat{\mathbf{C}}_{\hat{\mathbf{Y}}^{[m]}} &= \frac{1}{P-1} \sum_{p=1}^P \text{vec}\left(\mathbf{Y}^{[m,p]} - \hat{\mathbf{Y}}^{[m]}\right) \text{vec}\left(\mathbf{Y}^{[m,p]} - \hat{\mathbf{Y}}^{[m]}\right)^H, \\ \hat{\mathbf{C}}_{\hat{\mathbf{Y}}\hat{\mathbf{U}}^{[m]}} &= \frac{1}{P-1} \sum_{p=1}^P \text{vec}\left(\mathbf{Y}^{[m,p]} - \hat{\mathbf{Y}}^{[m]}\right) \text{vec}\left(\mathbf{U}^{[m,p]} - \hat{\mathbf{U}}^{[m]}\right)^H,\end{aligned}\tag{68}$$

where $\text{vec}(\mathbf{A})$ denotes the operation that stacks the columns of matrix \mathbf{A} on top of each other, and \mathbf{A}^H denotes the Hermitian transpose of matrix \mathbf{A} . In (68), k is omitted for simplification. From $\hat{\mathbf{C}}_{\hat{\mathbf{U}}^{[m]}} \in \mathbb{C}^{n_u n_u \times n_u n_u}$, $\hat{\mathbf{C}}_{\hat{\mathbf{Y}}^{[m]}} \in \mathbb{C}^{n_y n_y \times n_y n_y}$, and $\hat{\mathbf{C}}_{\hat{\mathbf{Y}}\hat{\mathbf{U}}^{[m]}} \in \mathbb{C}^{n_y n_u \times n_u n_u}$, the sample covariance $\hat{\mathbf{C}}_n^{[m]}$ of $\hat{\mathbf{G}}^{[m]}$ is approximated with [34]

$$\begin{aligned}\hat{\mathbf{C}}_n^{[m]} &= \left(\left(\hat{\mathbf{U}}^{[m]} \right)^{-\top} \otimes \mathbf{I}_{n_y} \right) \hat{\mathbf{C}}_{\hat{\mathbf{Y}}^{[m]}} \left(\left(\hat{\mathbf{U}}^{[m]} \right)^{-\top} \otimes \mathbf{I}_{n_y} \right)^H + \dots \\ &\quad + \left(\left(\hat{\mathbf{U}}^{[m]} \right)^{-\top} \otimes \hat{\mathbf{G}}^{[m]} \right) \hat{\mathbf{C}}_{\hat{\mathbf{U}}^{[m]}} \left(\left(\hat{\mathbf{U}}^{[m]} \right)^{-\top} \otimes \hat{\mathbf{G}}^{[m]} \right)^H + \dots \\ &\quad - 2 \text{herm} \left\{ \left(\left(\hat{\mathbf{U}}^{[m]} \right)^{-\top} \otimes \mathbf{I}_{n_y} \right) \hat{\mathbf{C}}_{\hat{\mathbf{Y}}\hat{\mathbf{U}}^{[m]}} \left(\left(\hat{\mathbf{U}}^{[m]} \right)^{-\top} \otimes \hat{\mathbf{G}}^{[m]} \right)^H \right\},\end{aligned}\tag{69}$$

with $\hat{\mathbf{C}}_n^{[m]} \in \mathbb{C}^{n_y n_u \times n_y n_u}$, \mathbf{I}_{n_y} the $n_y \times n_y$ identity matrix, and \otimes the Kronecker matrix product. In a noiseless input framework, the expression in (69) simplifies to

$$\hat{\mathbf{C}}_n^{[m]} = \left(\left(\hat{\mathbf{U}}^{[m]} \right)^{-\top} \otimes \mathbf{I}_{n_y} \right) \hat{\mathbf{C}}_{\hat{Y}^{[m]}} \left(\left(\hat{\mathbf{U}}^{[m]} \right)^{-\top} \otimes \mathbf{I}_{n_y} \right)^H. \quad (70)$$

Averaging over M estimates $\hat{\mathbf{C}}_n^{[m]}$, and applying the \sqrt{N} -law [30], results in the improved estimate of the covariance matrix characterizing measurement noise

$$\hat{\mathbf{C}}_n = \frac{1}{M^2} \sum_{m=1}^M \hat{\mathbf{C}}_n^{[m]}. \quad (71)$$

The combination of measurement noise and stochastic nonlinear behaviour is characterized by the total sample covariance $\hat{\mathbf{C}}_{\text{BLA}}$. It is determined from the M estimates $\hat{\mathbf{G}}^{[m]}(j\omega_k)$ as

$$\hat{\mathbf{C}}_{\text{BLA}} = \frac{1}{M(M-1)} \sum_{m=1}^M \text{vec} \left(\hat{\mathbf{G}}^{[m]} - \hat{\mathbf{G}}_{\text{BLA}} \right) \text{vec} \left(\hat{\mathbf{G}}^{[m]} - \hat{\mathbf{G}}_{\text{BLA}} \right)^H. \quad (72)$$

The total covariance of the BLA is equal to the sum of the covariance due to nonlinear contributions $\mathbf{C}_{\text{NL}}(k)$ and the measurement noise covariance $\mathbf{C}_n(k)$ through

$$\mathbf{C}_{\text{BLA}}(k) = \mathbf{C}_{\text{NL}}(k) + \mathbf{C}_n(k). \quad (73)$$

Therefore, $\hat{\mathbf{C}}_{\text{NL}}(k)$ is estimated with

$$\hat{\mathbf{C}}_{\text{NL}}(k) = \hat{\mathbf{C}}_{\text{BLA}}(k) - \hat{\mathbf{C}}_n(k). \quad (74)$$

Concluding, using M experiments, the Best Linear Approximation $\hat{\mathbf{G}}_{\text{BLA}}(j\omega_k)$ is estimated. Also, the total sample covariance matrix $\hat{\mathbf{C}}_{\text{BLA}}(k)$ of the estimate $\hat{\mathbf{G}}_{\text{BLA}}(j\omega_k)$, due to the combination of measurement noise and stochastic nonlinear behaviour, is determined. Furthermore, the measurement noise sample covariance matrix $\hat{\mathbf{C}}_n(k)$ of the estimate $\hat{\mathbf{G}}_{\text{BLA}}(j\omega_k)$ and the sample covariance of the stochastic nonlinear contributions $\hat{\mathbf{C}}_{\text{NL}}(k)$ are determined.

4.3.2 Frequency domain subspace identification

The next step is to transform the nonparametric estimate $\hat{\mathbf{G}}_{\text{BLA}}(j\omega_k)$ into a parametric model. The goal is to estimate the linear state space matrices \mathbf{A} , \mathbf{B} , \mathbf{C} , and \mathbf{D} of a discrete-time, linear state-space model, while the sample covariance matrix $\hat{\mathbf{C}}_{\text{BLA}}$ is taken into account. This will be done using the frequency domain subspace algorithm from [25]. The estimated subspace models are optimized using the results from [30] and [35].

The transformation from the nonparametric BLA to a linear model can be done for different model orders n and subspace parameter r , defined as the number of rows of the extended observability matrix. The quality of the subspace model is evaluated through a weighted least-squares cost function.

In order to arrive at this linear model from the frequency response data from $\hat{\mathbf{G}}_{\text{BLA}}(j\omega_k)$, several steps need to be taken. Firstly, the model structure and definitions needed are given

in Section 4.3.2.1. Secondly, in Section 4.3.2.2 the extended observability matrix \mathbf{O}_r is estimated, given $\hat{\mathbf{G}}_{\text{BLA}}(j\omega_k)$ and $\hat{\mathbf{C}}_{\text{BLA}}$. Then, using \mathbf{O}_r , matrices \mathbf{A} and \mathbf{C} are estimated in Section 4.3.2.3. Finally, given \mathbf{A} , \mathbf{C} , and $\hat{\mathbf{G}}_{\text{BLA}}(j\omega_k)$, \mathbf{B} and \mathbf{D} are estimated in Section 4.3.2.4.

4.3.2.1 Model structure & definitions

In order to be able to estimate the extended observability matrix \mathbf{O}_r , the model structure and several definitions are introduced firstly. Assume that the system G is a stable, linear time-invariant (LTI) discrete-time system of finite order n with m inputs and p outputs, and can be described by a state-space model

$$\begin{cases} \mathbf{x}(t+1) = \mathbf{A}\mathbf{x}(t) + \mathbf{B}\mathbf{u}(t) \\ \mathbf{y}(t) = \mathbf{C}\mathbf{x}(t) + \mathbf{D}\mathbf{u}(t) \end{cases}, \quad (75)$$

with $\mathbf{y}(t) \in \mathbb{R}^p$, $\mathbf{u}(t) \in \mathbb{R}^m$, and $\mathbf{x}(t) \in \mathbb{R}^n$.

Consider the DFT of (75) in N samples as

$$\begin{cases} z_k \mathbf{X}(k) = \mathbf{A}\mathbf{X}(k) + \mathbf{B}\mathbf{U}(k) + z_k x_I \\ \mathbf{Y}(k) = \mathbf{C}\mathbf{X}(k) + \mathbf{D}\mathbf{U}(k) \end{cases}, \quad (76)$$

for $k = 1, \dots, F$ frequencies, and with $z_k = e^{j2\pi \frac{k}{N}}$. In the transient term $z_k x_I$, x_I is defined as

$$x_I = \frac{1}{\sqrt{N}}(x(0) - x(N)). \quad (77)$$

As only steady-state periods are considered, the transient term will be neglected from here.

Since the BLA determination resulted in an estimate in FRF form, rewrite (76) into FRF form by setting $\mathbf{U}(k) = \mathbf{I}_{n_u}$, with \mathbf{I}_{n_u} the $n_u \times n_u$ identity matrix. The plant model is then defined as

$$\begin{cases} z_k \mathbf{X}(k) = \mathbf{A}\mathbf{X}(k) + \mathbf{B} \\ \mathbf{G}(k) = \mathbf{C}\mathbf{X}(k) + \mathbf{D} \end{cases}, \quad (78)$$

with $\mathbf{X}(k) \in \mathbb{C}^{n_a \times n_u}$ the state matrix, and $\mathbf{G}(k) \in \mathbb{C}^{n_y \times n_u}$.

Now, multiply the latter equation from (78) with z_k^p , and develop it by substitution of $z_k \mathbf{X}(k)$ with the first equation of (78), and repeat for $p-1$ substitutions, as

$$\begin{aligned} z_k^p \mathbf{G}(k) &= z_k^p (\mathbf{C}\mathbf{X}(k) + \mathbf{D}) \\ &= z_k^{p-1} (\mathbf{C}z_k \mathbf{X}(k) + z_k \mathbf{D}) \\ &= z_k^{p-1} (\mathbf{C}\mathbf{A}\mathbf{X}(k) + \mathbf{C}\mathbf{B} + z_k \mathbf{D}) \\ &= z_k^{p-2} (\mathbf{C}\mathbf{A}^2 \mathbf{X}(k) + \mathbf{C}\mathbf{A}\mathbf{B} + z_k \mathbf{C}\mathbf{B} + z_k^2 \mathbf{D}) \\ &\quad \dots \\ z_k^p \mathbf{G}(k) &= \mathbf{C}\mathbf{A}^p \mathbf{X}(k) + (\mathbf{C}\mathbf{A}^{p-1} \mathbf{B} + z_k \mathbf{C}\mathbf{A}^{p-2} \mathbf{B} + \dots + z_k^{p-1} \mathbf{C}\mathbf{B} + z_k^p \mathbf{D}). \end{aligned} \quad (79)$$

Now, applying $p = 0, \dots, r-1$ with $r > n_a$ to (79) gives

$$\begin{aligned}
\mathbf{G}(k) &= \mathbf{C}\mathbf{X}(k) + \mathbf{D} \\
z_k \mathbf{G}(k) &= \mathbf{C}\mathbf{A}\mathbf{X}(k) + \mathbf{C}\mathbf{B} + z_k \mathbf{D} \\
&\dots \\
z_k^{r-1} \mathbf{G}(k) &= \mathbf{C}\mathbf{A}^{r-1} \mathbf{X}(k) + \mathbf{C}\mathbf{A}^{r-2} \mathbf{B} + \dots + z_k^{r-2} \mathbf{C}\mathbf{B} + z_k^{r-1} \mathbf{D}.
\end{aligned} \tag{80}$$

In order to convert the model structure in (80), a few definitions are needed. The extended observability matrix \mathbf{O}_r is defined as

$$\mathbf{O}_r = \begin{bmatrix} \mathbf{C} \\ \mathbf{C}\mathbf{A} \\ \dots \\ \mathbf{C}\mathbf{A}^{r-1} \end{bmatrix}, \tag{81}$$

and the matrix \mathbf{S}_r containing the Markov parameters is defined as

$$\mathbf{S}_r = \begin{bmatrix} \mathbf{D} & 0 & \dots & 0 & 0 \\ \mathbf{C}\mathbf{B} & \mathbf{D} & \dots & 0 & 0 \\ \dots & \dots & \dots & \dots & \dots \\ \mathbf{C}\mathbf{A}^{r-2} \mathbf{B} & \mathbf{C}\mathbf{A}^{r-3} \mathbf{B} & \dots & \mathbf{C}\mathbf{B} & \mathbf{D} \end{bmatrix}. \tag{82}$$

Furthermore, also define

$$\mathbf{W}_r(k) = [1 \quad z_k \quad \dots \quad z_k^{r-1}]^T. \tag{83}$$

Applying (81), (82), and (83) to (80) results in the transformation into

$$\mathbf{G} = \mathbf{O}_r \mathbf{X} + \mathbf{S}_r \mathbf{I}, \tag{84}$$

with matrices \mathbf{G} , \mathbf{X} , and \mathbf{I} defined as

$$\begin{aligned}
\mathbf{G} &= [\mathbf{W}_r(1) \otimes \mathbf{G}(1) \quad \dots \quad \mathbf{W}_r(F) \otimes \mathbf{G}(F)] \\
\mathbf{X} &= [\mathbf{X}(1) \quad \dots \quad \mathbf{X}(F)] \\
\mathbf{I} &= [\mathbf{W}_r(1) \otimes \mathbf{I}_{n_u} \quad \dots \quad \mathbf{W}_r(F) \otimes \mathbf{I}_{n_u}]
\end{aligned} \tag{85}$$

Since the goal is to estimate the real-valued observability matrix \mathbf{O}_r , convert the complex data equation in (84) into a real equation. Consider $\mathbf{A}^{\text{re}} = [\text{Re}(\mathbf{A}) \quad \text{Im}(\mathbf{A})]$, and apply it to (84), converting it into

$$\mathbf{G}^{\text{re}} = \mathbf{O}_r \mathbf{X}^{\text{re}} + \mathbf{S}_r \mathbf{I}. \tag{86}$$

An additive noise setting is considered, like

$$\mathbf{G} = \mathbf{G}_0 + \mathbf{N}_G(k), \tag{87}$$

with \mathbf{G}_0 the noiseless plant. The noise matrix $\mathbf{N}_G(k)$ is assumed to have independent (over k) circular complex normally distributed elements, zero mean

$$\mathcal{E}\{\mathbf{N}_G(k)\} = 0, \quad (88)$$

and covariance $\mathbf{C}_G(k)$

$$\mathbf{C}_G(k) = \mathcal{E}\{\text{vec}(\mathbf{N}_G(k))\text{vec}^H(\mathbf{N}_G(k))\}. \quad (89)$$

Applying the considered noise setting to the model structure from (86) converts it into

$$\mathbf{G}^{\text{re}} = \mathbf{O}_r \mathbf{X}^{\text{re}} + \mathbf{S}_r \mathbf{I} + \mathbf{N}_G^{\text{re}}, \quad (90)$$

with

$$\mathbf{N}_G = \left[\mathbf{W}_r(1) \otimes \mathbf{N}_G(1) \quad \cdots \quad \mathbf{W}_r(F) \otimes \mathbf{N}_G(F) \right]. \quad (91)$$

A final assumption is that the true plant model can be written as (78), with (\mathbf{A}, \mathbf{C}) observable, and (\mathbf{A}, \mathbf{B}) controllable [30]. Referring to the true linear model seems unfit when the algorithm is used to identify a model for a nonlinear setup, since the actual setup will not follow the structure in (78). However, the current goal is to retrieve a parametric model for the Best Linear Approximation of the system. To the BLA, the nonlinear behavior of the setup results in either bias contributions, changing the dynamic behavior of the BLA, or stochastic contributions, acting like ordinary disturbing noise.

Therefore, with the model structure and the needed definitions introduced, the state-space matrices from (90) can be estimated to proceed with the estimation of the linear model matrices.

4.3.2.2 Estimate \mathbf{O}_r

In order to estimate \mathbf{O}_r , given $\hat{\mathbf{G}}_{\text{BLA}}$ and $\hat{\mathbf{C}}_{\text{BLA}}$, choose parameter $r > n_a$ and construct

$$\mathbf{Z} = \begin{bmatrix} \mathbf{I}^{\text{re}} \\ \hat{\mathbf{G}}_{\text{BLA}}^{\text{re}} \end{bmatrix}, \quad (92)$$

and

$$\mathbf{C}_N = \text{Re} \left(\sum_{k=1}^F \mathbf{W}_r(k) \mathbf{W}_r^H(k) \otimes \sum_{i=1}^{n_u} \hat{\mathbf{C}}_{\text{BLA}}^i(k) \right), \quad (93)$$

where $\hat{\mathbf{C}}_{\text{BLA}}^i(k)$ denotes the i^{th} diagonal partition of $\hat{\mathbf{C}}_{\text{BLA}}(k)$ [30].

Eliminate \mathbf{I}^{re} from \mathbf{Z} , by using a QR-decomposition of \mathbf{Z}^\top

$$\mathbf{Z} = \mathbf{R}^\top \mathbf{Q}^\top, \quad (94)$$

resulting in

$$\mathbf{Z} = \begin{bmatrix} \mathbf{I}^{\text{re}} \\ \hat{\mathbf{G}}_{\text{BLA}}^{\text{re}} \end{bmatrix} = \begin{bmatrix} \mathbf{R}_{11}^\top & 0 \\ \mathbf{R}_{12}^\top & \mathbf{R}_{22}^\top \end{bmatrix} \begin{bmatrix} \mathbf{Q}_1^\top \\ \mathbf{Q}_2^\top \end{bmatrix}. \quad (95)$$

When \mathbf{R}_{11}^\top is defined as the upper left block with dimension $rn_u \times rn_u$, \mathbf{R}_{12}^\top has dimension $rn_y \times rn_u$, and \mathbf{R}_{22}^\top with dimension $rn_y \times rn_y$ remains after the elimination of \mathbf{I}^{re} from \mathbf{Z} .

Now, remove the noise influence from (90) by calculating the singular value decomposition (SVD) of $\mathbf{C}_N^{-\frac{1}{2}} \mathbf{R}_{22}^\top$ as

$$\mathbf{C}_N^{-\frac{1}{2}} \mathbf{R}_{22}^\top = \mathbf{U} \mathbf{\Sigma} \mathbf{V}^\top, \quad (96)$$

so \mathcal{O}_r can be estimated as

$$\hat{\mathcal{O}}_r = \mathbf{C}_N^{\frac{1}{2}} \mathbf{U}_{[:,1:n_a]}, \quad (97)$$

where $\mathbf{U}_{[:,i]}$ denotes the i^{th} column of \mathbf{U} .

Using the estimation of \mathcal{O}_r , \mathbf{A} and \mathbf{C} can be estimated.

4.3.2.3 Estimate A and C

In order to estimate \mathbf{A} and \mathbf{C} from $\hat{\mathcal{O}}_r$, utilize the shift property of \mathcal{O}_r [30] as

$$\begin{aligned} \hat{\mathbf{A}} &= \hat{\mathcal{O}}_{r[1:(r-1)n_y,:]}^\dagger \hat{\mathcal{O}}_{r[n_y+1:rn_y,:]}, \\ \hat{\mathbf{C}} &= \hat{\mathcal{O}}_{r[1:n_y,:]} \end{aligned}, \quad (98)$$

where $\hat{\mathcal{O}}_{r[j,:]}$ denotes the j^{th} row of $\hat{\mathcal{O}}_r$, and $\hat{\mathcal{O}}_r^\dagger$ is the Moore-Penrose pseudoinverse of the full column rank matrix $\hat{\mathcal{O}}_r$.

Using $\hat{\mathbf{A}}$ and $\hat{\mathbf{C}}$, \mathbf{B} and \mathbf{D} can be estimated.

4.3.2.4 Estimate B and D

The final step towards a parametric linear model is the estimation of \mathbf{B} and \mathbf{D} . In order to estimate \mathbf{B} and \mathbf{D} using the found $\hat{\mathbf{A}}$ and $\hat{\mathbf{C}}$, minimize the weighted least-squares (WLS) cost function \mathbf{V}_L with respect to \mathbf{B} and \mathbf{D} . \mathbf{V}_L is given as

$$\mathbf{V}_L = \sum_{k=1}^F \boldsymbol{\epsilon}_L^H(k) \mathbf{W}_L \boldsymbol{\epsilon}_L(k), \quad (99)$$

with \mathbf{W}_L a weighting function, typically chosen as $\hat{\mathbf{C}}_{\text{BLA}}^{-1}(k)$, and the model fitting error $\boldsymbol{\epsilon}_L$ is defined as

$$\boldsymbol{\epsilon}_L(k) = \mathbf{G}_L(j\omega_k) - \hat{\mathbf{G}}_{\text{BLA}}(j\omega_k). \quad (100)$$

This results in the transfer function of the linear subspace model, constructed as

$$\mathbf{G}_L(j\omega_k) = \hat{\mathbf{C}}(z_k \mathbf{I}_{n_a} - \hat{\mathbf{A}})^{-1} \hat{\mathbf{B}} + \hat{\mathbf{D}}. \quad (101)$$

4.3.3 Nonlinear optimization of the linear model

Generally, the subspace method of [25] combined with the results from [35] applied in Section 4.3.2 yields a reasonably low value of the cost function \mathbf{V}_L in (99). However, in practice, \mathbf{V}_L depends strongly on the initially user-chosen subspace parameter r [30].

A logical next step to improve the linear model found in (101) is applying the subspace algorithm for different values of r , and selecting the model corresponding to the lowest \mathbf{V}_L . In order to improve the quality of the obtained linear model even further, minimize the cost function in (99) with respect to all parameters $(\mathbf{A}, \mathbf{B}, \mathbf{C}, \mathbf{D})$ instead of only \mathbf{B} and \mathbf{D} .

Minimizing (99) with respect to all parameters $(\mathbf{A}, \mathbf{B}, \mathbf{C}, \mathbf{D})$ results in a nonlinear optimization problem. Using the Levenberg-Marquardt algorithm [22][24], this problem can be solved. This can be done using perturbations, but in order to accelerate the optimization, the Jacobian of the model error $\epsilon_L(k)$ with respect to the model parameters is computed with

$$\begin{cases} \frac{\partial \epsilon_L(k)}{\partial \mathbf{A}_{ij}} = \text{vec}(\mathbf{C}(z_k \mathbf{I}_{n_a} - \mathbf{A})^{-1} \mathbf{I}_{ij}^{n_a \times n_a} (z_k \mathbf{I}_{n_a} - \mathbf{A})^{-1} \mathbf{B}) \\ \frac{\partial \epsilon_L(k)}{\partial \mathbf{B}_{ij}} = \text{vec}(\mathbf{C}(z_k \mathbf{I}_{n_a} - \mathbf{A})^{-1} \mathbf{I}_{ij}^{n_a \times n_u}) \\ \frac{\partial \epsilon_L(k)}{\partial \mathbf{C}_{ij}} = \text{vec}(\mathbf{I}_{ij}^{n_y \times n_a} (z_k \mathbf{I}_{n_a} - \mathbf{A})^{-1} \mathbf{B}) \\ \frac{\partial \epsilon_L(k)}{\partial \mathbf{D}_{ij}} = \text{vec}(\mathbf{I}_{ij}^{n_y \times n_u}). \end{cases}, \quad (102)$$

where \mathbf{A}_{ij} denotes the ij^{th} element of \mathbf{A} . Furthermore, while carrying out the nonlinear optimization, the unstable models estimated in Section 4.3.2 can be stabilized, for example by using the methods described in [8].

In order to estimate the final model order n , the procedure of minimizing the cost function in (99) is repeated for different model orders n_a . Subsequently, preferably the linear model with the lowest validation fitting error is selected, while striving to maintain a minimal amount of modeling parameters.

4.3.4 Estimation full nonlinear model

The final step in the identification procedure is to estimate the full nonlinear model

$$\begin{cases} \mathbf{x}(t+1) = \mathbf{A}\mathbf{x}(t) + \mathbf{B}\mathbf{u}(t) + \mathbf{E}\zeta(t) \\ \mathbf{y}(t) = \mathbf{C}\mathbf{x}(t) + \mathbf{D}\mathbf{u}(t) + \mathbf{F}\eta(t) + \mathbf{e}(t) \end{cases}, \quad (103)$$

with $\mathbf{e}(t)$ the output noise. Input $\mathbf{u}(t)$ is assumed to be noiseless, meaning it is independent of the output noise, and it is observed without errors.

All parameters of the full nonlinear model $(\mathbf{A}, \mathbf{B}, \mathbf{C}, \mathbf{D}, \mathbf{E}, \mathbf{F})$ are estimated by minimizing a second weighted least-squares cost function \mathbf{V}_{NL} with respect to

$$\boldsymbol{\theta} = [\text{vec}(\mathbf{A}) \quad \text{vec}(\mathbf{B}) \quad \text{vec}(\mathbf{C}) \quad \text{vec}(\mathbf{D}) \quad \text{vec}(\mathbf{E}) \quad \text{vec}(\mathbf{F})]^\top, \quad (104)$$

starting from the linear matrices acquired in 4.3.3. Zero initial values are considered for nonlinear coefficients in (\mathbf{E}, \mathbf{F}) . It is possible to minimize \mathbf{V}_{NL} only with respect to (\mathbf{E}, \mathbf{F}) , and

preserve the found linear model matrices. This, however, would limit the solution space of the optimization problem, and therefore will most likely lead to worse results than for minimizing with respect to all model parameters in $(\mathbf{A}, \mathbf{B}, \mathbf{C}, \mathbf{D}, \mathbf{E}, \mathbf{F})$.

Consider the WLS cost function

$$\mathbf{V}_{\text{NL}}(\boldsymbol{\theta}) = \sum_{k=1}^F \boldsymbol{\epsilon}_{\text{NL}}^H(k, \boldsymbol{\theta}) \mathbf{W}_{\text{NL}}(k) \boldsymbol{\epsilon}_{\text{NL}}(k, \boldsymbol{\theta}), \quad (105)$$

with $\mathbf{W}_{\text{NL}}(k) \in \mathbb{C}^{n_y \times n_y}$ a user-chosen frequency domain weighting function, typically chosen equal to the inverse of the covariance matrix of the output $\hat{\mathbf{C}}_y^{-1}(k)$. If no covariance information is available, a constant weighting can be employed. It is also possible to put more emphasis on a certain frequency band of interest, by choosing $\mathbf{W}_{\text{NL}}(k)$ properly [30].

In (105) the model error measure is equal to

$$\boldsymbol{\epsilon}_{\text{NL}}(k, \boldsymbol{\theta}) = \mathbf{Y}_{\text{NL}}(k, \boldsymbol{\theta}) - \mathbf{Y}(k), \quad (106)$$

with $\mathbf{Y}_{\text{NL}}(k, \boldsymbol{\theta})$ and $\mathbf{Y}(k)$ the DFT of the modeled output and the measured output respectively.

Minimizing \mathbf{V}_{NL} is done through the Levenberg-Marquardt algorithm [22][24]. Therefore, the Jacobian of the output with respect to the model parameters needs to be computed as

$$J(k, \boldsymbol{\theta}) = \frac{\partial \boldsymbol{\epsilon}(k, \boldsymbol{\theta})}{\partial \boldsymbol{\theta}} = \frac{\partial \mathbf{Y}_{\text{NL}}(k, \boldsymbol{\theta})}{\partial \boldsymbol{\theta}}. \quad (107)$$

Since the calculation of $\mathbf{Y}_{\text{NL}}(k, \boldsymbol{\theta})$, and therefore $J(k, \boldsymbol{\theta})$ is impractical directly in the frequency domain, this will be done in the time-domain, followed by a DFT. Expressions for the Jacobian of the model equations from (103) can be found in Appendix B of [31].

Utilizing these expressions, all parameters of the full nonlinear model $(\mathbf{A}, \mathbf{B}, \mathbf{C}, \mathbf{D}, \mathbf{E}, \mathbf{F})$ are estimated.

4.4 Conclusion

In order to identify the Peltier-based setup, a set of M experiments needs to be conducted, accumulating P steady-state periods of input-output data. Using this data, a nonparametric Best Linear Approximation $\hat{\mathbf{G}}_{\text{BLA}}$ and its sample covariance $\hat{\mathbf{C}}_{\text{BLA}}$ can be determined. Using the BLA and its sample covariance, a linear model can be estimated using the frequency domain subspace algorithm from [25] while employing the sample covariance matrix instead of the true covariance [35], by minimizing a weighted least-squares cost function with respect to all model parameters. Afterwards, a nonlinear model can be estimated by again minimizing a weighted least-squares cost function with respect to all model parameters, starting from the linear matrices acquired in Section 4.3.3. Zero initial values are considered for nonlinear coefficients. This results in a model with the structure as defined in (103). The methodology described in this chapter is used to construct a data-driven model of the Peltier-based setup in Chapter 5.

5 Data-driven model: results

In this chapter, the Peltier-based setup, introduced in Chapter 3, is identified using the methodology described in Chapter 4. Firstly, in Section 5.1 the designed excitation signal for the identification is discussed. Secondly, in Section 5.2 the chosen model structure for the Peltier-based setup is described. Section 5.3 then elaborates on the found nonparametric BLA and the resulting estimated parametric linear models. Subsequently, Section 5.4 elaborates on the found single-input-single-output (SISO) models for the Peltier-based setup with only input nonlinearities. Section 5.5 continues with the found SISO models for the Peltier-based setup when including state-dependency. Next, Section 5.6 and Section 5.7 elaborate on the possibilities to include the ambient temperature (T_{amb}) in the modeling procedure and show the resulting models that include T_{amb} . Concluding, in Section 5.8, it is discussed whether the most optimal data-driven model is obtained to compare with the physics-based model.

5.1 Excitation signal design

To be able to accurately capture the thermodynamics of the Peltier-based setup, the excitation signal has to be designed properly. Following (62), the sampling frequency f_s , number of samples per period N , and amplitudes U_k of the multisine (MS) are chosen. Also, minimum frequency f_{min} and maximum frequency f_{max} are chosen to establish the frequency range of interest for the identification.

The desired sampling frequency f_{s_d} for thermal systems is typically equal to 20 times the bandwidth, and is determined by means of $f_{s_d} = \frac{20}{\tau_D \cdot 2\pi} = 2.27$ Hz, with τ_D [s] the dominant time-constant in the output of the Peltier-based setup, determined in Appendix B.1. In order to capture non-linear harmonics for the data-driven modeling, the sampling frequency is increased by a factor of approximately 4. It is possible to increase it even more, but for now, this has no added value. The sampling frequency f_s for the data-driven modeling experiments therefore is chosen equal to 10 Hz.

To catch all thermodynamics of the setup appropriately, a desired minimum frequency equal to $f_{\text{min}_d} = \frac{1}{\tau_S \cdot 2\pi} = 4.52 \cdot 10^{-4}$ Hz is needed. Here, $\tau_S = 3.52 \cdot 10^2$ s is the slowest time-constant, which is determined in Appendix B.2. The lower-frequent regions of thermal systems contain the most rich thermodynamics. To also catch thermodynamics in the frequency range between DC and the first pole, reduce f_{min_d} by a factor of approximately 3, resulting in a f_{min} of $1.48 \cdot 10^{-4}$ Hz. Since f_{min} influences the length of the experiment through

$$f_{\text{min}} = \frac{f_s}{N}, \quad (108)$$

this automatically comes down to a total number of samples per period N of $6.75 \cdot 10^4$.

The Peltier element has actuation rate limitations because high-frequent (≥ 1 Hz) switching between cooling and heating could damage the Peltier element due to thermal expansion. To determine f_{max} , firstly the cut-off frequency f_c of the Peltier-based setup is determined. This is the frequency at which energy flowing through the system starts to be attenuated rather than to be passed through, and it is determined as $f_c = \frac{1}{\tau_D \cdot 2\pi} = 1.14 \cdot 10^{-1}$ Hz. However,

during exploratory MS experiments with the setup for f_{\max} equal to f_c , it is observed that the actuation rate limitations are violated, resulting in a broken Peltier. Therefore, taking a safety factor of ± 10 into account, the maximum frequency f_{\max} is reduced to $1.02 \cdot 10^{-2}$ Hz. Since this is the first time the data-driven identification is used on the Peltier-based setup, it is accepted that the frequency range from $1.02 \cdot 10^{-2}$ Hz to $1.14 \cdot 10^{-1}$ Hz is not measured.

To obtain a model that represents reality most adequately, it is desired to obtain a model with a temperature range that covers most of its operating temperature region. As stated in Section 2.1, a temperature range from 5 °C to 90 °C is relevant for this setup. To obtain a desired amplitude spectrum, the amplitudes U_k are manually tuned.

In order to achieve the desired ΔT with the multisine excitation, several tuning steps are taken. Note, there is no ideal amplitude spectrum to be designed.

1. Multiply the amplitudes of the lowest five frequencies with a factor five to obtain a larger ΔT .
2. Multiply all amplitudes with a gain of 1.4 to obtain the needed ΔT , and a better signal-to-noise ratio.
3. Create an offset in the MS by setting the DC gain to -0.25, since the temperature range is not symmetrical around the ambient temperature.

As explained in Section 4.3.1, the periodic nature of the excitation signals enables to make a distinction between the effect of the nonlinear distortions and the measurement noise on the Best Linear Approximation [30]. Variations over P periods arise from the measurement noise, and the variations over M realizations are caused by the combination of measurement noise and stochastic nonlinear behavior.

To determine the amount of periods, and the amount of realizations to be measured, firstly, the amount of periods necessary to reject transients is determined as one. Then, to average out noise, at least two steady-state periods are needed. Since noise will also be averaged out over different realizations, three steady-state periods are measured, resulting in a total of four periods to measure per realization. This choice will be reviewed in Chapter 6.

Subsequently, to determine the effect of the nonlinear distortions, several realizations are needed. With more realizations measured, the effect of the nonlinear distortions on the BLA can be determined more accurately. However, measuring more realizations implies more time spent on experiments. Making a reasonable trade-off between the overall length of the experiments and the amount of realization measured, a total of 4 realizations is chosen. This results, combined with four periods per realization, in a total length of 30 hours per Peltier of data acquisition. This is quite lengthy to be applied in practice. This choice will also be reviewed in Chapter 6.

Concluding, for both Peltier 1 (P1) and Peltier 2 (P2), independent experiment sets of four MS realizations are conducted, each realization consisting of four periods of input-output

data. Three out of four periods are steady-state, used to estimate the nonparametric BLA in Section 5.3.

In Figure 13, the realizations of the experiment set used for the identification of Peltier 1 are given, both in the time domain and in the frequency domain. The realizations of the experiment set for Peltier 2 are different, but have equivalent properties. The resulting output of the four realizations in the time-domain for both Peltiers are provided in Figure 14.

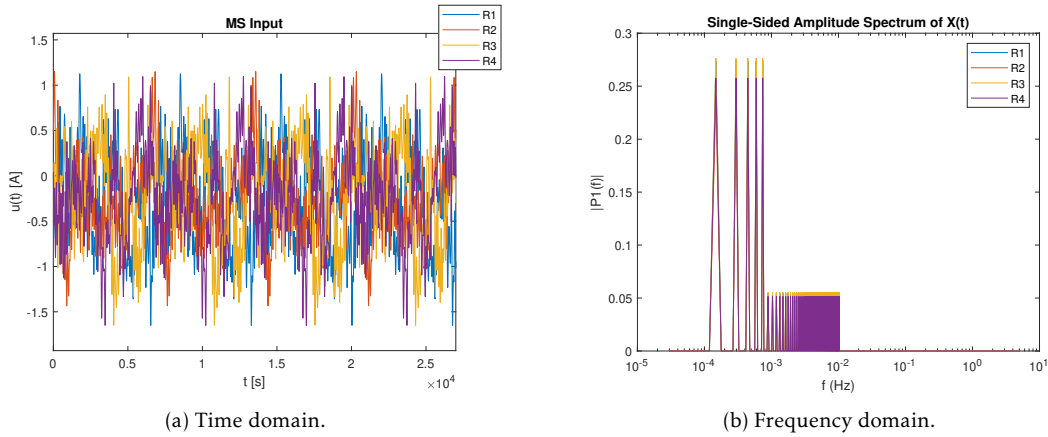


Figure 13: Four realizations of the input multisine current profile for Peltier 1 in both time and frequency domain.

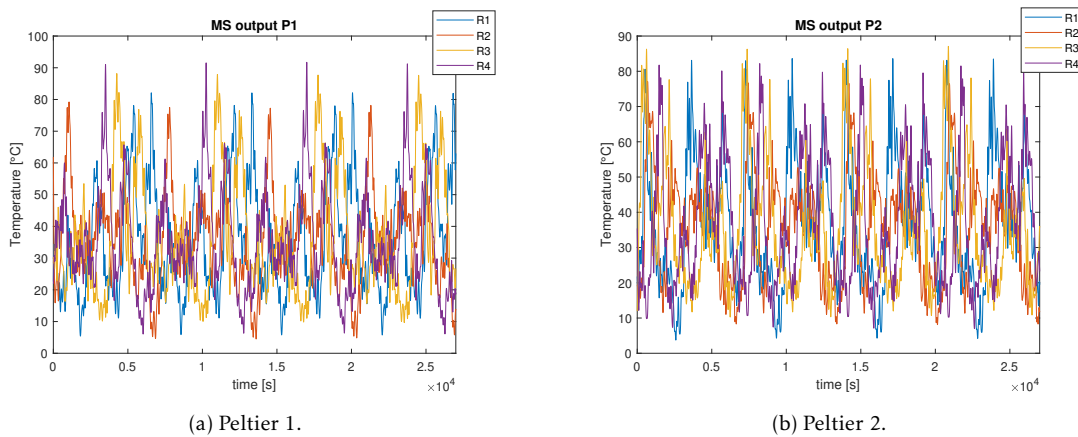


Figure 14: Output for both Peltiers after exciting it with the designed multisine realizations.

5.2 Model structure settings and validation profiles

In Section 5.2.1, the choices made regarding the data-driven modeling structure as described in (103) are discussed. Then, in Section 5.2.2 the validation profiles used to check the quality of the linear and nonlinear models are introduced.

5.2.1 Model structure settings for identification of the Peltier-based setup

As described in Section 2.1, the objective is to thermally control both points of interest on the bottom plate of the setup provided in Figure 1. Identification of the Peltier-based setup is done from Peltier input current I_{in} to output temperature at the point of interest T_{POI} , for both Peltier 1 and 2.

In [39] it is assumed that little coupling is present in the Peltier-based setup. To prove the minimal amount of coupling, the Relative Gain Array (RGA) is computed for the Peltier-based setup. The RGA provides a measure of interactions [2], and is computed as

$$\Lambda(\mathbf{G}) = \mathbf{G} \circ (\mathbf{G}^{-1})^T \quad (109)$$

where \circ is the elementwise Hadamard product of two matrices. Each element Λ_{ij} provides a scale invariant measure of the dependence of output j on input i . The elements of Λ are calculated for every frequency in the frequency range of interest, f_{min} to f_{max} . The magnitudes of the diagonal elements per frequency λ_{ii} are depicted in Figure 15. With the maximum magnitude of λ_{ii} equal to 1.025, the coupling is proven to be very little.

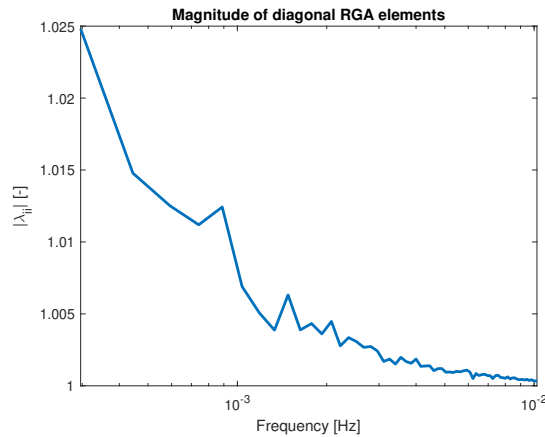


Figure 15: Magnitude of the diagonal elements of the RGA for the Peltier-based setup.

Since the amount of coupling in the system is very little, for simplicity reasons, both sides of the Peltier-based setup are identified in a SISO way.

After inspecting the thermodynamics of the Peltiers in the physics-based model in (60), it is observed that

1. The order of the nonlinearities in the state equations does not exceed two.
2. The Peltier-based setup contains no output nonlinearities.

Therefore, the maximum order of nonlinearities in the state equation for the data-driven identification is set equal to two, and no output nonlinearities in the output equation are considered.

Furthermore, for the data-driven model, firstly, two different settings will be considered regarding the amount of nonlinearities in the state equation. The first setting considers only input nonlinearities up until the power two, meaning that the model structure from (103) is reduced to

$$\begin{cases} \mathbf{x}(t+1) = \mathbf{A}\mathbf{x}(t) + \mathbf{B}\mathbf{u}(t) + \mathbf{E}\mathbf{u}^2(t) \\ \mathbf{y}(t) = \mathbf{C}\mathbf{x}(t) + \mathbf{D}\mathbf{u}(t) + \mathbf{e}(t) \end{cases}. \quad (110)$$

The resulting models will be referred to as ‘U2-SISO’ models.

The second setting considers nonlinearities in both state and input up until the power two. This means that the model structure from (103) is reduced to

$$\begin{cases} \mathbf{x}(t+1) = \mathbf{A}\mathbf{x}(t) + \mathbf{B}\mathbf{u}(t) + \mathbf{E}\zeta(t) \\ \mathbf{y} = \mathbf{C}\mathbf{x}(t) + \mathbf{D}\mathbf{u}(t) + \mathbf{e}(t) \end{cases}, \quad (111)$$

with $\zeta(t)$ equal to all monomials in $\mathbf{x}(t)$ and $\mathbf{u}(t)$ of degree two, i.e. $\zeta(t)$ for a SISO-model of model order two equals

$$\zeta(t) = [\mathbf{x}_1^2 \quad \mathbf{x}_1\mathbf{x}_2 \quad \mathbf{x}_1\mathbf{u} \quad \mathbf{x}_2^2 \quad \mathbf{x}_2\mathbf{u} \quad \mathbf{u}^2]. \quad (112)$$

The resulting models will be referred to as ‘SD-SISO’ models.

5.2.2 Validation and test profiles

To check the quality of both the linear and the nonlinear model, both a validation and a test profile are used. In order to maintain coherence between excitation and validation signals, validation is done with a multisine. Then, in order to test if the model is fit for use in handheld devices, like in [18], it is tested with a test profile, where the test profile exhibits a realistic temperature reference for the POIs.

In order to validate the model properly, an independent data set is to be used. Therefore, the estimation of the nonparametric BLA in Section 5.3.1 is done with the three out of four realizations, denoted as R_{train} , resulting in the model having no knowledge of the data in the realization used for validation, denoted as R_{val} . The final steady-state period of R_{val} is chosen as the MS validation profile. The input and output of this MS validation profile are denoted as ‘ \mathbf{u}_{val} ’ and ‘ \mathbf{y}_{val} ’ respectively.

In practice, the procedure to determine R_{train} is done parallel to that of determining the model order n . To exemplify, this is clarified in the following steps.

1. Choose R_{train} as the first, second, and third MS realization out of four.
2. Estimate a nonparametric BLA following Section 4.3.1 with R_{train} .
3. Estimate and optimize a linear parametric model following Sections 4.3.2 and 4.3.3, for different model orders n_a and subspace parameter r .
4. Save the settings of the models with the lowest validation fitting error for all model orders n_a .

5. Repeat steps 1-4 for R_{train} chosen as every other combination of three MS realizations.
6. Pick the model with the lowest validation fitting error, while striving to maintain a minimal amount of modeling parameters.

In this way, R_{train} , and therewith R_{val} , \mathbf{u}_{val} , and \mathbf{y}_{val} are determined, as well as model order n .

The test profile, denoted as ‘T-profile’, is designed to resemble a typical temperature profile for the Peltier to follow when used in handheld devices like in [18], and covers most of the operating temperature range. For this test profile, the input and output are denoted as ‘ \mathbf{u}_{test} ’ & ‘ \mathbf{y}_{test} ’ respectively. In Figure 16, \mathbf{u}_{test} is given, and \mathbf{y}_{test} for both P1 and P2 are provided in Figure 17.

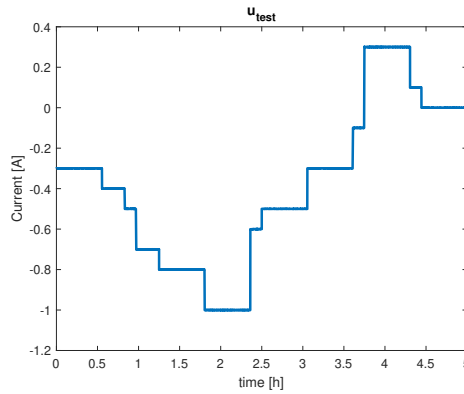
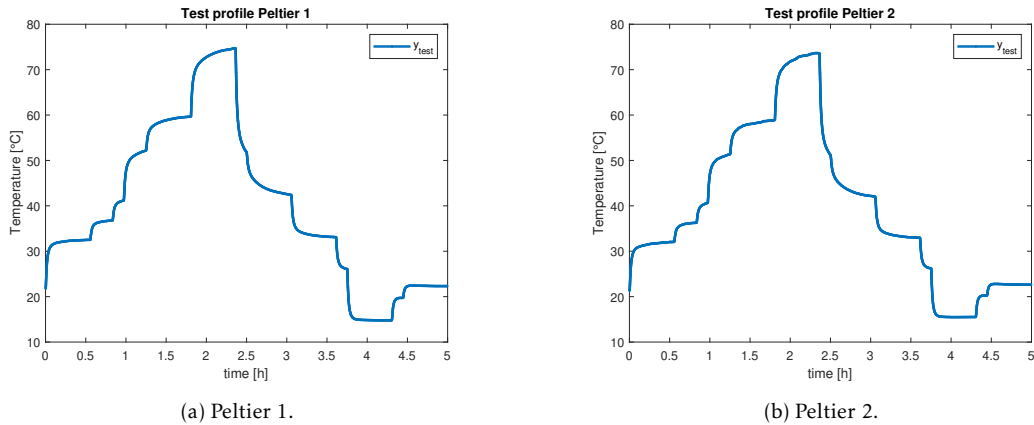


Figure 16: \mathbf{u}_{test} for both Peltiers.



(a) Peltier 1.

(b) Peltier 2.

Figure 17: \mathbf{y}_{test} for both Peltiers.

Both the validation and the test profile will be used to qualify both the linear and the non-linear model in terms of percentual error and maximum error. The percentual error for both

profiles is defined as

$$\mathbf{e}_{\%} = \frac{\text{std}(\mathbf{e})}{\text{std}(\mathbf{r})} \cdot 100\%, \quad (113)$$

with $\mathbf{e} = \mathbf{r} - \mathbf{y}$, where \mathbf{r} is the measured output \mathbf{y}_{val} or \mathbf{y}_{test} , and \mathbf{y} is the modeled output for either the MS validation profile or the T-profile. The maximum error is defined as

$$\mathbf{e}_{\text{max}} = \max(|\mathbf{e}|). \quad (114)$$

With the model structure settings chosen, the validation profile and test profile introduced, and the excitation signal for the identification designed in Section 5.1, the data-driven identification procedure can continue by estimating the nonparametric BLA and linear model matrices.

5.3 Best linear approximation & linear model estimation

In this section, the experimental data, obtained by exciting the system with the designed multisines in Section 5.1, is used to estimate a nonparametric BLA in Section 5.3.1 following the methods described in Section 4.3.1. Then, applying the methods from Sections 4.3.2 and 4.3.3, a parametric linear model is estimated in Section 5.3.2.

5.3.1 Best linear approximation: SISO

To eventually obtain the linear parametric model, firstly the nonparametric BLA is estimated following Section 4.3.1. As described in Section 5.2.2, the estimation of the nonparametric BLA is done with three out of four realizations, to ensure that the estimated model has no knowledge of the data in the validation realization R_{val} . Using the methods described in Section 4.3.1, the nonparametric best linear approximation $\hat{\mathbf{G}}_{BLA}$, total sample variance $\hat{\sigma}_{BLA}^2$ due to stochastic nonlinear contributions and noise, sample variance due to stochastic nonlinear contributions $\hat{\sigma}_{NL}^2$, and measurement noise sample variance $\hat{\sigma}_n^2$ are estimated. Figure 18 shows the estimated nonparametric BLA $\hat{\mathbf{G}}_{BLA}$, its total sample variance $\hat{\sigma}_{BLA}^2$ and noise sample variance $\hat{\sigma}_n^2$ for both Peltier 1 and 2.

For both P1 and P2, the found nonparametric BLA and its total sample variance will be used to estimate a linear parametric model in Section 5.3.2.

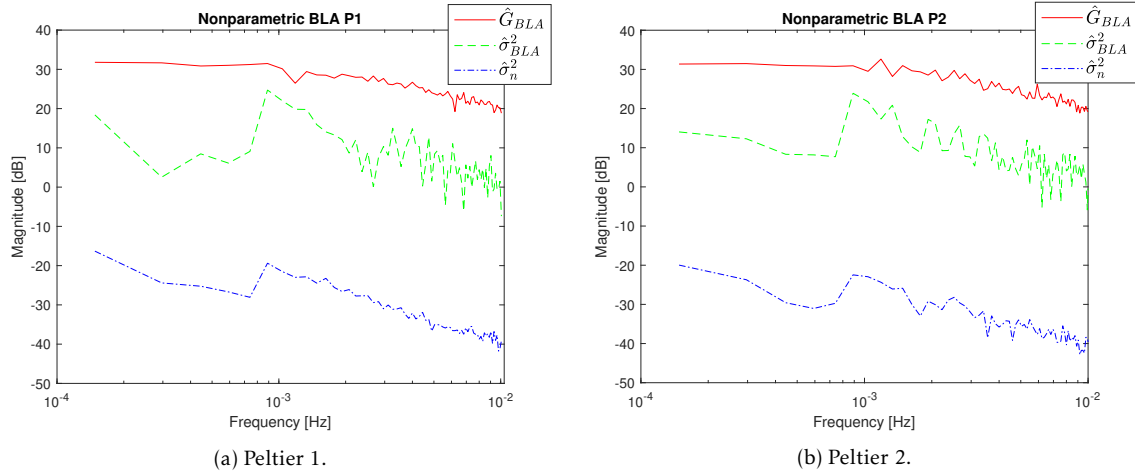


Figure 18: Nonparametric BLA, the total sample covariance due to stochastic nonlinear contributions and noise, and noise sample covariance for both Peltiers.

5.3.2 Estimation and optimization of a parametric linear model

Using the nonparametric BLA and its sample variance, a parametric linear model is estimated by minimizing the cost function V_L in (99) with respect to all model parameters, following Sections 4.3.2 and 4.3.3. To determine the final model order n , the procedure of minimizing the cost function V_L in (99) is repeated for different model orders $n_a = [1, 2, 3, 4]$. Figures 19 and 20 show the cost function V_L plotted against the subspace parameter r for both subspace models and optimized models, for model order 1 (blue), 2 (orange), 3 (yellow), and 4 (purple). Subspace models are plotted as dots, and optimized models as stars. Stabilized subspace models are encircled in gray, while unstable optimized models are encircled in color.

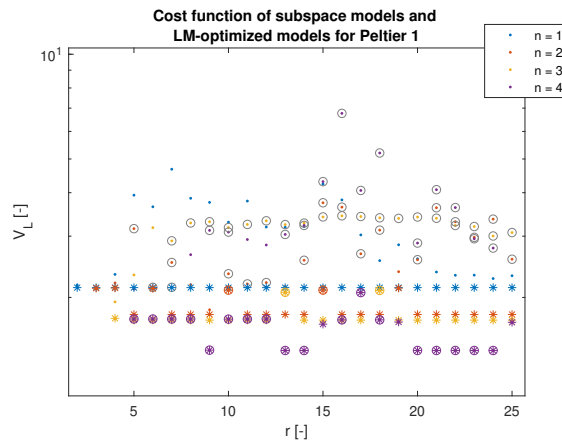


Figure 19: Cost function for (optimized) subspace models for different n and r for Peltier 1. Model order 1 in blue, 2 in orange, 3 in yellow, and 4 in purple. Subspace models are plotted as dots, and optimized models as stars. Stabilized subspace models are encircled in gray, while unstable optimized models are encircled in color.

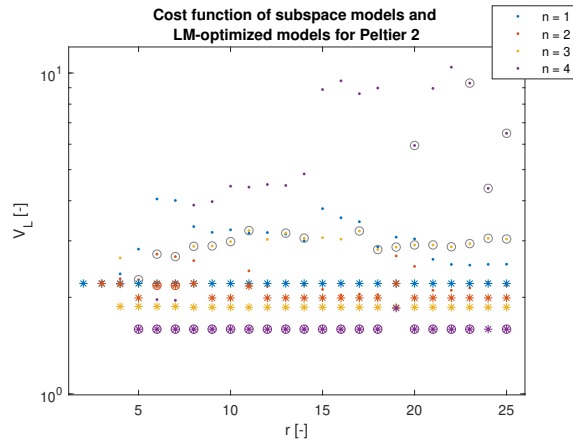


Figure 20: Cost function for (optimized) subspace models for different n and r for Peltier 2. Model order 1 in blue, 2 in orange, 3 in yellow, and 4 in purple. Subspace models are plotted as dots, and optimized models as stars. Stabilized subspace models are encircled in gray, while unstable optimized models are encircled in color.

For the identification of the Peltier-based setup, only stable models are considered. By zooming in on the optimized models in the bottom of Figures 19 and 20, the final model orders can be determined. These zoomed-in parts of Figures 19 and 20 are depicted in Figures 21 and 22.

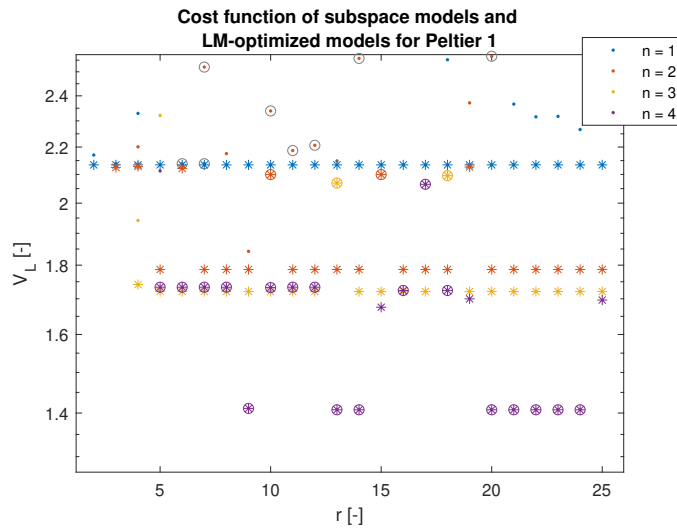


Figure 21: Zoomed in bottom part of Figure 19, to visualize the optimized models for Peltier 1 more optimal.

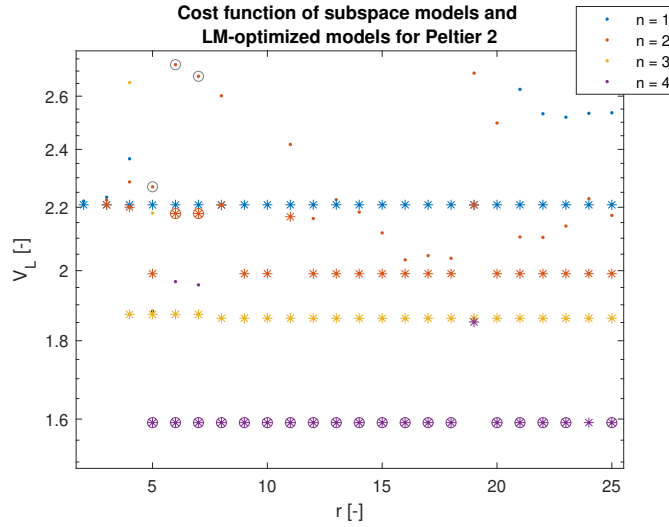


Figure 22: Zoomed in bottom part of Figure 20, to visualize the optimized models for Peltier 2 more optimal.

Preferably, the model with the lowest V_L is selected, while striving to maintain a minimal amount of modeling parameters. Also, because of the symmetry in the setup, it is desired to maintain the same model order for both Peltier 1 and 2. Figure 21 shows that the lowest cost function for Peltier 1 is achieved for $n = 4$, and $r = 13$. However, this model is unstable, and therefore not desired to use for further model identification. The decrease in V_L for the best stable model of order $n = 4$ with respect to the best stable model of order $n = 3$ is minimal. Therefore, the final model order for Peltier 1 is determined as $n = 3$. From Figure 22, the lowest cost function V_L for Peltier 2 is determined, while maintaining the same model order as for Peltier 1. The lowest cost function V_L is then achieved for $n = 3$, and $r = 8$. The final model order for Peltier 2 is therefore also determined as $n = 3$. In hindsight, if the identification for Peltier 2 had been done prior to that of Peltier 1, a model order of 4 could also have been considered. For now, this has not been done.

The resulting estimated parametric linear models for both Peltier 1 and 2 are given in Figure 23, where G_{P1} denotes the linear model for Peltier 1 and G_{P2} denotes the linear model for Peltier 2.

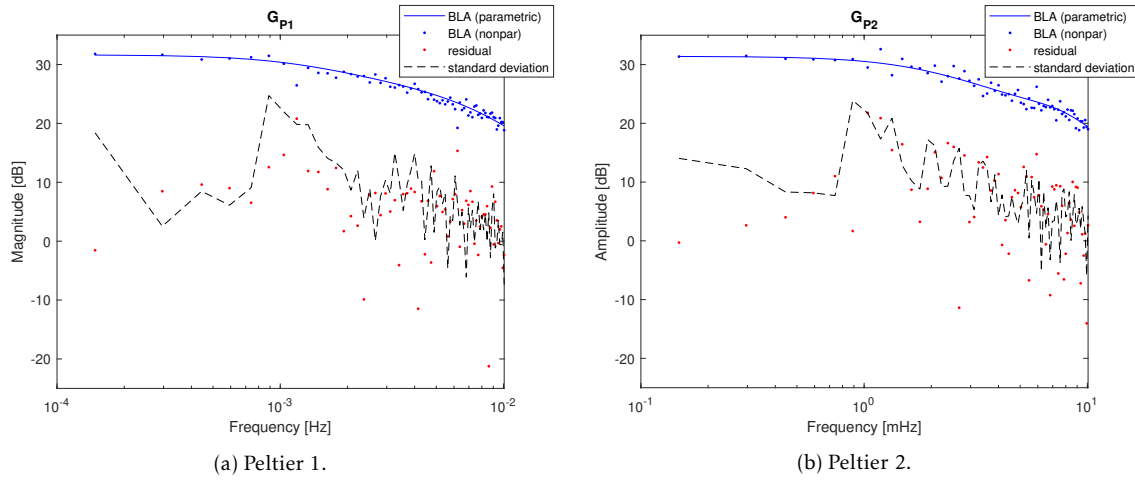


Figure 23: Resulting parametric BLA for both Peltiers: SISO.

The difference between the estimated parametric linear models for both Peltiers is probably due to the production process of the Peltier elements. The difference in the amount of solder used, and the difference in the size of pellets is considerable, as explained in Section 2.1. Table 2 gives an overview of the poles of the estimated linear models for both P1 and P2, with the corresponding natural frequencies ω_n and damping ξ .

Pole #	1	2	3
ω_n [Hz]	$8.8 \cdot 10^{-3}$	$4.07 \cdot 10^{-2}$	$8.84 \cdot 10^{-2}$
ξ [-]	1	1	1

(a) Peltier 1.

Pole #	1	2	3
ω_n [Hz]	$1.58 \cdot 10^{-2}$	$4.6 \cdot 10^{-2}$	$4.6 \cdot 10^{-2}$
ξ [-]	1	0.1241	0.1241

(b) Peltier 2.

Table 2: Natural frequencies and damping of the poles of the resulting parametric models of both Peltier 1 and Peltier 2.

For Peltier 1, a linear model is estimated with three real poles, while for Peltier 2, a linear model with one real pole and a complex pole pair is estimated. For a linear open-loop thermal system, only stable real poles are expected. Since the setup is nonlinear, as well as an amplifier and current control are applied, this expectation is not necessarily true for the Peltier-based setup. What it does demonstrate is that the data-driven identification method does not care about the symmetry in the setup, or consider the underlying physics, but solely wants to catch the IO-thermodynamics as precisely as possible. Also, it might show that the assumed symmetry of the setup is not necessarily true. This could mean that the data-driven approach of identifying two separate SISO models leads to more accurate results than the method employed for the physics-based model, where the thermal resistances of one side of the setup are estimated, and the thermal resistances of the other side are assumed to be equal, according to the symmetry.

Using the found linear model matrices as starting point, the full nonlinear model will be estimated in Section 5.4.

5.4 Resulting U2-SISO nonlinear models

To estimate a full nonlinear model, the cost function \mathbf{V}_{NL} from (105) will be minimized with respect to all model parameters, following Section 4.3.4 and considering the model structure defined in (110) as

$$\begin{cases} \mathbf{x}(t+1) = \mathbf{A}\mathbf{x}(t) + \mathbf{B}\mathbf{u}(t) + \mathbf{E}\mathbf{u}^2(t) \\ \mathbf{y}(t) = \mathbf{C}\mathbf{x}(t) + \mathbf{D}\mathbf{u}(t) + \mathbf{e}(t) \end{cases}.$$

The linear model matrices obtained in Section 5.3 are used as a starting point for $(\mathbf{A}, \mathbf{B}, \mathbf{C}, \mathbf{D})$, and zero initial values are considered for nonlinear coefficients in \mathbf{E} .

The resulting U2-SISO models for both Peltiers are validated on the MS validation profile as defined in Section 5.2.2. In Figure 24, \mathbf{Y}_{val} , the DFT of the measured output for the validation profile, is given in grey. Furthermore, $\mathbf{Y}_{val_{lin}}$, the DFT of the linear model output for the validation profile, is given in blue, and $\mathbf{Y}_{val_{NL}}$, the DFT of the nonlinear U2-SISO model output for the validation profile, is provided in green. The DFT of the linear error, ϵ_L , is equal to

$$\epsilon_L = \mathbf{Y}_{val} - \mathbf{Y}_L, \quad (115)$$

and depicted in red, while the DFT of the nonlinear error, ϵ_{NL} , is equal to

$$\epsilon_{NL} = \mathbf{Y}_{val} - \mathbf{Y}_{NL}, \quad (116)$$

and given in purple. Finally, the sample noise variance $\hat{\sigma}_n^2$ is provided in black.

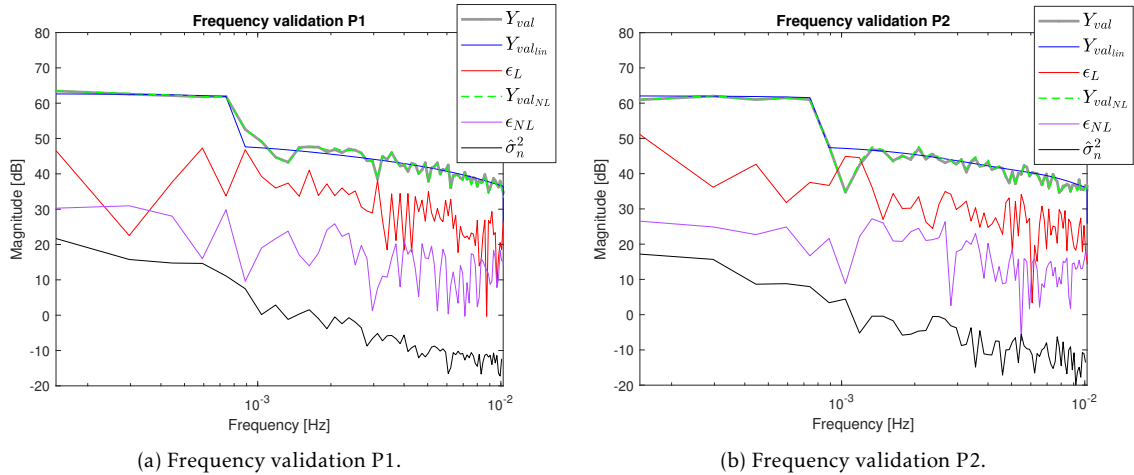


Figure 24: Frequency validation for both Peltiers: U2-SISO.

From Figure 24, it is observed that, for almost all frequencies excited, the nonlinear fit for the MS validation profile $\mathbf{Y}_{val_{NL}}$ outperforms the linear fit $\mathbf{Y}_{val_{lin}}$. To analyze the output of both the linear and the nonlinear model, as well as analyze the modeling error for both

models in more detail, the measured output and modeled output are compared in the time domain. Figure 25 shows y_{val} , the measured output for the validation profile, in grey, $y_{\text{val,lin}}$, the linear model output for the validation profile, in blue, and $y_{\text{val,NL}}$, the nonlinear U2-SISO model output for the validation profile, in green. In Figure 26, the measured output for the validation profile, y_{val} , is provided in grey, the linear error, $e_{\text{val,lin}}$, equal to

$$e_{\text{val,lin}} = y_{\text{val}} - y_{\text{val,lin}}, \quad (117)$$

is depicted in red, and the nonlinear error, $e_{\text{val,NL}}$, equal to

$$e_{\text{val,NL}} = y_{\text{val}} - y_{\text{val,NL}}, \quad (118)$$

is depicted in purple.

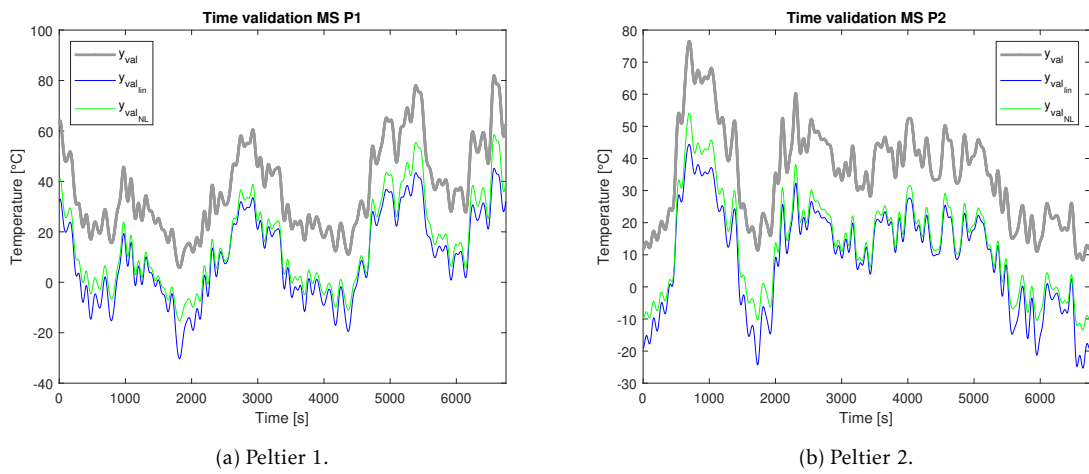


Figure 25: Time validation MS for both Peltiers: U2-SISO

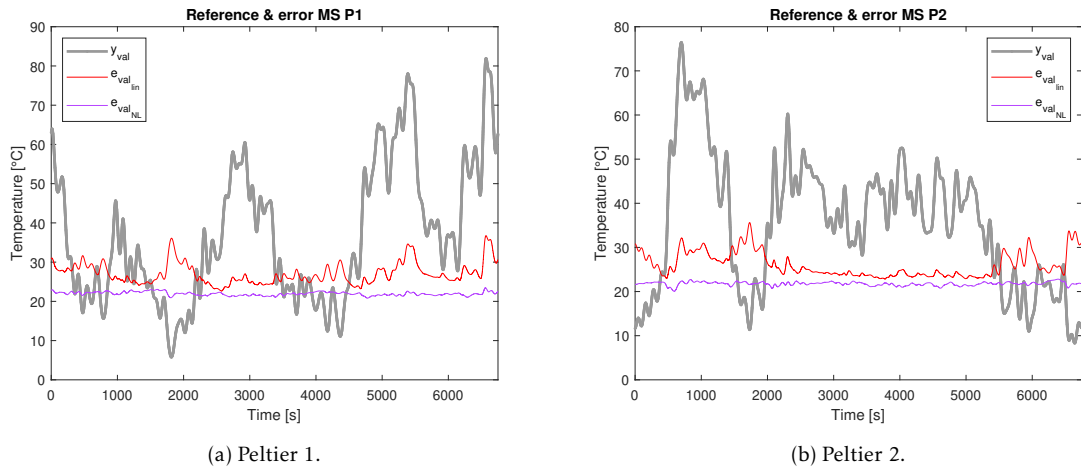


Figure 26: Output and errors for MS validation for both Peltiers: U2-SISO.

From Figures 25 and 26, it is clearly visible that the nonlinear error has become smaller than the linear error while having a smaller mean. However, a DC-like term remains, resulting in

the nonlinear fit $\mathbf{y}_{\text{val}_{\text{NL}}}$ in Figure 25 to only converge slightly towards the validation profile \mathbf{y}_{val} .

The DC-like term is explained by revisiting the thermodynamics of the physics-based model. For the physics-based model, both the Peltier input current and the ambient temperature T_{amb} are inputs to the system, with T_{amb} a non-controllable input. The data-driven model has no knowledge of T_{amb} , but it still affects the output data on which its identification is done, which results in the DC-like term for both validation and test profile.

Since the ambient temperature is measured during all experiments using a thermocouple, it is possible to incorporate it in the model. Simply adding T_{amb} in the output equation of (110) does not work, since a fluctuation in ambient temperature during experiments would be directly visible in the output, which is not desired nor realistic. Also, that way, the ambient temperature is incorporated twice, since although no knowledge of T_{amb} is present in the model structure, it still influenced the output of the experiments.

To incorporate the ambient temperature properly in the model, three different solutions are investigated, and the results are presented in the following sections. Firstly, in Section 5.5 the resulting SD-SISO models are presented, for which compensation for T_{amb} is done by including state-dependency, therefore following the model structure in (111). Secondly, in Section 5.6, the ambient temperature is included by identifying a nonlinear model around the mean of T_{amb} , after which the mean of T_{amb} is added in the output equation. This is done following the model structure from (110). The found models are referred to as ‘SD-DC-SISO’ models. Finally, in Section 5.7.1, the ambient temperature is incorporated by executing a multiple-input-single-output (MISO) identification, where T_{amb} is considered as input \mathbf{u}_2 . Firstly, a nonparametric linear model from T_{amb} to T_{POI} is estimated, using a separate experiment on the Peltier-based setup without current input. The found nonparametric BLA then is used to filter the measured ambient temperature during the MS experiments. Then, the filtered T_{amb} is deducted from the original output T_{POI} , after which a MISO parametric linear model is estimated. Finally, a full nonlinear model is estimated, extending the model structure in (111) to the MISO case, but only implementing all monomials in $\mathbf{x}(t)$ and $\mathbf{u}_1(t)$ of degree two, based on the physics-based model. Apart from evaluating the models in terms of percentual and maximum error, the practicability of the models will be assessed in terms of the robustness with respect to T_{amb} .

5.5 Resulting SD-SISO models

The full nonlinear model estimation procedure for the SD-SISO models for both Peltiers is done by minimizing cost function \mathbf{V}_{NL} from (105) with respect to all model parameters, following Section 4.3.4, and considering the model structure defined in (111) as

$$\begin{cases} \mathbf{x}(t+1) = \mathbf{A}\mathbf{x}(t) + \mathbf{B}\mathbf{u}(t) + \mathbf{E}\zeta(t) \\ \mathbf{y} = \mathbf{C}\mathbf{x}(t) + \mathbf{D}\mathbf{u}(t) + \mathbf{e}(t) \end{cases}.$$

The BLA and estimated parametric linear model matrices are identical to the ones determined in Section 5.3 for the U2-SISO models. Therefore, these linear model matrices are used as a starting point for $(\mathbf{A}, \mathbf{B}, \mathbf{C}, \mathbf{D})$. Zero initial values are considered for nonlinear coefficients in \mathbf{E} .

The resulting SD-SISO models for both Peltiers are validated on the MS validation profile as defined in Section 5.2.2. In Figure 27, \mathbf{Y}_{val} , the DFT of the measured output for the validation profile, is given in grey. Furthermore, $\mathbf{Y}_{val_{lin}}$, the DFT of the linear model output for the validation profile, is given in blue, and $\mathbf{Y}_{val_{NL}}$, the DFT of the nonlinear SD-SISO model output for the validation profile, is provided in green. The DFT of the linear error, ϵ_L , is equal to

$$\epsilon_L = \mathbf{Y}_{val} - \mathbf{Y}_L, \quad (119)$$

and depicted in red, while the DFT of the nonlinear error, ϵ_{NL} , is equal to

$$\epsilon_{NL} = \mathbf{Y}_{val} - \mathbf{Y}_{NL}, \quad (120)$$

and given in purple. Finally, the sample noise variance $\hat{\sigma}_n^2$ is provided in black.

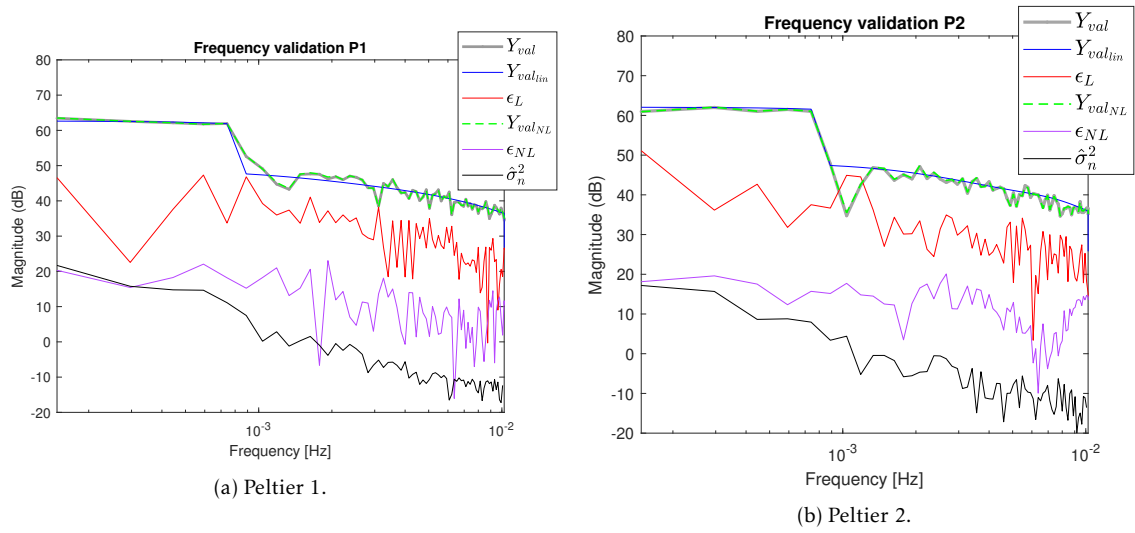


Figure 27: Frequency validation for both Peltiers: SD-SISO.

By considering the model structure defined in (111), more nonlinear terms are considered in the state equation with respect to the U2-SISO models. Figure 27 shows that the nonlinear fit for the MS validation profile $\mathbf{Y}_{val_{NL}}$ outperforms the linear fit $\mathbf{Y}_{val_{lin}}$ over the whole frequency range. For the lowest frequencies, ϵ_{NL} even approaches the magnitude of the noise sample variance, implying that the remaining error is purely due to measurement noise.

Again, to analyze the output of both the linear and the nonlinear model, as well as analyze the modeling error for both models in more detail, the measured output and modeled output are compared in the time domain. Figure 28 shows \mathbf{y}_{val} , the measured output for the validation profile, in grey, $\mathbf{y}_{val_{lin}}$, the linear model output for the validation profile, in blue, and $\mathbf{y}_{val_{NL}}$, the nonlinear SD-SISO model output for the validation profile, in green. In Figure 29, the nonlinear error, $\mathbf{e}_{val_{NL}}$, equal to

$$\mathbf{e}_{val_{NL}} = \mathbf{y}_{val} - \mathbf{y}_{val_{NL}}, \quad (121)$$

is depicted in purple.

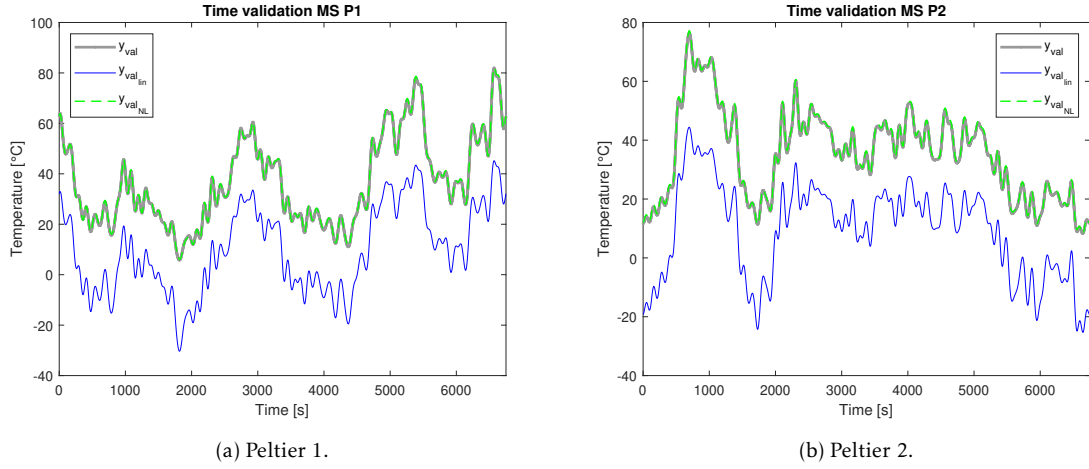


Figure 28: Time validation MS for both Peltiers: SD-SISO.

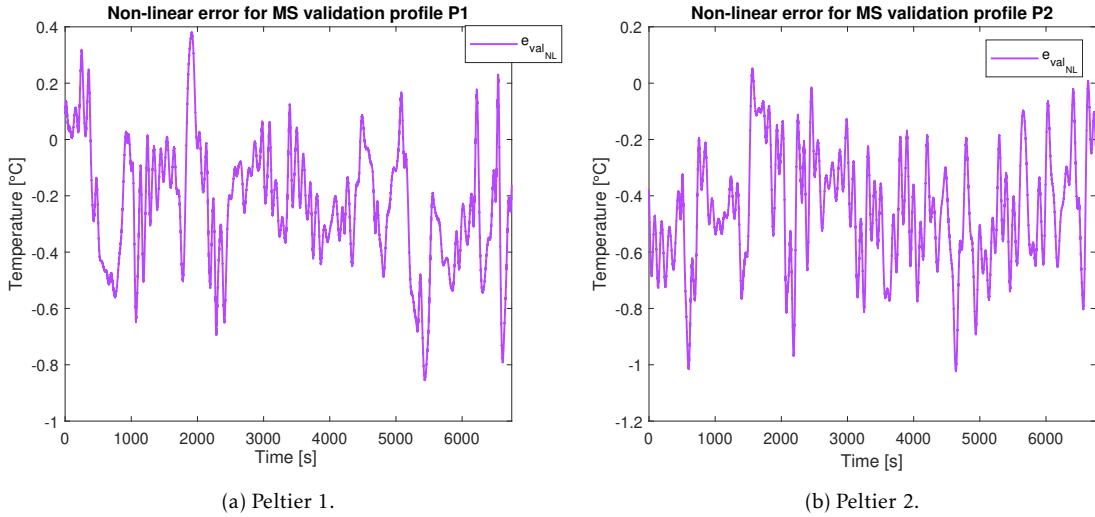


Figure 29: NL error MS validation profile for both Peltiers: SD-SISO.

From Figure 29, it is clearly visible that the DC-like residue has shrunk, therefore decreasing the modeling error. This is also visible when the model is subjected to the test profile. Figure 30 shows y_{test} , the measured output for the test profile, in grey, $y_{test_{lin}}$, the linear model output for the test profile, in blue, and $y_{test_{NL}}$, the nonlinear SD-SISO model output for the test profile, in green. In Figure 31, the nonlinear error, $e_{test_{NL}}$, equal to

$$e_{test_{NL}} = y_{test} - y_{test_{NL}}, \quad (122)$$

is provided in purple.

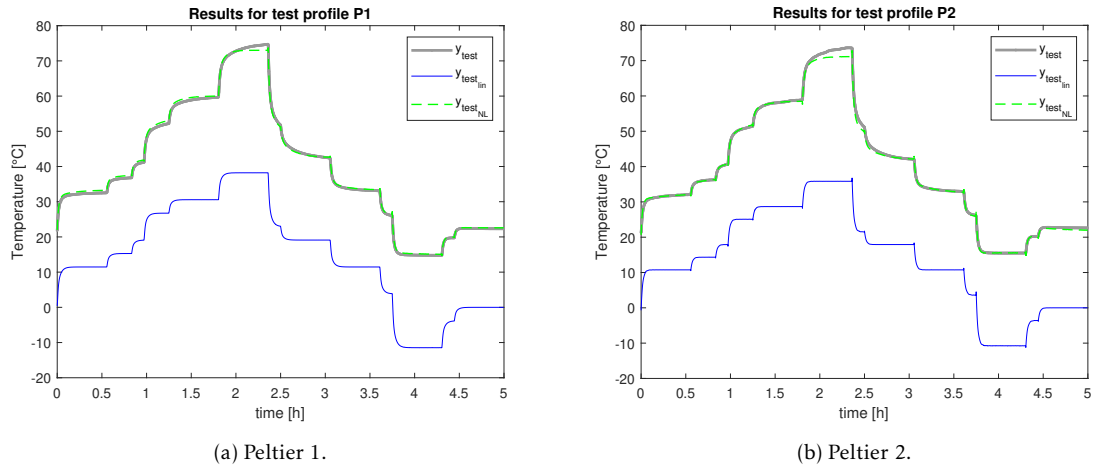


Figure 30: Output for test profile for both Peltiers: SD-SISO.

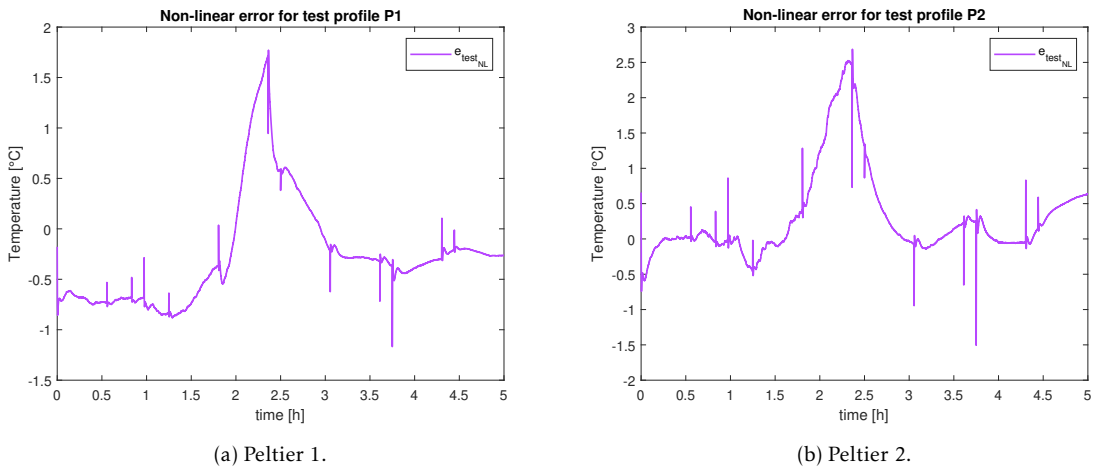


Figure 31: NL error test profile for both Peltiers: SD-SISO.

The spikes in the error profile are caused by the feedthrough term in (111). A feedthrough term in the model structure of the Peltier-based setup is odd, but it is considered in the model structure for this research because of modeling freedom. The feedthrough term for the data-driven model denotes that when a current is put into the system, it is directly visible in the output. A current input for the Peltier-based setup causes a heatload, which is never directly visible in the output, since that would mean that it is heating a state without any thermal mass. Therefore, for future research it is recommended to adapt the model structure for the identification of a thermal system to one without a feedthrough term. Furthermore, the spikes can be prevented by lowpass-filtering the input trajectories, since the model is not trained on any step-like profiles.

The quality of the final SD-SISO models in terms of percentual error and maximum error for P1 and P2 is given in Table 3 and 4. The maximum error for Peltier 1 has decreased to

0.86 °C for the validation MS profile, and the maximum error for Peltier 2 has decreased to 1.02 °C for the validation MS profile. For the test profile, the maximum error for Peltier 1 has decreased to 1.77 °C and for Peltier 2 to 2.69 °C. During transient, the errors for the test profile shows peaks up to 1.72 °C for Peltier 1 and 2.53 °C for Peltier 2.

P1	MS validation profile		Test profile	
	%	Max [°C]	%	Max [°C]
Linear model	15.77	36.76	24.52	37.06
SD-SISO	1.26	0.86	3.06	1.77

Table 3: Error margins for SD-SISO model for P1.

P2	MS validation profile		Test profile	
	%	Max [°C]	%	Max [°C]
Linear model	18.00	18.10	25.46	15.71
SD-SISO	1.35	1.02	3.75	2.69

Table 4: Error margins for SD-SISO model for P2.

In the SD-SISO models, compensation for T_{amb} is successfully done by including state-dependency. Because of the modeling freedom, the model is able to overcome the DC-like residue found for the U2-SISO models. However, since the model has no knowledge on T_{amb} , it is only valid for a certain ambient temperature, and therefore not robust to changes in T_{amb} . A rise or drop in ambient temperature during validation experiments with respect to the MS experiments results in a higher modeling error, since the model compensates for the effect of the ambient temperature it was trained on. It is therefore only a suited modeling approach for applications with little to no fluctuations in ambient temperature.

5.6 Resulting SD-DC-SISO models

To overcome the DC-like residue for the found U2-SISO models, the ambient temperature is included for the SD-DC-SISO models by identifying a nonlinear model around the mean of T_{amb} , after which the mean of T_{amb} is added in the output equation. Also, whereas until now the DC gain was omitted from the identification process, it will be included for this method, as most influence from T_{amb} is focussed around DC. This results in the model structure from (111) to adapt to

$$\begin{cases} \mathbf{x}(t+1) = \mathbf{A}\mathbf{x}(t) + \mathbf{B}\mathbf{u}(t) + \mathbf{E}\zeta(t) \\ \mathbf{y}(t) = \bar{T}_{amb} + \mathbf{C}\mathbf{x}(t) + \mathbf{D}\mathbf{u}(t) + \mathbf{e}(t) \end{cases} \quad (123)$$

with \bar{T}_{amb} the mean of T_{amb} . Since the ambient temperature differs per experiment, it is applied as follows.

1. Determine the mean of the ambient temperature separately for all MS realizations $\bar{T}_{amb_{MS}}$ and deduct it from the corresponding output y_{POI} .

2. Ascertain R_{val} , following Section 5.2.2, therewith determining the mean of the ambient temperature for the MS validation profile $\bar{T}_{amb_{val}}$.
3. Determine the mean of the ambient temperature for the test profile $\bar{T}_{amb_{test}}$.
4. Follow the procedure described in Section 4.3 to identify the nonlinear model considering the model structure defined in (123).
5. Validate the identified PNLSS model on \mathbf{u}_{val} , and add $\bar{T}_{amb_{val}}$ in the output equation.
6. Subject the identified PNLSS model to \mathbf{u}_{test} , and add $\bar{T}_{amb_{test}}$ in the output equation.

Again, the resulting SD-DC-SISO models for both Peltiers are validated on the MS validation profile as defined in Section 5.2.2. In Figure 32, \mathbf{Y}_{val} , the DFT of the measured output for the validation profile, is given in grey. Furthermore, $\mathbf{Y}_{val_{lin}}$, the DFT of the linear model output for the validation profile, is given in blue, and $\mathbf{Y}_{val_{NL}}$, the DFT of the nonlinear SD-SISO model output for the validation profile, is provided in green. The DFT of the linear error, ϵ_L , is equal to

$$\epsilon_L = \mathbf{Y}_{val} - \mathbf{Y}_L, \quad (124)$$

and depicted in red, while the DFT of the nonlinear error, ϵ_{NL} , is equal to

$$\epsilon_{NL} = \mathbf{Y}_{val} - \mathbf{Y}_{NL}, \quad (125)$$

and given in purple. Finally, the sample noise variance $\hat{\sigma}_n^2$ is provided in black.

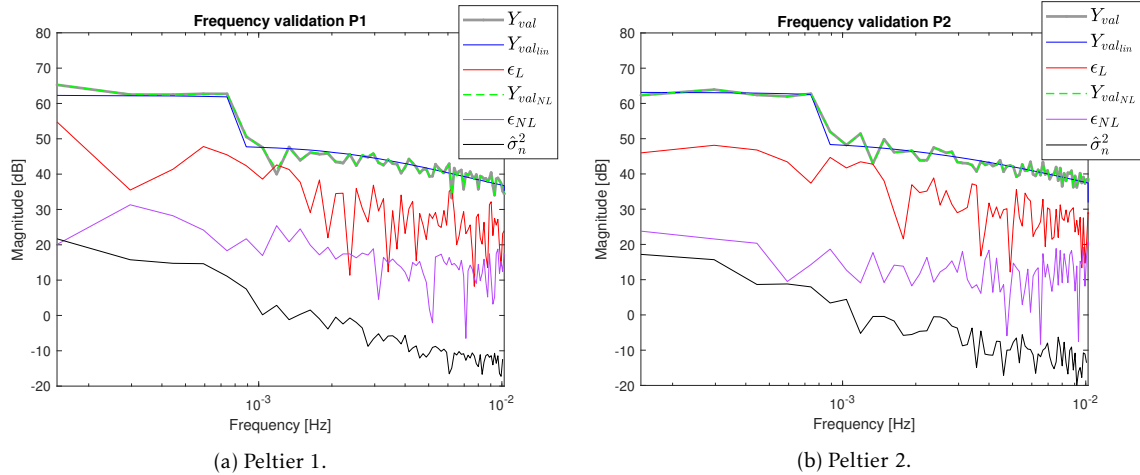


Figure 32: Frequency validation for both Peltiers: SD-DC-SISO.

By considering the model structure defined in (123), more nonlinear terms are considered in the state equation with respect to the U2-SISO models. Also, by modeling it around the mean of the ambient temperature measured during experiments, the model does not have to compensate for it in the output. From Figure 32, it can be observed that the nonlinear fit for

the MS validation profile $\mathbf{Y}_{\text{val}_{\text{NL}}}$ outperforms the linear fit $\mathbf{Y}_{\text{val}_{\text{lin}}}$ over the whole frequency range.

Again, to analyze the output of both the linear and the nonlinear model, as well as analyze the modeling error for both models in more detail, the measured output and modeled output are compared in the time domain. Figure 33 shows \mathbf{y}_{val} , the measured output for the validation profile, in grey, $\mathbf{y}_{\text{val}_{\text{lin}}}$, the linear model output for the validation profile, in blue, and $\mathbf{y}_{\text{val}_{\text{NL}}}$, the nonlinear SD-DC-SISO model output for the validation profile, in green. In Figure 34, the nonlinear error, $\mathbf{e}_{\text{val}_{\text{NL}}}$, equal to

$$\mathbf{e}_{\text{val}_{\text{NL}}} = \mathbf{y}_{\text{val}} - \mathbf{y}_{\text{val}_{\text{NL}}}, \quad (126)$$

is depicted in purple.

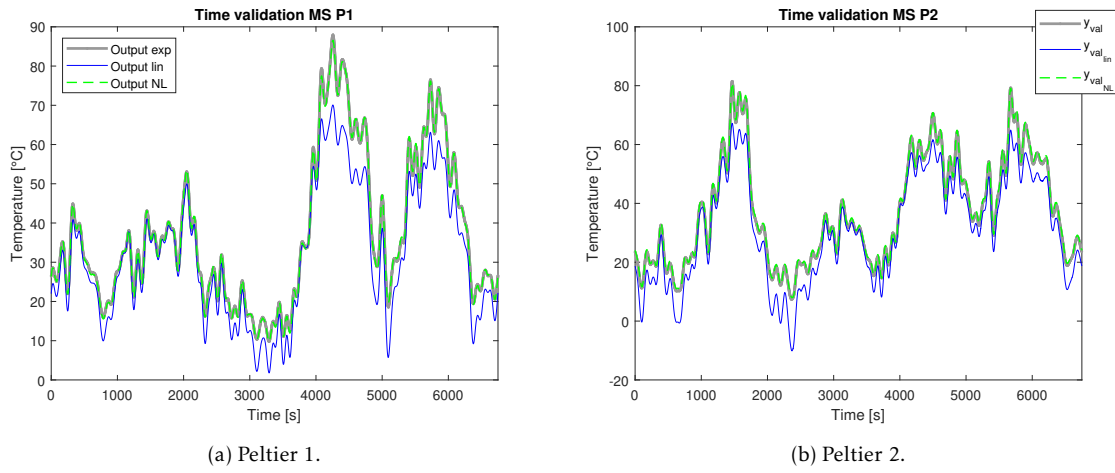


Figure 33: Time validation MS for both Peltiers: SD-DC-SISO.

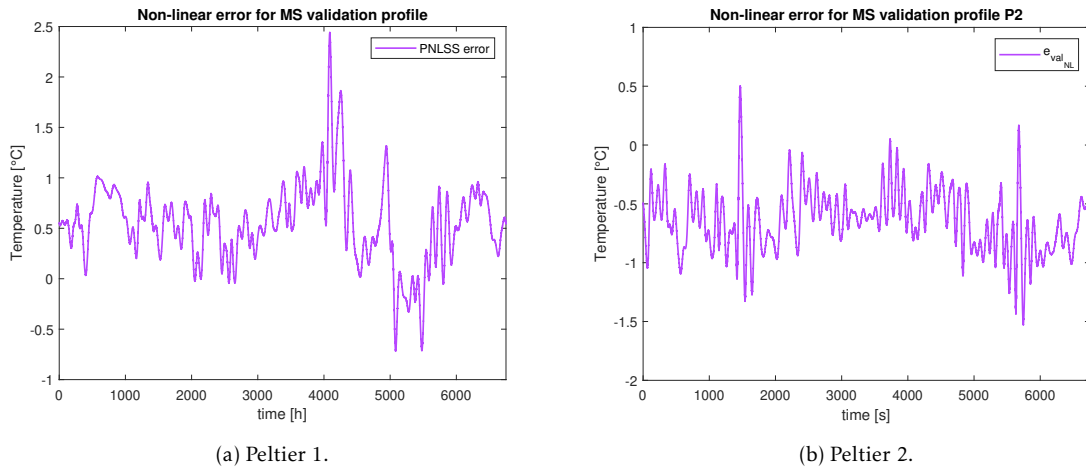


Figure 34: NL error MS validation profile for both Peltiers: SD-DC-SISO.

From Figure 34, it is clearly visible that the DC-like residue has shrunk when compared

to the U2-SISO models, therefore decreasing the modeling error. However, the maximum error has increased with respect to the SD-SISO case. This is also visible when the model is subjected to the test profile. Figure 35 shows \mathbf{y}_{test} , the measured output for the test profile, in grey, $\mathbf{y}_{\text{test}_{\text{lin}}}$, the linear model output for the test profile, in blue, and $\mathbf{y}_{\text{test}_{\text{NL}}}$, the nonlinear SD-DC-SISO model output for the test profile, in green. In Figure 36, the nonlinear error, $\mathbf{e}_{\text{test}_{\text{NL}}}$, equal to

$$\mathbf{e}_{\text{test}_{\text{NL}}} = \mathbf{y}_{\text{test}} - \mathbf{y}_{\text{test}_{\text{NL}}}, \quad (127)$$

is provided in purple.

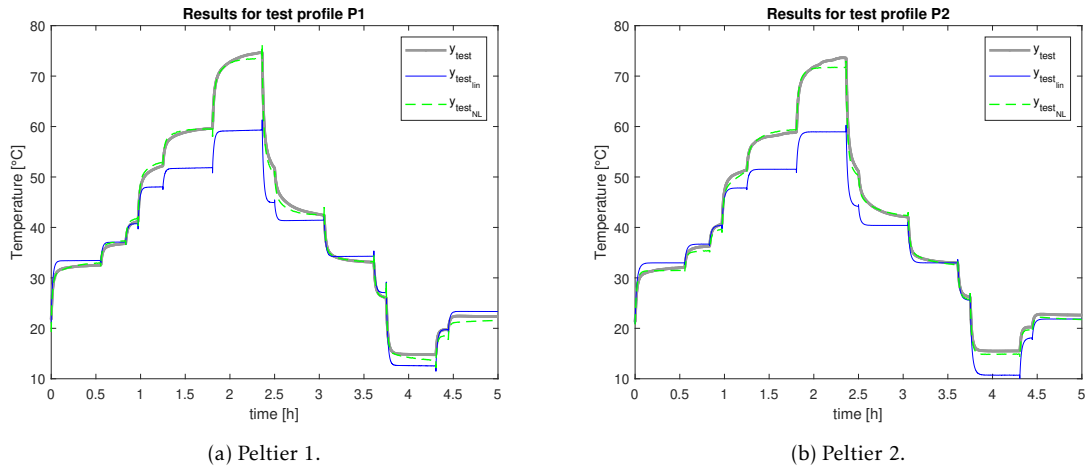


Figure 35: Output for test profile for both Peltiers: SD-DC-SISO.

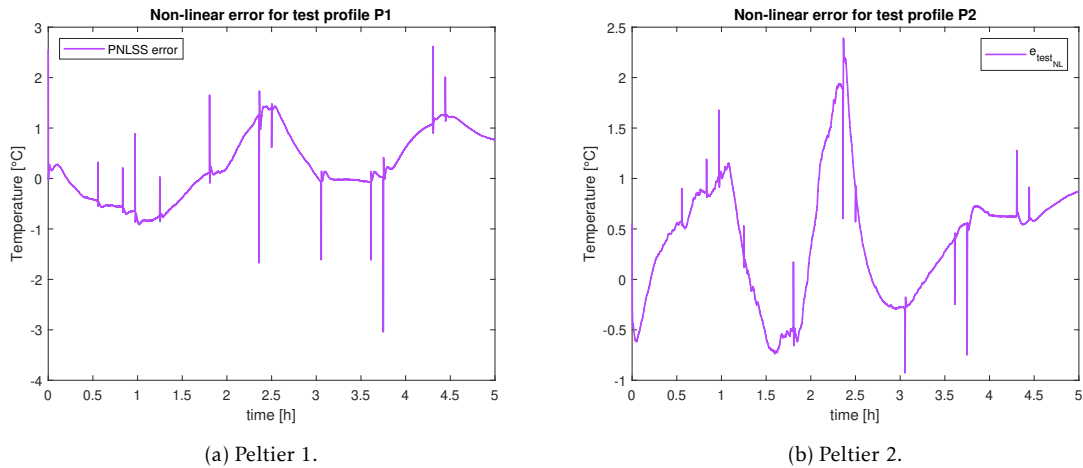


Figure 36: NL error test profile for both Peltiers: SD-DC-SISO.

As before, the spikes in the error profile are caused by the feedthrough term in (123). See the previous section for more details. The quality of the final SD-DC-SISO models in terms of percentual error and maximum error for P1 and P2 is given in Tables 5 and 6.

P1	MS validation profile		Test profile	
	%	Max [°C]	%	Max [°C]
Linear model	21.23	17.90	27.59	15.41
SD-DC-SISO	2.12	2.44	3.71	3.04

Table 5: Error margins for SD-DC-SISO model for P1.

P2	MS validation profile		Test profile	
	%	Max [°C]	%	Max [°C]
Linear model	17.86	17.52	25.46	14.71
SD-DC-SISO	1.45	1.53	3.51	2.39

Table 6: Error margins for SD-DC-SISO model for P2.

The maximum error for Peltier 1 has decreased to 2.44 °C for the validation MS profile, and the maximum error for Peltier 2 has decreased to 1.53 °C for the validation MS profile. For the test profile, the maximum error for Peltier 1 has decreased to 3.04 °C and for Peltier 2 to 2.39 °C. During transient, the errors for the test profile shows peaks up to 1.43 °C for Peltier 1 and 2.19 °C for Peltier 2.

Compensation for T_{amb} is successfully done by identifying models around the mean of the ambient temperature. In this way, the models are able to compensate for the DC-like residue found for the U2-SISO models. When compared to the SD-SISO models, this results for P1 in an increase in maximum error for the MS validation profile by factor 2.86, and an increase in maximum error for the T-profile validation by factor 1.72. For P2 this results in an increase in maximum error for the MS validation profile by factor 1.49, while the maximum error for the T-profile validation decreases by factor 0.89. In comparison to the SD-SISO models, SD-DC-SISO models have more but limited knowledge on T_{amb} , since these only incorporate its mean. The SD-DC-SISO models are therefore only valid for a certain range of ambient temperatures, and therefore little robust to changes in T_{amb} . A rise or drop in ambient temperature during experiments is averaged out, so there is no direct influence on the output. However, if these models are used for an experimental setup in a totally different environment, with an ambient temperature that is 5 °C higher compared to T_{amb} the model is validated on, it would not work properly. It is therefore a suited modeling approach for applications with little fluctuation in ambient temperature. The accepted fluctuation for the modeling method to be proper is determined by the magnitude of error that the user allows the model to obtain.

5.7 Increasing robustness with respect to the ambient temperature

For the methods used so far to be useful for applications with more fluctuation in ambient temperature, more robustness with respect to the ambient temperature is needed. To achieve this, a MISO identification is executed, where T_{amb} is considered as input \mathbf{u}_2 . The procedure and the resulting SD-MISO models are explained in Section 5.7.1. Since the ambient temperature is non-controllable, the validation profile and test profile are measured

at a certain ambient temperature, and are not easily adapted. In order to check the robustness of the SD-MISO modeling procedure with respect to different ambient temperature, offline experiments are done. These offline experiments are simulations, performed with the physics-based model of [39], and the procedure will be elaborated on in Section 5.7.2.

5.7.1 Resulting SD-MISO models

To arrive at the final SD-MISO models, firstly, a nonparametric linear model from T_{amb} to T_{POI} is estimated, using a separate set of experiments. In these experiments the ambient temperature and the temperature at the POI are measured, without exciting the Peltier element. The nonparametric BLA from T_{amb} to T_{POI} is estimated following the methods described in 4.3.1 for both Peltier 1 and 2, and given in Figure 37. To check whether the estimated nonparametric BLA is properly conducted, it should look like a first order system and have a gain of 1 (= 0 dB) around DC, since when no current is applied, the setup will eventually obtain the same temperature as T_{amb} . Note that the DC term is not visible in Figure 37, since it is plotted on a logarithmic scale. The DC gain for the estimated nonparametric BLAs for the ambient temperature to the output for Peltier 1 and Peltier 2 are off by $1.82 \cdot 10^{-2} \%$ and $2.76 \cdot 10^{-2} \%$ respectively, which is an accepted error margin.

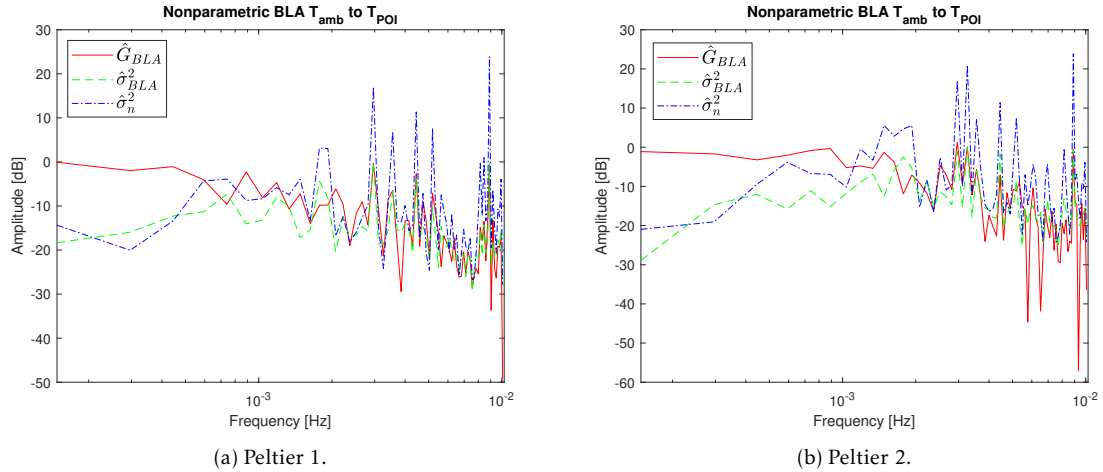


Figure 37: Nonparametric BLA and its sample covariance for T_{amb} to T_{POI} for both Peltiers: SD-MISO.

The found nonparametric BLA from T_{amb} to T_{POI} now is used to filter the measured ambient temperature during the MS experiments. Then, the filtered T_{amb} is deducted from the original output T_{POI} .

To determine the model order n , the procedure of minimizing the cost function V_L in (99) is repeated for different model orders $n_a = [1, 2, 3, 4]$. Since the experiments are done separately, the sample variance $\hat{\sigma}_{\text{BLA}}^2$ is not used as a weighting in (99) for the estimation of the linear models.

Figures 38 and 39 show the cost function V_L plotted against the subspace parameter r for

both subspace models and optimized models, for model order 1 (blue), 2 (orange), 3 (yellow), and 4 (purple). Subspace models are plotted as dots, and optimized models as stars. Stabilized subspace models are encircled in gray, while unstable optimized models are encircled in color.

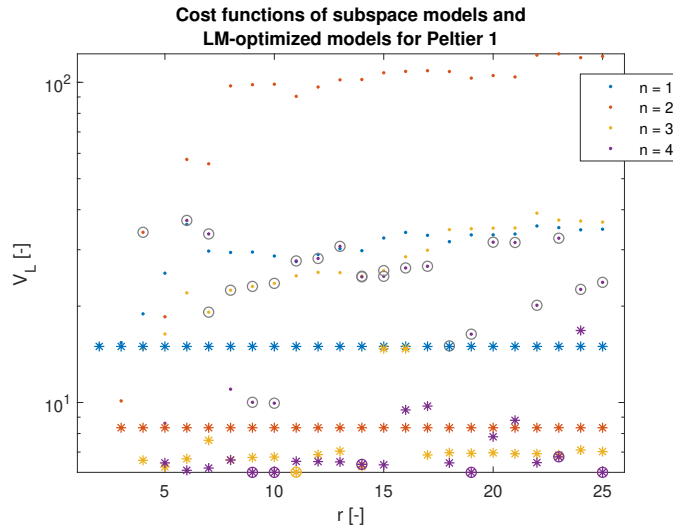


Figure 38: Cost function for (optimized) MISO subspace models for different n and r for Peltier 1. Model order 1 in blue, 2 in orange, 3 in yellow, and 4 in purple. Subspace models are plotted as dots, and optimized models as stars. Stabilized subspace models are encircled in gray, while unstable optimized models are encircled in color.

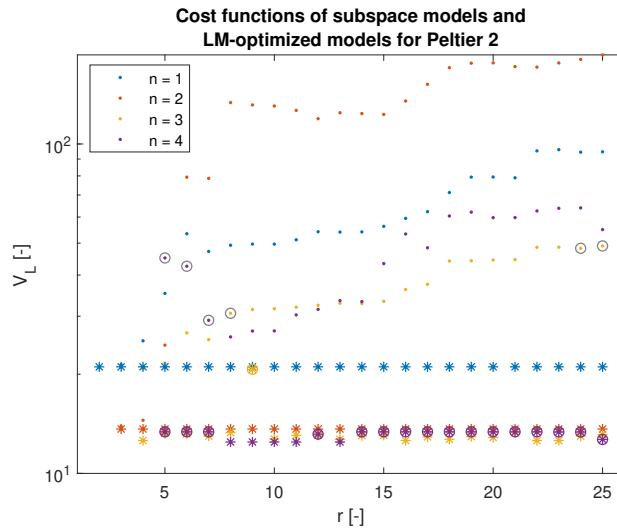


Figure 39: Cost function for (optimized) MISO subspace models for different n and r for Peltier 2. Model order 1 in blue, 2 in orange, 3 in yellow, and 4 in purple. Subspace models are plotted as dots, and optimized models as stars. Stabilized subspace models are encircled in gray, while unstable optimized models are encircled in color.

By zooming in on the optimized models in the bottom of Figures 38 and 39, the final model orders can be determined. These zoomed-in parts of Figures 38 and 39 are depicted in Figures 40 and 41.

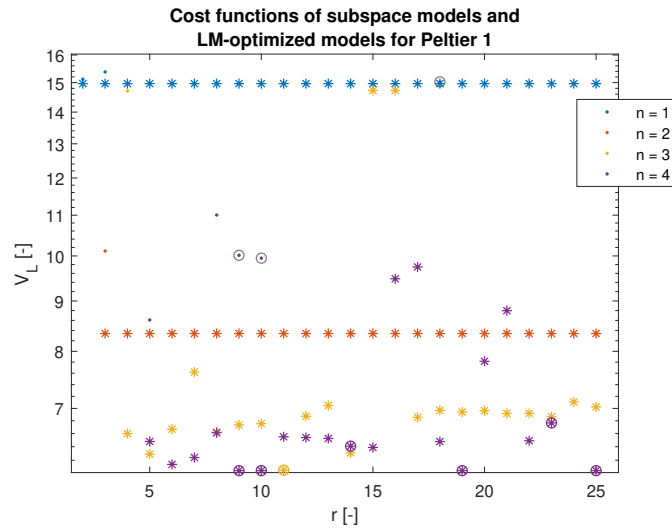


Figure 40: Zoomed in bottom part of Figure 38, to visualize the optimized models for Peltier 1 more optimal.

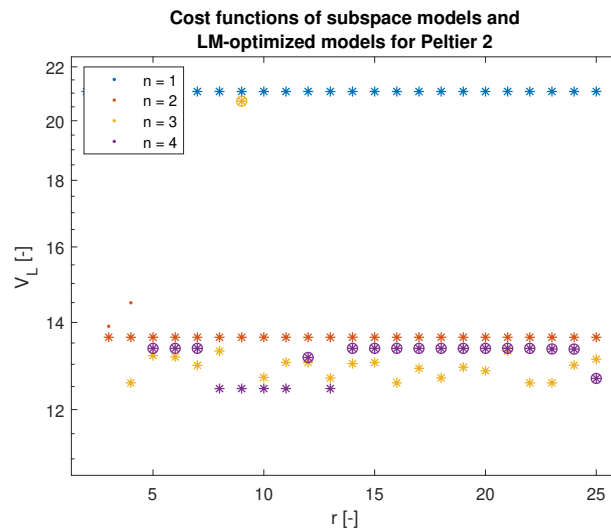


Figure 41: Zoomed in bottom part of Figure 39, to visualize the optimized models for Peltier 2 more optimal.

Again, preferably, the model with the lowest V_L is selected, while striving to maintain a minimal amount of modeling parameters. Also, because of the symmetry of the setup, it is desired to maintain the same model order for both Peltier 1 and 2. The decrease in V_L for the best stable model of order $n = 4$ with respect to the best stable model of order $n = 3$ is

minimal for both Peltiers. Taking this into account, from Figure 40 and 41, the final model order for the SD-MISO model for both Peltier 1 and 2 is determined as $n = 3$.

Next, a MISO parametric linear model is estimated by minimizing the cost function V_L in (99) with respect to all model parameters, following Sections 4.3.2 and 4.3.3.

The resulting estimated linear parametric models for both Peltiers can be found in Figure 42. G_{11} denotes the estimated parametric linear model from I_{in} to T_{POI} and G_{21} denotes the estimated parametric linear model from T_{amb} to T_{POI} . Note that the estimated DC term is not visible in this plot, since it plotted on a logarithmic scale. The found linear model matrices are used as starting point for the nonlinear model estimation. Again, the difference between the estimated parametric linear MISO models for both Peltiers is probably due to the production process of the Peltier elements as explained in Section 2.1.

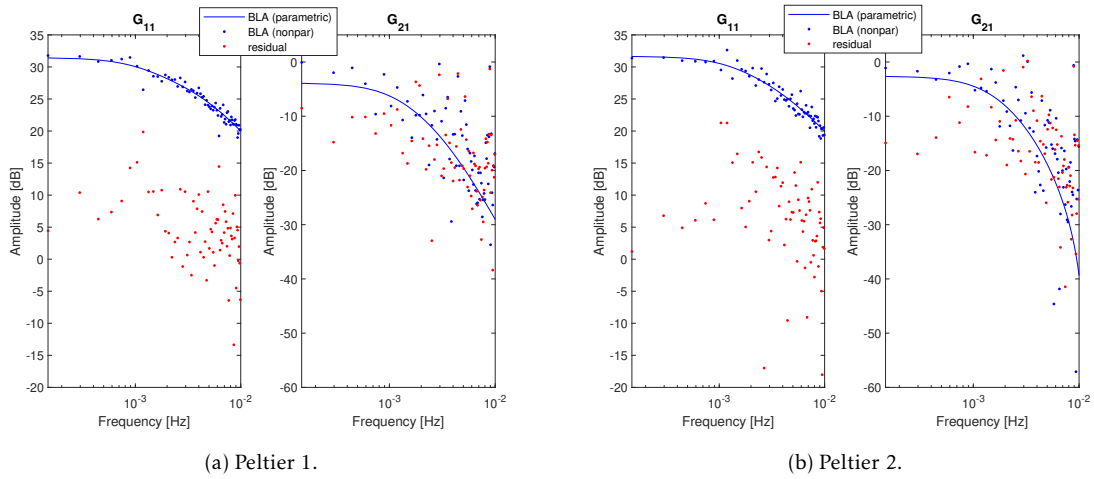


Figure 42: Resulting parametric linear BLA for both Peltiers: SD-MISO.

Finally, a full nonlinear model is estimated, extending the model structure in (111) to the MISO case. Analyzing the physics-based model from [39] clarifies that no nonlinear terms including the ambient temperature are present. Therefore, for the SD-MISO models, only the monomials in $\mathbf{x}(t)$ and $\mathbf{u}_1(t)$ of degree two are included in $\zeta(t)$. This results in the model structure from (111) to adapt to

$$\begin{cases} \mathbf{x}(t+1) = \mathbf{A}\mathbf{x}(t) + \mathbf{B}\mathbf{u}(t) + \mathbf{E}\zeta(t) \\ \mathbf{y}(t) = \mathbf{C}\mathbf{x}(t) + \mathbf{D}\mathbf{u}(t) + \mathbf{e}(t) \end{cases}, \quad (128)$$

with $\zeta(t)$ equal to the monomials in $\mathbf{x}(t)$ and $\mathbf{u}_1(t)$ of degree two, as

$$\zeta(t) = \begin{bmatrix} \mathbf{x}_1^2 & \mathbf{x}_1\mathbf{x}_2 & \mathbf{x}_1\mathbf{x}_3 & \mathbf{x}_1\mathbf{u}_1 & \mathbf{x}_2^2 & \mathbf{x}_2\mathbf{x}_3 & \mathbf{x}_2\mathbf{u}_1 & \mathbf{x}_3^2 & \mathbf{x}_3\mathbf{u}_1 & \mathbf{u}_1^2 \end{bmatrix}. \quad (129)$$

The resulting SD-MISO models for both Peltiers are validated on the MS validation profile as defined in Section 5.2.2. Since the model now has two inputs, the validation profile is extended with $\mathbf{u}_{2_{val}}$, being the ambient temperature during the MS validation profile. In

Figure 43, \mathbf{Y}_{val} , the DFT of the measured output for the validation profile, is given in grey. Furthermore, $\mathbf{Y}_{val_{lin}}$, the DFT of the linear model output for the validation profile, is given in blue, and $\mathbf{Y}_{val_{NL}}$, the DFT of the nonlinear SD-SISO model output for the validation profile, is provided in green. The DFT of the linear error, ϵ_L , is equal to

$$\epsilon_L = \mathbf{Y}_{val} - \mathbf{Y}_L, \quad (130)$$

and depicted in red, while the DFT of the nonlinear error, ϵ_{NL} , is equal to

$$\epsilon_{NL} = \mathbf{Y}_{val} - \mathbf{Y}_{NL}, \quad (131)$$

and given in purple. Finally, the sample noise variance $\hat{\sigma}_n^2$ is provided in black.

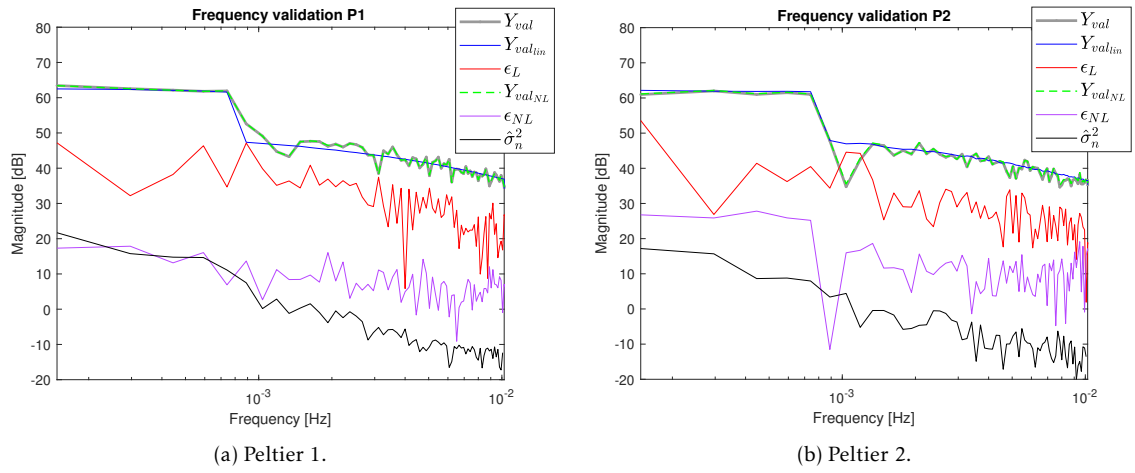


Figure 43: Frequency validation for both Peltiers: SD-MISO.

By considering the model structure defined in (128), a SD-MISO model is estimated, where T_{amb} is an input. In this way, the influence of the ambient temperature is included over the whole frequency range, instead of purely by a DC term. In Figure 43, it can be observed that the nonlinear fit for the MS validation profile $\mathbf{Y}_{val_{NL}}$ outperforms the linear fit $\mathbf{Y}_{val_{lin}}$ over the whole frequency range.

Again, to analyze the output of both the linear and the nonlinear model, as well as analyze the modeling error for both models in more detail, the measured output and modeled output are compared in the time domain. Figure 44 shows \mathbf{y}_{val} , the measured output for the validation profile, in grey, $\mathbf{y}_{val_{lin}}$, the linear model output for the validation profile, in blue, and $\mathbf{y}_{val_{NL}}$, the nonlinear SD-MISO model output for the validation profile, in green. In Figure 45, the nonlinear error, $\mathbf{e}_{val_{NL}}$, equal to

$$\mathbf{e}_{val_{NL}} = \mathbf{y}_{val} - \mathbf{y}_{val_{NL}}, \quad (132)$$

is provided in purple.

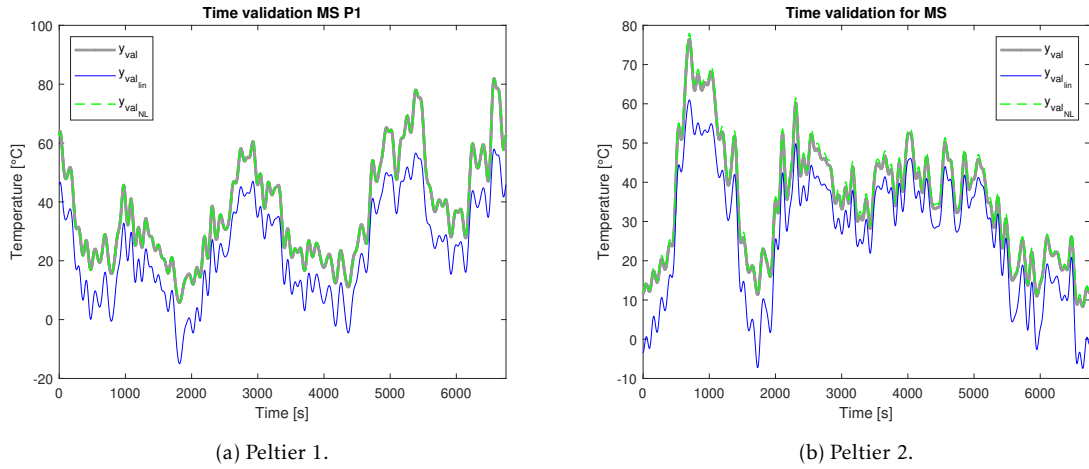


Figure 44: Time validation MS for both Peltiers: SD-MISO.

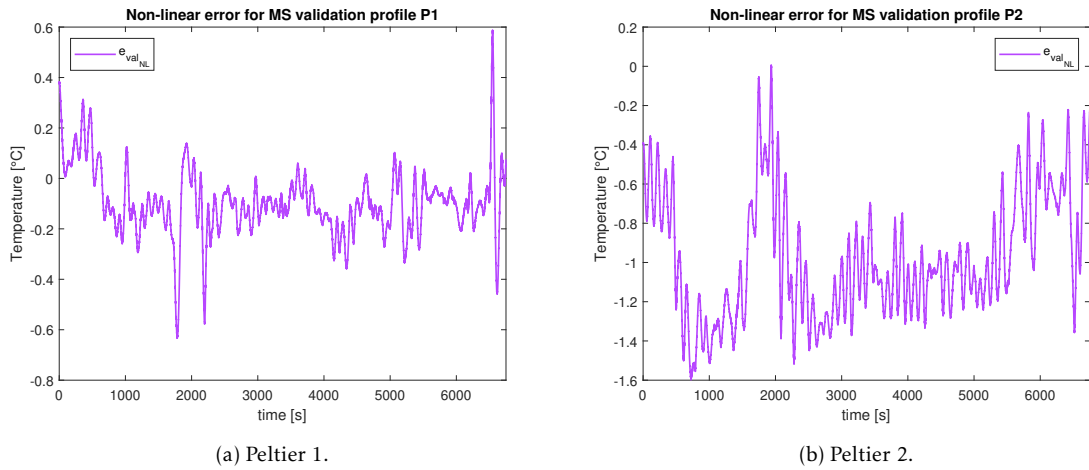


Figure 45: NL error MS validation profile for both Peltiers: SD-MISO.

From Figure 45, it is clearly visible that the DC-like residue has shrunk, therefore decreasing the modeling error. This is also visible when the model is subjected to the test profile. Figure 46 shows \mathbf{y}_{test} , the measured output for the test profile, in grey, $\mathbf{y}_{\text{test}_{\text{lin}}}$, the linear model output for the test profile, in blue, and $\mathbf{y}_{\text{test}_{\text{NL}}}$, the nonlinear SD-MISO model output for the test profile, in green. In Figure 47, the nonlinear error, $\mathbf{e}_{\text{test}_{\text{NL}}}$, equal to

$$\mathbf{e}_{\text{test}_{\text{NL}}} = \mathbf{y}_{\text{test}} - \mathbf{y}_{\text{test}_{\text{NL}}}, \quad (133)$$

is depicted in purple.

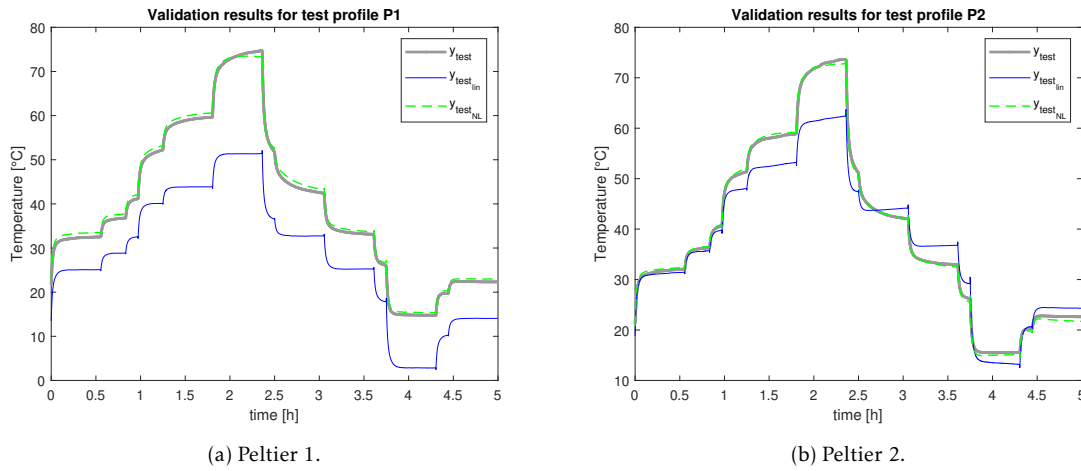


Figure 46: Output for test profile for both Peltiers: SD-MISO.

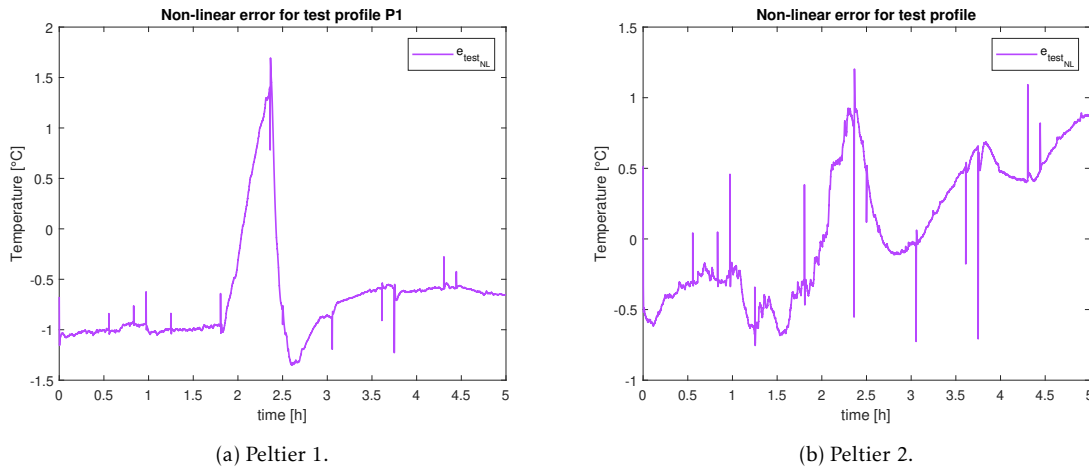


Figure 47: NL error test profile for both Peltiers: SD-MISO.

As before, the spikes in the error profile are caused by the feedthrough term in (128). See Section 5.5 for more details. The quality of the final SD-MISO models for P1 and P2 are given in Table 7 and 8 in terms of percentual error and maximum error. The maximum error for Peltier 1 has decreased to 0.63 °C for the validation MS profile, and the maximum error for Peltier 2 has decreased to 1.60 °C for the validation MS profile. For the test profile, the maximum error for Peltier 1 has decreased to 1.69 °C and for Peltier 2 to 1.20 °C. During transient, the errors for the test profile shows a peaks up to 0.93 °C for Peltier 2. The maximum error for Peltier 1 is not because of these peaks during steep current changes. The differences between the estimated data-driven models for both Peltiers, and the error margins obtained, are probably caused by the production process of the Peltier elements. The difference in the amount of solder used, and the difference in the size of pellets is considerable, as explained in Section 2.1.

P1	MS validation profile		Test profile	
	%	Max [°C]	%	Max [°C]
Linear model	15.90	24.03	25.57	23.34
SD-MISO	0.78	0.63	2.80	1.69

Table 7: Error margins for SD-MISO model for P1.

P2	MS validation profile		Test profile	
	%	Max [°C]	%	Max [°C]
Linear model	21.71	18.62	23.64	11.38
SD-MISO	2.09	1.60	2.76	1.20

Table 8: Error margins for SD-MISO model for P2.

Compensation for T_{amb} is successfully done by identifying a separate nonparametric model from T_{amb} to T_{POI} . Then, the found nonparametric BLA from T_{amb} to T_{POI} is used to filter the measured ambient temperature during the MS experiments. Next, the filtered T_{amb} is deducted from the original output T_{POI} , after which a MISO parametric identification is done. The model has proper knowledge of T_{amb} , and is therefore considered robust and a suited modeling approach for applications encountering fluctuation in ambient temperature.

Since the ambient temperature is non-controllable, the validation profile and test profile are measured at certain ambient temperatures. Using the current setup, T_{amb} cannot easily be adapted during experiments, although this would be useful to check the validity of the final SD-MISO models for different ambient temperatures. This will therefore be done by performing offline experiments with the physics-based model of [39]. The results are discussed in Section 5.7.2.

5.7.2 Validation method through offline experiments

To check the validity of the methods used to obtain the final SD-MISO models in terms of its robustness with respect to different ambient temperatures, a set of offline experiments is performed. These offline experiments are simulations, performed with the physics-based model of [39]. The methods used are identical to those described in Section 5.7.1. However, because the physics-based model was designed with a Peltier of type TEC-[39], and therefore has different properties, a different set of multisines is designed and used for the identification.

Using these offline experiments, a MISO Polynomial NonLinear State Space (PNLSS) model is identified, denoted as the SD-MISO-OFFLINE model. After identification, the SD-MISO-OFFLINE model firstly is validated on a MS validation profile. Then, it is subjected to four different test trajectories, to check its robustness with respect to the ambient temperature. These test trajectories all have identical current input profiles, equal to that of the test profile as used before, while performed at different ambient temperature. The first test profile is an offline experiment conducted at a T_{amb} profile similar to the one measured during the

validation experiment in Section 5.7.1. The second, third, and fourth test are done with the same ambient temperature profile but now increased by +5 °C, -5 °C, and +10 °C respectively.

The resulting SD-MISO-OFFLINE model is validated on the MS validation profile as defined in Section 5.2.2. The validation profile is extended with $u_{2_{\text{val}}}$, being the ambient temperature during the validation profile. In Figure 48a, \mathbf{Y}_{val} , the DFT of the measured output for the validation profile, is given in grey. Furthermore, $\mathbf{Y}_{\text{val}_{\text{lin}}}$, the DFT of the linear model output for the validation profile, is given in blue, and $\mathbf{Y}_{\text{val}_{\text{NL}}}$, the DFT of the nonlinear SD-MISO-OFFLINE model output for the validation profile, is provided in green. The DFT of the linear error, ϵ_L , is equal to

$$\epsilon_L = \mathbf{Y}_{\text{val}} - \mathbf{Y}_L, \quad (134)$$

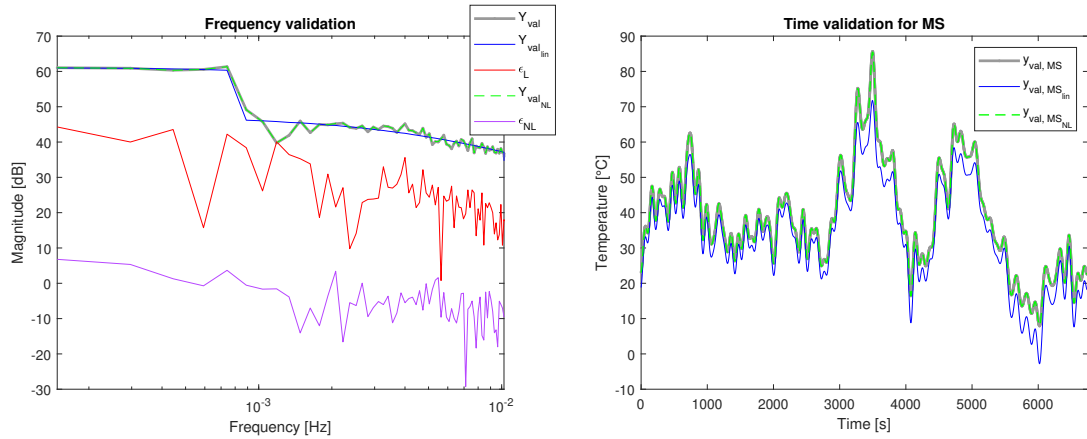
and depicted in red, while the DFT of the nonlinear error, ϵ_{NL} , is equal to

$$\epsilon_{\text{NL}} = \mathbf{Y}_{\text{val}} - \mathbf{Y}_{\text{NL}}, \quad (135)$$

and given in purple. Figure 48b shows $\mathbf{y}_{\text{val,MS}}$, the measured output for the validation profile, in grey, $\mathbf{y}_{\text{val,MS}_{\text{lin}}}$, the linear model output for the validation profile, in blue, and $\mathbf{y}_{\text{val,MS}_{\text{NL}}}$, the nonlinear SD-MISO-OFFLINE model output for the validation profile, in green. In Figure 49, the nonlinear error, $\mathbf{e}_{\text{val}_{\text{NL}}}$, equal to

$$\mathbf{e}_{\text{val}_{\text{NL}}} = \mathbf{y}_{\text{val}} - \mathbf{y}_{\text{val}_{\text{NL}}}, \quad (136)$$

is provided in purple.



(a) Frequency validation Peltier 1: SD-MISO-OFFLINE.

(b) Time validation Peltier 1: SD-MISO-OFFLINE.

Figure 48: Frequency validation and time validation on MS validation profile for Peltier 1: SD-MISO-OFFLINE.

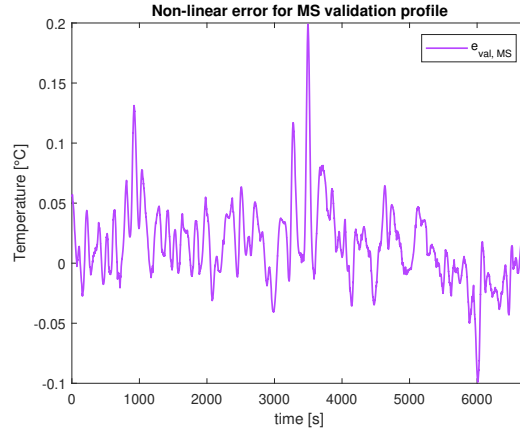


Figure 49: NL error for MS validation profile for Peltier 1: SD-MISO-OFFLINE.

It is clear from Figure 49 that the resulting error for the MS validation profile is very small. To prove the robustness with respect to the ambient temperature, and therewith the correctness of the method used for implementing the ambient temperature in the SD-MISO models, the found nonlinear model is subjected to the four test profiles.

Figure 50a shows $\mathbf{y}_{\text{test1}}$, the measured output for the first test profile, in grey, $\mathbf{y}_{\text{test1}_{\text{lin}}}$, the linear model output for the first test profile, in blue, and $\mathbf{y}_{\text{test1}_{\text{NL}}}$, the nonlinear SD-MISO-OFFLINE model output for the first test profile, in green. Figures 50b, 51a, and 51b show the measured output, linear model output and SD-MISO-OFFLINE model output for respectively the second, third and fourth test profile. The nonlinear error for the first test profile, $\mathbf{e}_{\text{test1}}$, equal to

$$\mathbf{e}_{\text{test1}} = \mathbf{y}_{\text{test1}} - \mathbf{y}_{\text{test1}_{\text{NL}}}, \quad (137)$$

is depicted in Figure 52a. Figures 52b, 53a, and 53b depict the nonlinear error for respectively the second, third and fourth test profile.

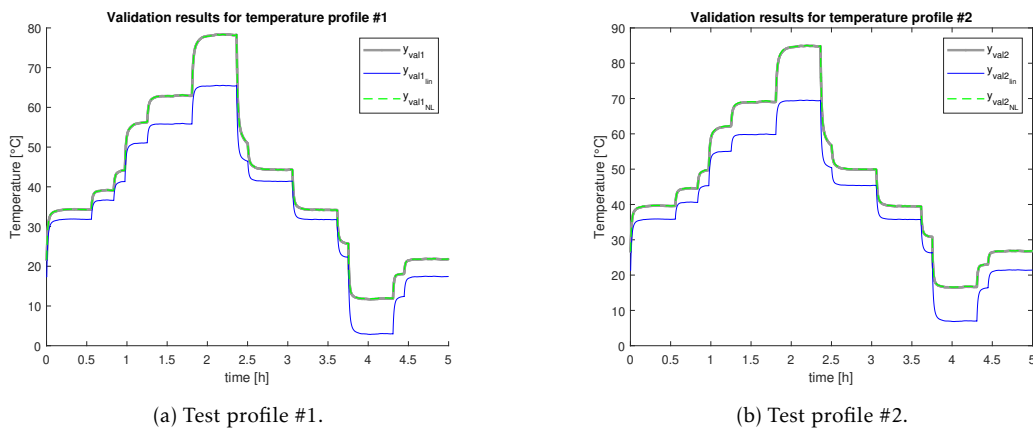
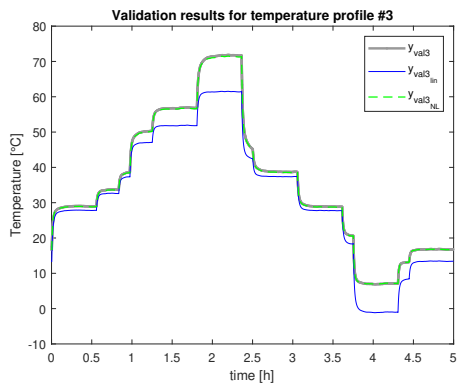
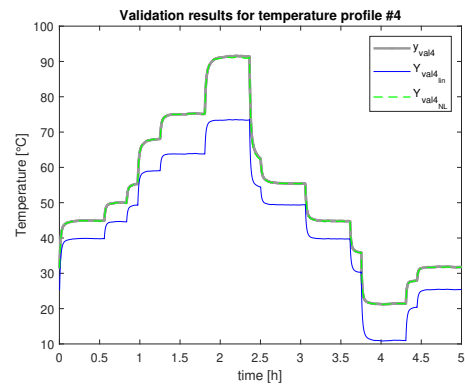


Figure 50: Measured output (grey), linear model output (blue), and nonlinear SD-MISO-OFFLINE model output (green) for test profiles #1 and #2.

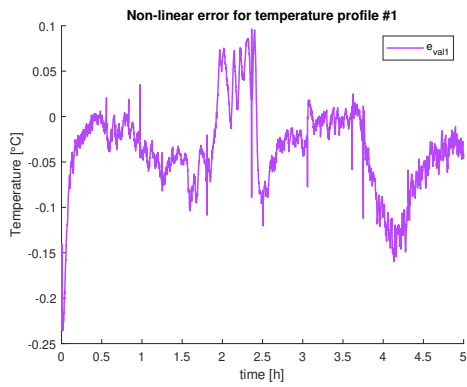


(a) Test profile #3.

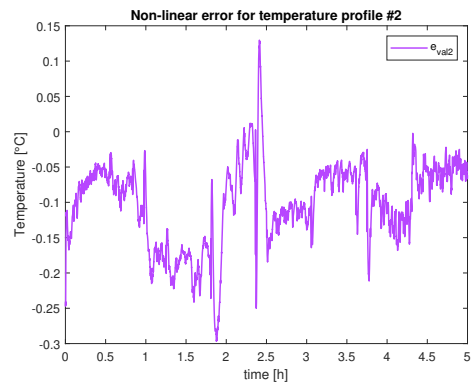


(b) Test profile #4.

Figure 51: Measured output (grey), linear model output (blue), and nonlinear SD-MISO-OFFLINE model output (green) for test profiles #3 and #4.

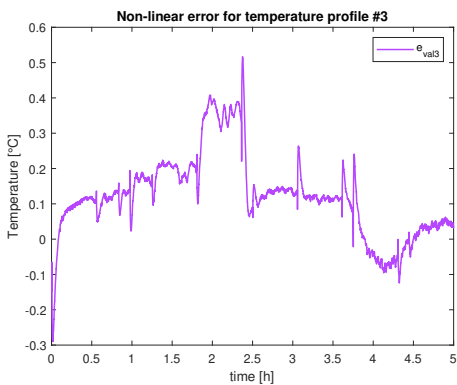


(a) Test profile #1.

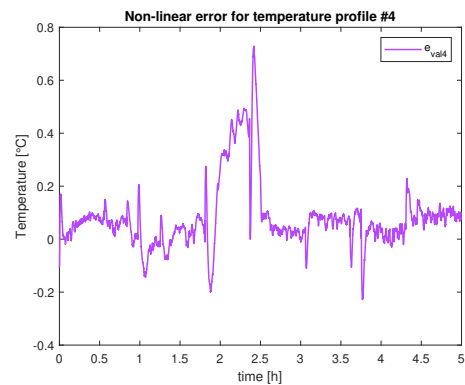


(b) Test profile #2.

Figure 52: Nonlinear error for the SD-MISO-OFFLINE model for test profiles #1 and #2.



(a) Test profile #3.



(b) Test profile #4.

Figure 53: Nonlinear error for the SD-MISO-OFFLINE model for test profiles #3 and #4.

The quality of the final offline SD-MISO-OFFLINE models in terms of percentual error and maximum error is given in Tables 9 and 10. As can be seen, for all validation profiles, the highest maximum error for all validation profiles is 0.73 °C. This is for validation profile #4, of which the ambient temperature is 10 °C off compared to the initial MS offline experiments. Therefore, it can be concluded that the method used to obtain the SD-MISO model in Section 5.7.1 results in a model that is robust with respect to changes in ambient temperature. What strikes from Tables 9 and 10 is that the SD-MISO-OFFLINE model manages an increase in ambient temperature of 10 °C for the validation profile more optimal than a decrease of 5 °C in ambient temperature. This might be the result of the focus on higher temperatures in the data acquired for identification, or due to the fact that Peltier elements become more efficient for higher temperatures.

P1	MS		Test #1		Test #2	
	%	Max [°C]	%	Max [°C]	%	Max [°C]
Linear model	13.26	13.99	16.51	12.86	17.51	15.45
SD-MISO-OFFLINE	0.22	0.20	0.24	0.24	0.29	0.30

Table 9: Error margins for SD-MISO offline model: MS, validation profile #1 and #2.

P1	Test #3		Test #4	
	%	Max [°C]	%	Max [°C]
Linear model	15.81	10.31	18.74	18.06
SD-MISO-OFFLINE	0.62	0.52	0.63	0.73

Table 10: Error margins for SD-MISO offline model: validation profile #3 and #4.

If it is desired to research the effect of T_{amb} more thoroughly, the setup could be adapted to obtain control over the ambient temperature, and multisine excitations could be designed for the ambient temperature as well. That way, a true MISO identification could be done. This, however, is out of scope for the current research and is left as a recommendation for future research.

5.8 Conclusion

In this chapter, several data-driven models of the Peltier-based setup, as introduced in Section 2.1, have been presented. After carefully designing the multisine excitation signal, and performing the experiments, the model structure settings are explained. Following the initial modeling structure, it is learned that the influence of the ambient temperature had not yet been incorporated correctly into the model. To either overcome the effect of it, or include it into the model structure, three different solutions have been presented. The errors for both the validation profile and the test profile are given in Tables 11 and 12.

P1	Validation MS		Validation T-profile	
	%	Max [°C]	%	Max [°C]
SD-SISO	1.3	0.86	3.06	1.77
SD-DC-SISO	2.12	2.44	3.71	3.04
SD-MISO	0.78	0.63	2.80	1.69

Table 11: Error margins for all data-driven models for both the validation profile and the test profile for Peltier 1.

P2	Validation MS		Validation T-profile	
	%	Max [°C]	%	Max [°C]
SD-SISO	1.35	1.02	3.75	2.69
SD-DC-SISO	1.45	1.53	3.51	2.39
SD-MISO	2.09	1.60	2.76	1.20

Table 12: Error margins for all data-driven models for both the validation profile and the test profile for Peltier 2.

The SD-SISO models overcome the effect of T_{amb} by including state-dependency in the model structure. This results for P1 in a maximum error for the MS validation profile of 0.86 °C, and a maximum error for the T-profile validation of 1.77 °C. For P2 this results in a maximum error for the MS validation profile of 1.02 °C, and a maximum error for the T-profile of 2.69 °C. However, since the models for both Peltiers have no knowledge on T_{amb} , these are only valid for a certain ambient temperature, and therefore not robust to fluctuations in T_{amb} . The modeling approach used for the SD-SISO models is therefore only suited for applications with little to no fluctuations in ambient temperature.

The found SD-DC-SISO models incorporate T_{amb} by identifying a model around the mean of the ambient temperature. When compared to the SD-SISO models, this results for P1 in an increase in maximum error for the MS validation profile by factor 2.86, and an increase in maximum error for the T-profile validation by factor 1.72. For P2 this results in an increase in maximum error for the MS validation profile by factor 1.49, while the maximum error for the T-profile validation decreases by factor 0.89. In comparison to the SD-SISO models, SD-DC models have more but limited knowledge on T_{amb} , since these only incorporate its mean. The SD-SISO models are therefore only valid for a certain range of ambient temperatures, and therefore little robust to changes in T_{amb} . If the Peltier-based setup were to be used in a totally different environment, with an ambient temperature that is 5 °C higher, it would not work properly. The modeling approach used for the SD-DC-SISO models is therefore also only a suited modeling approach for applications with little fluctuation in ambient temperature. The accepted fluctuation in T_{amb} for the modeling method to be suited is determined by the magnitude of error that the user allows the model to have.

For the final SD-MISO models, compensation for T_{amb} is successfully done by identifying a separate nonparametric model from T_{amb} to T_{POI} . The found nonparametric BLA from T_{amb} to T_{POI} then is used to filter the measured ambient temperature during the MS experiments.

Following, the filtered T_{amb} is deducted from the original output T_{POI} , and a MISO identification is done. When compared to the SD-DC-SISO models, this results for P1 in a decrease in error for the MS validation profile by factor 3.86, and a decrease in error for the T-profile validation by factor 1.8. For P2 this results in an increase in error for the MS validation profile by a factor 1.04, while the error for the T-profile validation decreases by factor 1.99. In comparison to the SD-DC-SISO models, SD-MISO models have proper knowledge of T_{amb} and are therefore considered robust to changes in T_{amb} . The modeling approach used for the SD-MISO models is therefore suited for applications encountering fluctuation in ambient temperature. Furthermore, compared to the other modeling methods, the resulting SD-MISO models obtain the smallest error for the T-profile, designed to resemble a typical temperature profile for the Peltier to follow when used in handheld devices like in [18]. The robustness with respect to changes in T_{amb} of this approach has been investigated on a set of offline experiments, which establishes the correct estimation of the effect of the ambient temperature on the model output. Improvements could be done by investigating the effect of T_{amb} more thoroughly. By adapting the setup to obtain control over the ambient temperature, and designing MS excitations for T_{amb} , a true MISO identification could be done. This, however, is out of scope for the current research and is left as a recommendation for future research.

The data-driven models obtained in this chapter are considered rich enough to make a fair comparison in Chapter 6 with the physics-based model of the Peltier-based setup from Chapter 3.

6 Comparison physics-based and data-driven model

This chapter compares the resulting SD-MISO models, i.e. the data-driven models with Peltier current and ambient temperature as input, obtained in Chapter 5 with the physics-based model from Chapter 3 on several aspects. Firstly, in Section 6.1 the performance in terms of modeling error of both models is discussed. Section 6.2 then elaborates on the model complexity and interpretability of the models. Subsequently, Section 6.3 continues on the practical applicability of both methods. Finally, conclusions are given in Section 6.4.

6.1 Modeling accuracy

Although the methods and training data sets used for the identification of the physics-based model of the Peltier-based setup from Chapter 3, and the SD-MISO models of the Peltier-based setup from Chapter 5.7.1 are dissimilar, both models are designed to describe the Peltier thermodynamics as accurately as possible for a temperature profile, that exhibits a realistic temperature reference for the POIs. Both methods and the training data sets needed for identification are described below.

The physics-based model is a lumped-capacitance model, of which the lump division is depicted in Figure 11, containing linear heat transfer dynamics and the nonlinear Peltier element thermodynamics. The parameters of the physics-based model are estimated in a couple of steps. Firstly, as explained in Sections 4.1.2 and 4.1.3 of [39], the temperature-dependent model parameters S_M , K_M , and R_M , describing the Peltier element thermodynamics, are determined with the dedicated setup provided in Figure 12. This is done by either using a stairs signal, exciting transient thermodynamics and by allowing the output to settle, visualizing steady-state thermodynamics, or a pseudo random binary sequence (PRBS) signal, exciting transient thermodynamics [39]. The choice for either of the two is done based on whether validation needed to be done on high or low frequent signals. After identifying S_M , K_M , and R_M for three different Peltiers, these parameters are averaged for the usage in the physics-based model. Then, following Section 4.2.1 of [39], the linear heat transfer dynamics, described by the thermal capacitances of the lumps, and the thermal resistances between the lumps, are calculated.

The SD-MISO model is a data-driven model, and is constructed according to the methods described in Section 5.7.1. A set of 4 experiments, accumulating 3 steady-state periods of input-output data is done. Using a separate set of experiments, a nonparametric linear model from T_{amb} to T_{POI} is estimated. In these experiments the ambient temperature and the temperature at the POI are measured, without exciting the Peltier element. The nonparametric BLA from T_{amb} to T_{POI} is estimated following the methods described in Section 4.3.1 for both Peltier 1 and 2. The found nonparametric BLA from T_{amb} to T_{POI} now is used to filter the measured ambient temperature during the MS experiments. Then, the filtered T_{amb} is deducted from the original output T_{POI} . Next, a nonparametric Best Linear Approximation $\hat{\mathbf{G}}_{\text{BLA}}$ and its sample variance $\hat{\sigma}_{\text{BLA}}^2$ are determined. Using the BLA and its sample variance, a linear model is estimated using the frequency domain subspace algorithm from [25] while employing the sample covariance matrix instead of the true covariance [35], by minimizing a weighted least-squares cost function with respect to all model parameters. Afterwards, a nonlinear model is estimated by again minimizing a weighted least-squares cost

function with respect to all model parameters, starting from the linear matrices acquired in 4.3.3. Zero initial values are considered for nonlinear coefficients. This results in a model with the structure as defined in (128).

Despite the difference in methods and training data, the common purpose for both models is the goal to describe the Peltier thermodynamics as accurately as possible for a temperature profile, that exhibits a realistic temperature reference for the POIs. This will therefore be used as main point of comparison for the two identification methods.

As described in Section 2.1, the data-driven models are obtained for L100 Peltiers, while for the identification of the physics-based model TEC-[39] Peltiers are used. The specifications of both Peltiers are different, meaning that employing a certain current profile to both leads to nonidentical temperature outputs. This means it is not possible to fairly compare the two models directly. Therefore, a non-identical but equivalent current profile has been used for both models, where both profiles result in a typical temperature profile for the Peltier to follow when used in handheld devices like in [18], and cover most of the operating temperature range.

To compare the performance of both the physics-based and the SD-MISO models, the errors for these validation temperature profiles are compared. Figure 54 depicts the experimental output $y_{\text{test,PB}}$, and modeled output $y_{\text{test,PB,NL}}$ for the temperature profile and corresponding error $e_{\text{test,PB}}$ for the physics-based model. Figure 55 provides the experimental output $y_{\text{test,DD}}$, and modeled output $y_{\text{test,DD,NL}}$ for the temperature profile and corresponding error $e_{\text{test,DD}}$ for the SD-MISO models for the temperature profiles for Peltier 1 and Peltier 2 respectively.

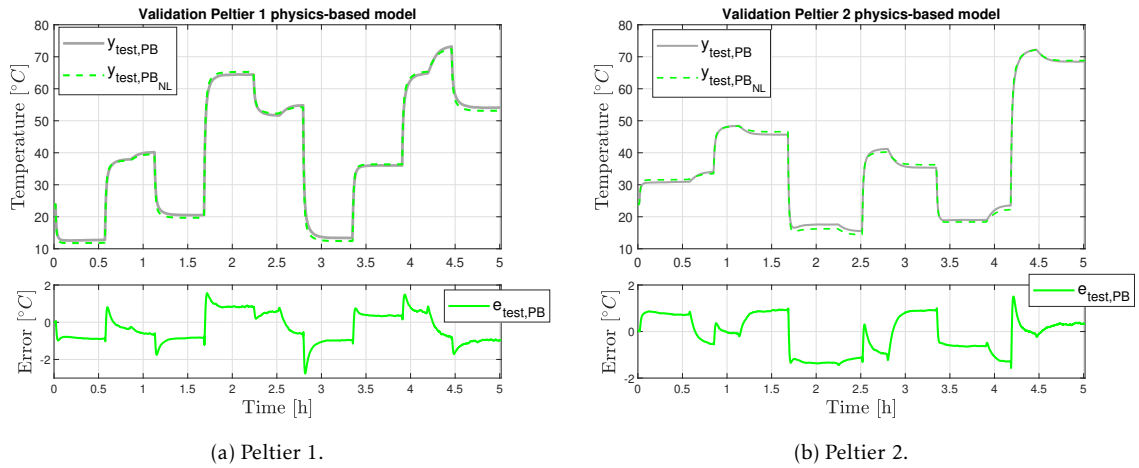


Figure 54: Validation on temperature profile for the physics-based model for both Peltiers. The top part shows the experimental output (solid), model output (dashed), and the bottom part shows the corresponding error.

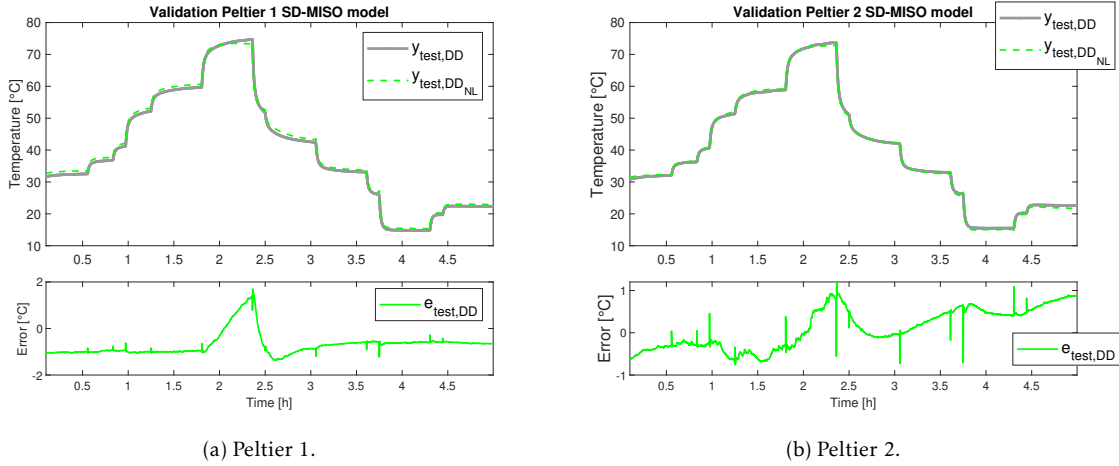


Figure 55: Validation on temperature profile for the SD-MISO model for both Peltiers. The top part shows the experimental output (solid), model output (dashed), and the bottom part shows the corresponding error.

It is clearly visible from in Figures 55a and 55b that for the physics-based model, a zero-mean error profile is produced, while for the data-driven model an offset is present. This might have to do with the fact that the data-driven model does not care about the underlying physics, and solely aims to fit the IO-data as precisely as possible. Table 13 gives the resulting percentual and maximum error for the temperature profiles for the physics-based model and the SD-MISO data-driven models. Observing the resulting errors for the temperature profile, the maximum error for the SD-MISO model for P1 is 1.07 °C lower, and the maximum error for the SD-MISO model for P2 is 0.37 °C lower when compared to the physics-based model. Also, the percentual errors for the SD-MISO models for both Peltiers are lower, indicating that the overall error margins over the validation profile are lower as well. It can therefore be concluded that the SD-MISO models outperform the physics-based model in terms of accuracy. The decrease in modeling error might be due to the fact that the only goal of the SD-MISO model is to capture the IO-thermodynamics as accurately as possible, while maintaining a minimal number of parameters. It does not care about describing the underlying physics correctly. Furthermore, since the discretization of the physics-based model is suboptimal to describe the thermodynamics that create temperature gradients over the stainless steel bottom plates [39], the underlying physics cannot be described more accurately by the physics-based model, without extending its dimensions.

P1	Validation data	
	%	Max [°C]
PB	4.03	2.76
SD-MISO	2.80	1.69

(a) Peltier 1.

P2	Validation data	
	%	Max [°C]
PB	4.63	1.57
SD-MISO	2.76	1.20

(b) Peltier 2.

Table 13: Error margins for both the physics-based and the SD-MISO data-driven models for the temperature profile for both Peltiers.

6.2 Model robustness & interpretability models

For the model of the Peltier-based setup to be of use in practice, it needs to be robust with respect to the ambient temperature. This way, TECs can be used in any type of environment, within the Peltier boundaries. Also, it is convenient if the modeling approach allows easy adaptation between different types of Peltier elements. This way, the identification of the Peltier-based setup is valuable in the sense that it can be applied for a broader range of applications. Furthermore, it is dependent on the goal of the model, whether it may be needed to be interpretable in terms of states. For example, when the underlying nonlinear thermodynamics of any TEC are to be analyzed, to obtain more insight in the underlying physical phenomena. Therefore, the robustness of both physics-based and SD-MISO data-driven models with respect to T_{amb} and changes in Peltier parameters are investigated. Finally, the interpretability of the models is discussed.

The physics-based model is constructed by describing the thermodynamics in the experimental setup. Every state in the model represents a temperature of a position on the actual setup, meaning that the model is fully interpretable in terms of states. The ambient temperature is considered a non-controllable input in the physics-based model. This way, the robustness with respect to T_{amb} is guaranteed, although the interaction between T_{amb} and the setup cannot be calibrated. Furthermore, when a physics-based modeling approach is to be used for a different TEC, the temperature-dependent model parameters S_M , K_M , and R_M , describing the Peltier element thermodynamics, need to be determined with the dedicated setup provided in Figure 12. Most of the thermal resistances of the setup do not change, and can therefore be utilized in the identification of the setup with a different TEC. The contact resistance for a different Peltier can differ, and should therefore be recalibrated. The physics-based modeling approach therefore is easily adaptable to different types of Peltiers. Also an average for the parameters can be used to make it more robust for product to product variations.

The SD-MISO data-driven models are identified using IO-data, combined with some physical insights from the physics-based model regarding model structure. No output nonlinearities are considered, and the maximum order of nonlinearities is chosen equal to that of the physics-based model. No further physical insight of the system is used. Although the insight from the physics-based model was available, this is not always the case. A testing procedure [28] can be employed to differentiate between odd and even nonlinearities, which are nonlinear functions of the state and input, acting in odd and even frequencies respectively. This way, up to which order of nonlinearities needs to be considered in the model structure can be determined, without the insight of the physics-based model. As discussed in Section 5.3.2, the initially determined linear model for P2 has 3 poles, of which two are a complex pole pair. This indicates that the method does indeed neither care about symmetry in the setup, nor about the underlying physics, since for an open-loop thermal system, only real poles are expected. Furthermore, as explained in Section 5.5, a feedthrough term in the model structure of the Peltier-based setup is considered because of modeling freedom, while this is physically impossible. Since the only goal for the SD-MISO models is to obtain an optimal fit for the IO-data, the knowledge on the behavior of the actual Peltier-based setup is not obtained. Therefore, the states of the SD-MISO models are noninterpretable. Using a separately identified model for the ambient temperature to the output temperature,

the robustness with respect to T_{amb} is guaranteed, as proven in the offline experiments in Section 5.7.2. However, this is only possible if the frequency content of the separate experiments for the ambient temperature to the output is rich enough to catch the thermodynamics properly, which is difficult to influence. In terms of applicability to identify different TECs, the data-driven approach cannot reuse any of the found model parameters, since its only goal is to catch the IO-data in an optimal fashion. Applying the methods for a different Peltier means that the identification procedure has to be redone completely. Assuming that the type of Peltier does not result in a major change of underlying thermodynamics means that the model structure can be maintained identical. From the results for the SD-MISO models, it can be observed that the identification of two Peltiers of the same type does not result in resembling models. However, as indicated in Section 5.3.2, the assumed symmetry of the setup might not necessarily be true. It is therefore unclear whether data-driven identification techniques are robust with respect to product to product variations, and it is recommended for future research in order to draw any final conclusions on it.

Altogether, for the SD-MISO data-driven models the IO-behavior is described more accurately, while the knowledge on the underlying behavior of the system is lost. Both methods are robust with respect to the ambient temperature, although the interaction between T_{amb} and the setup cannot be calibrated. It is dependent on the goal of the model, whether it may be needed to be interpretable in terms of states. For example, when the underlying nonlinear thermodynamics of any TEC are to be analyzed, to obtain more insight in the underlying physical phenomena, a physics-based modeling approach is needed. If the goal is purely to describe the IO-thermodynamics as accurately as possible, while maintaining a minimal amount of modeling parameters, the SD-MISO data-driven models should be considered, since these outperform the physics-based model in terms of error margins.

6.3 Practicability methods

One of the requirements for a modeling approach to be of use in practice, is that it should be feasible to identify a model in a limited time, while capturing the thermodynamics properly. Therefore, now the practical applicability of both methods is compared. This is done in terms of possibility for controller / observer design in Section 6.3.1, and modeling effort in Section 6.3.2.

6.3.1 Possibility for controller / observer design

It is very common for a sensor location to not coincide precisely with the actual point of interest, as is the case for the Peltier-based setup. Therefore, observer design is very useful. A nonlinear observer has been designed for the physics-based model, and since the states are actual temperatures of parts of the setup, the knowledge of the states can be used for the observer. Furthermore, for the physics-based model, feedback linearization is applied, transforming the nonlinear thermodynamics into linear input-output thermodynamics [20].

Since the data-driven model has noninterpretable states, state information cannot be used to describe the output at the POI in any logical way. In order to be able to design a nonlinear observer for the data-driven model properly, more research needs to be conducted in this

direction. The same holds for possible feedback linearization controller design.

6.3.2 Modeling effort

The temperature-dependent Peltier parameters of the physics-based model, S_M , R_M , and K_M , are identified by either using a stairs signal, exciting transient thermodynamics and by allowing the output to settle, visualizing steady-state thermodynamics, or a pseudo random binary sequence (PRBS) signal, exciting transient thermodynamics [39]. The choice for either of the two is done based on whether validation needed to be done on high or low frequent signals. Using the dedicated experimental setup from Figure 12, the temperature-dependent parameters for a single Peltier are determined. Using either the stairs experiment or the PRBS experiment, both taking 10 hours to complete, results in a total time needed for identification of the temperature dependent parameters of a Peltier of 10 hours. Afterwards, either the stairs or the PRBS experiment are done for the Peltier-based setup, therewith determining the thermal resistances of the physics-based model, again taking 10 hours. Finally, validation is done with a 5 hour experiment, resulting in a total experimental time of 25 hours per Peltier. However, if a new (type of) TEC would need to be modeled using the physics-based model, the two experiments with the dedicated test setup of Figure 12 plus validation would suffice, therefore reducing the total needed experimental time to 15 hours per Peltier. The experiments used for identification of the temperature-dependent parameters for the physics-based model could be tuned, and time needed could be reduced, to accelerate the identification process.

For the SD-MISO data-driven models, an experiment set consisting of 4 realizations is done, each consisting of 4 periods, of which 3 periods are steady-state. Each period takes 6750 seconds. To get a proper validation done for the carefully designed excitation signals, one of the realizations is chosen as validation realization. The final steady-state period of this realization is used to validate the model. Furthermore, validation is done with a 5 hour experiment, resulting in a total experimental time of 35 hours per Peltier. To identify a new (type of) TEC with a data-driven model, less experimental time would be needed, since the extra realization to validate is not necessary. This results in a total needed experimental time of 27.5 hours. Again, the experiments used for data-driven identification could be tuned, and time needed could be reduced, to accelerate the identification process. For example, it would be interesting to investigate if two periods in steady-state also suffice to describe the Peltier-based setup properly, therewith reducing the experimental time needed.

In terms of constructing a model, for the physics-based modeling approach, a lumped-mass model has to be constructed. For the data-driven modeling approach, the time spent on constructing the model is very little, due to the modeling freedom and no desire to describe the underlying physics properly. The experimental time of the data-driven approach might be higher, but the time spent on constructing the model is higher for the physics-based modeling approach. On the other hand, in most cases a model has been created during the design process of the system considered, which would greatly reduce the time spent on modeling again.

In thermal control, physics-based modeling is preferred because of project risk reduction,

the explainability, and tunability of these models. The found SD-MISO models for the Peltier-based setup are more accurate than the physics-based model, and are easily adaptable to different TECs to be identified. Furthermore, the influence of the ambient temperature is incorporated appropriately. Although the SD-MISO approach would benefit from a shorter experimental time needed, the time spent on modeling is significantly lower than for the physics-based modeling approach, whereas for the physics-based approach in most cases a model is already available through the design process of the considered system. The applicability for controller or observer design for these models still is to be investigated more thoroughly. Therefore, a data-driven modeling approach definitely can be beneficial for the identification of a thermal system, if the goal is to obtain its IO-thermodynamics as accurately as possible, while maintaining a minimal amount of parameters. More research is needed to draw any conclusions in terms of applicability for controller or observer design.

6.4 Conclusion

Concluding, the data-driven models for both Peltiers outperform the physics-based model in terms of accuracy. The maximum error for P1 is 1.07 °C lower, and the maximum error for P2 is 0.37 °C lower when compared to the physics-based model. Also, both models are robust to changes in ambient temperature.

If the goal of a model is to describe the IO-thermodynamics as accurately as possible, while maintaining a minimal amount of modeling parameters, the SD-MISO data-driven models outperform the physics-based model in terms of error margins. To describe the underlying behavior of any type of TEC or thermal system, a physics-based modeling approach should be considered.

Observer and controller design for the physics-based model have successfully been done in the past. Since the data-driven model has noninterpretable states, state information cannot be utilized. In order to design a nonlinear observer for the data-driven model properly, more research needs to be conducted in this direction. The same holds for possible feedback linearization controller design.

The total time needed to obtain experimental data to identify a new TEC is higher for the data-driven model, but the time spent on modeling is significantly lower than for the physics-based modeling approach. It would be interesting to research the modeling accuracy that can be obtained when the data-driven model only uses two realizations, since this would again greatly reduce the time needed for experiments.

A data-driven modeling approach definitely can be beneficial for the identification of a thermal system, if the goal is to obtain its IO-thermodynamics as accurately as possible, while maintaining a minimal amount of parameters. More research is needed to draw any conclusions in terms of applicability for controller or observer design.

7 Conclusion & recommendations for future research

7.1 Conclusions

The objective of this research is to investigate to what extent nonlinear data-driven identification can aid with the identification and control of a Peltier-based setup. The objective is fulfilled in a couple of steps.

7.1.1 Obtain the most accurate physics-based & data-driven model, while maintaining a minimal amount of modeling parameters

Firstly, by performing an in-depth analysis on the contribution of the Thomson effect, the most accurate physics-based model is obtained, while maintaining a minimal amount of parameters. It is observed that the Thomson effect was already incorporated in the model, and therefore no better results in terms of better correlation between model and measurements are obtained. Also, sensitivity analyses have been done to validate the model parameter calibration. This validation showed that the determination and optimization of the temperature dependent parameters S_M , R_M , and K_M has been done adequately.

Then, the most accurate data-driven model is obtained, while maintaining a minimal amount of parameters. A set of four random-phase multisine experiments is conducted, accumulating three steady-state periods of input-output data. By identifying a separate nonparametric model from the ambient temperature T_{amb} to the temperature at the point of interest T_{POI} , and using the found nonparametric best linear approximation from T_{amb} to T_{POI} to filter the measured ambient temperature during the MS experiments, the effect of the ambient temperature is incorporated. Next, the filtered T_{amb} is deducted from the original output T_{POI} , and a MISO identification is done, in the sense that the ambient temperature is considered an input as well. The resulting models have proper knowledge of T_{amb} and are therefore considered robust to changes in T_{amb} . The robustness with respect to changes in T_{amb} of this approach has been investigated on a set of offline experiments, which establishes the correct estimation of the effect of the ambient temperature on the model output.

7.1.2 Comparison physics-based & data-driven models

Accuracy & robustness

Despite the difference in methods and training data, the common purpose for both models is the goal to describe the Peltier thermodynamics as accurately as possible for a temperature profile, that exhibits a realistic temperature reference for the POIs and is therefore used as main point of comparison for the two identification methods. To compare the performance of both the physics-based and the final data-driven models, SD-MISO models, the errors for these validation temperature profiles are compared. Observing the resulting errors for the temperature profile, the maximum error for the SD-MISO model for P1 is 1.07 °C lower, and the maximum error for the SD-MISO model for P2 is 0.37 °C lower when compared to the physics-based model. Also, the percentual errors for the SD-MISO models for both Peltiers are lower, indicating that the overall error margins over the validation profile are lower as well.

The input-output behavior is described more accurately for the final SD-MISO models, while the knowledge on the underlying behavior of the system is lost. Both methods are robust with respect to the ambient temperature, although the interaction between T_{amb} and the setup cannot be calibrated. If the goal is purely to describe the IO-thermodynamics as accurately as possible, while maintaining a minimal amount of modeling parameters, the SD-MISO data-driven models should be considered, since these outperform the physics-based model in terms of error margins.

Model complexity & method practicability

In thermal control, physics-based modeling is preferred because of project risk reduction, the explainability, and tunability of these models. The found SD-MISO models for the Peltier-based setup are more accurate than the physics-based model, and is easily adaptable to different thermoelectric coolers to be identified. Furthermore, the influence of the ambient temperature is incorporated appropriately. Although the SD-MISO approach would benefit from a shorter experimental time needed, the time spent on modeling is significantly lower than for the physics-based modeling approach. The applicability for controller or observer design for these models still needs to be investigated more thoroughly. Therefore, a data-driven modeling approach definitely can be beneficial for the identification of a thermal system, if the goal is to obtain its IO-thermodynamics as accurately as possible, while maintaining a minimal amount of parameters.

7.2 Recommendations

For future research on Peltier-based systems it is recommended to include the following recommendations.

- R₁** Investigate the mismatch in amplifier behavior in order to use the setup to its full extent. That way, also a data-driven MIMO model of the whole setup can be obtained, instead of two separate SISO or MISO models.
- R₂** Adapt the model structure for the data-driven identification to one without a feedthrough term. This way, the model describes the underlying physics of the setup more accurately.
- R₃** If it is desired to research the effect of T_{amb} more thoroughly, adapt the Peltier-based setup to obtain control over the ambient temperature. That way, a true MISO identification could be done by designing multisines for the ambient temperature as well.
- R₄** Investigate whether data-driven models are applicable for observer and/or controller design.

References

- [1] Adamson, W.L. (1965). The effects of the Thomson coefficient and variable resistivity on thermoelectric heat pump performance. *Master Thesis, Georgia Institute of Technology*.
- [2] Bristol, E.H. (1966). On a new measure of interaction for multivariable process control, *IEEE Transactions on Automatic Control*, Vol. 11, p. 133–134.
- [3] Brus, L., and Zambrano, D. (2010). Black-box identification of solar collector dynamics with variant time delay. *Control Engineering Practice*, Vol. 10, p. 1133-1146.
- [4] Bos, K., Heck, D., Heertjes, M., and Kall van der, R (2018). IO Linearization, Stability, and Control of an Input Non-Affine Thermoelectric System. *Annual American Control Conference*, p. 526-528.
- [5] Chavez, J.A., Ortega, J.A., Salazar, J., Turo, A., and Garcia, M.J. (2000). Spice model of thermoelectric elements including thermal effects. *IEEE Instrumentation and Measurement Technology*, Vol. 2, p. 1019-1023.
- [6] Chen, J., Zijun, Y., and Liqing, W. (1996). The influence of Thomson effect on the maximum power output and maximum efficiency of a thermoelectric generator. *Journal of Applied Physics*, Vol. 79, p. 8823-8828.
- [7] Chen, J. (2013). Thermal controller design for a lab-on-chip benchmark. *Master thesis, Eindhoven University of Technology*.
- [8] D’haene, T., Pintelon, R., and Guillaume, P. (2007). Stable Approximations of Unstable Models. *Proceedings of the IEEE Instrumentation and Measurement Technology Conference, Warsaw, Poland*, p. 1-6.
- [9] Farnell, An Avnet Company (2020). Thermoelectric Peltier Cooler Module. Retrieved from <https://nl.farnell.com/multicomp-pro/mpeth-127-14-25-s-h1/peltier-module-39w-40-x-40-x-4/dp/3267527?st=peltier>
- [10] Fraisse, G., Ramousse, J., Sgorlon, D., and Goupil, C. (2013). Comparison of different modeling approaches for thermoelectric elements. *Energy conversion and Management*, Vol. 65, p. 351-356.
- [11] Gils van, R. (2017). Practical thermal control by thermo-electric actuators. *23rd International Workshop on Thermal Investigations of ICs and Systems (THERMINIC)*, p. 1-6.
- [12] Guiatni, M., Drif, A., and Kheddar, A. (2007). Thermoelectric modules: Recursive non-linear ARMA modeling, identification and robust control. *The 33rd Annual Conference of the IECON*, p. 568-573.
- [13] Hodes, M. (2005). On one-dimensional analysis of thermoelectric modules (TEMs). *IEEE Transactions on Components and Packaging Technologies*, Vol. 28, p. 307-317.
- [14] Hodes, M. (2010). Optimal pellet geometries for thermoelectric power generation. *IEEE Transactions on Components and Packaging Technologies*, Vol. 33, p.307-317.

- [15] Huang, M., Yen, R., and Wang, A. (2005). The influence of the Thomson effect on the performance of a thermoelectric cooler. *International Journal of Heat and Mass Transfer*, Vol. 48, p. 413-418.
- [16] Incropera, F.P., Dewitt, D.P., Bergman, T. L., and Lavine, A.S. (2007). Fundamentals of Heat and Mass Transfer. *John Wiley & Sons*.
- [17] Ioffe A.F. (1957). Semiconductor thermoelements and thermoelectric cooling. *Infosearch*.
- [18] Jiang, J., Kaigala, G.V., Marquez, H.J., and Backhouse, C.J. (2012). Nonlinear Controller Designs for Thermal Management in PCR Amplification. *IEEE Transactions on Control Systems Technology*, Vol. 20, p. 11-30.
- [19] Kaya, M. (2006). Experimental study on active cooling system used for thermal management of high-power multichip light-emitting diodes. *Nature*, Vol. 442, p. 412-418.
- [20] Khalil, H.K. (2002). Nonlinear systems. *Pearson*.
- [21] Khandurina, J., McKnight, T., Jacobsen, S., Waters, L., Foote R., and Ramsey J. (2000). Integrated system for rapid PCR-based DNA analysis in microfluidic devices. *Analytical Chemistry*, Vol. 72, p. 2995–3000.
- [22] Levenberg, K. (1944). A method for the solution of certain problems in least squares. *Quarterly of Applied Mathematics*, Vol. 2, p. 164-168.
- [23] Luo, Z. (2008). A simple method to estimate the physical characteristics of a thermoelectric cooler from vendor datasheets. *Electron Cooling*, p. 22-27.
- [24] Marquardt, D. (1963). An algorithm for least-squares estimation of nonlinear parameters. *SIAM Journal of Applied Mathematics*, Vol. 11, 431-441.
- [25] McKelvey, T., Akçay, H., and Ljung, L. (1996). Subspace-based multivariable system identification from frequency response data. *IEEE Transactions on Automatic Control*, Vol. 41, Issue 7, p. 960–979.
- [26] Mills, A.F. (1992). Heat transfer. *CRC Press*.
- [27] Mitrani, D., Tome, J.A., Salazar, J., Turo, A., Garcia, J., and Chavez, J.A. (2004). Methodology for extracting thermoelectric module parameters. *IMTC 2004*, p. 564-568.
- [28] Noël, J.P., Esfahani, A.F., Kerschen, G., and Schoukens, J. (2017). A nonlinear state-space approach to hysteresis identification. *Mechanical Systems and Signal Processing*, Vol. 84, p. 171-184.
- [29] Noël, J.P., and Schoukens, J. (2018). Grey-box state-space identification of nonlinear mechanical vibrations. *International Journal of Control*, Vol. 91, p. 1118-1139.
- [30] Paduart, J. (2007). Identification of nonlinear systems using Polynomial Nonlinear State Space models. *PhD Thesis, Vrije Universiteit Brussel*.

- [31] Paduart, J., Lauwers, L., Swevers, J., Smolders, K., Schoukens, J., and Pintelon, R. (2010). Identification of nonlinear systems using Polynomial Nonlinear State Space models. *Automatica*, Vol. 46, p. 647-656.
- [32] Pettes, A., Hodes, M., and Goodson, K. (2009). Optimized thermoelectric refrigeration in the presence of thermal boundary resistance. *IEEE Transactions on advanced packaging*, Vol. 32, p. 423-430.
- [33] Pintelas E., Livieris I.E., Pintelas P. (2020). A Grey-Box Ensemble Model Exploiting Black-Box Accuracy and White-Box Intrinsic Interpretability. *Algorithms*. Vol. 13 Issue 1.
- [34] Pintelon, R., Schoukens, J. (2001). System Identification: A Frequency Domain Approach. *IEEE Press*.
- [35] Pintelon, R.(2002). Frequency-domain subspace system identification using non-parametric noise models, *Automatica*, Vol. 38, p. 1295–1311.
- [36] Schoukens, J., Pintelon, R., Rolain, Y. (2012). Mastering System Identification in 100 Exercises. *IEEE Press*.
- [37] Relan, R., Vanbeylen, L., Firouz, Y., and Schoukens, J. (2015). Characterization and nonlinear modelling of Li-ion battery. *Proceedings of the 34th Benelux Meeting on Systems and Control*.
- [38] Shao, H., Yang, Z., and Yu, Y. (2014). LPV model-based temperature control of thermoelectric device. *ICMC*, Vol. 6, p. 1012-1017.
- [39] Slenders, R. (2020). Identification and control of a Peltier-based setup. *Master thesis, Eindhoven University of Technology*.
- [40] Steinhart, J.S., and Hart, S.R. (1968). Calibration curves for thermistors. *Deep Sea Research and Oceanographic Abstracts*, Vol. 15, p. 497-503.
- [41] Székely, V., Nagy, A., Torok, S., Hajas, G., and Rencz, M. (2000). Realization of an electronically controlled thermal resistance. *Microelectronics Journal*, Vol. 31, p. 811-814.
- [42] Székely, V., Torok, S., Kollar, E. (2007). Improvements of the variable thermal resistance. *13th Thermionic International workshop*.
- [43] Xie, L., and Ljung, L. (2002). Estimate Physical Parameters by Black-Box Modeling. *Chinese Control Conference*, p. 673-677.
- [44] Yager, P., Edwards, T., Fu, E., Helton, K., Nelson, K., Tam, M., and Weigl, B. (2006). Microfluidic diagnostic technologies for global public health. *Nature*, Vol. 442, p. 412-418.
- [45] Yamashita, O. (2008). Effect of temperature dependence of electrical resistivity on the cooling performance of a single thermoelectric element. *Applied Energy*, Vol. 85, p. 1002-1014.

- [46] Yamashita, O. (2009). Effect of linear and nonlinear components in the temperature dependences of thermoelectric properties on the cooling performance. *Applied Energy*, Vol. 86, p. 1746-1756.
- [47] Zhang, C., Xu, J., Ma, W., and Zheng, W. (2006). PCR microfluidic devices for DNA amplification. *Biotechnology advances*, Vol. 24, p. 243-284.
- [48] Zhang, R., Brooks, D., Hodes, M., and Manno, V. (2012). Optimized thermoelectric module-heat sink assemblies for precision temperature control. *Journal of Electronic Packaging*, Vol. 134.

Appendices

A Sensitivity analysis physics-based modeling parameters

The sensitivity of the temperature dependent parameters is obtained by calculating the Jacobian from the output temperatures w.r.t. S_M , K_M , and R_M . The Jacobian is a matrix with the derivative of the temperature T_1 to T_4 with respect to the parameters S_M , K_M , and R_M . As such the matrix has 4 rows and three columns. The elements of the matrix are given by $J_{ij} = \frac{dT_i}{dx_j}$, with $i \in \{1, 2, 3, 4\}$, $x = [S_m \ R_m \ K_m]$, and $j \in \{1, 2, 3\}$. The output temperatures correspond to the indicated positions in Figure 12.

The Jacobian is obtained in two steps. Firstly, a simulation with the originally obtained parameters S_m , R_m , and K_m is done to obtain T_{1-4} , which can be seen in Figure 56.

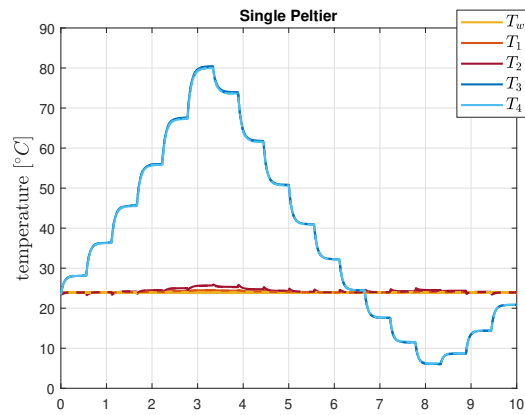
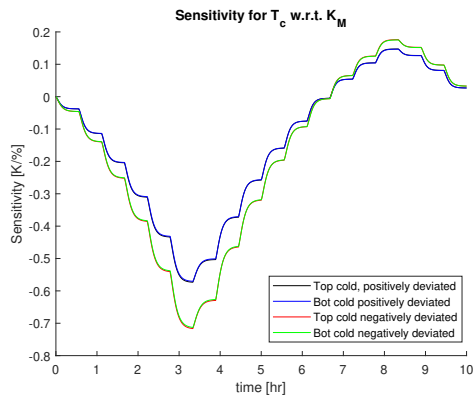
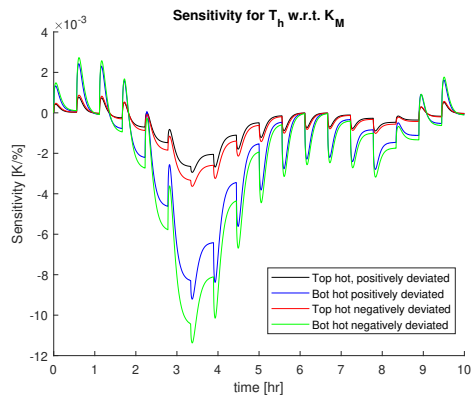


Figure 56: Simulated output with original parameters.

Then, the parameters S_m , R_m , and K_m are deviated by 10%, after which the same experiment is simulated again to obtain the new values for T_{1-4} . Then, the Jacobian is computed. This has been done deviating all parameters in x separately, as well as for deviating the combinations of the parameters. The resulting figures for the sensitivity of T_{1-4} w.r.t. S_m , R_m , and K_m of Peltier 1 can be found in Figures 57-59.

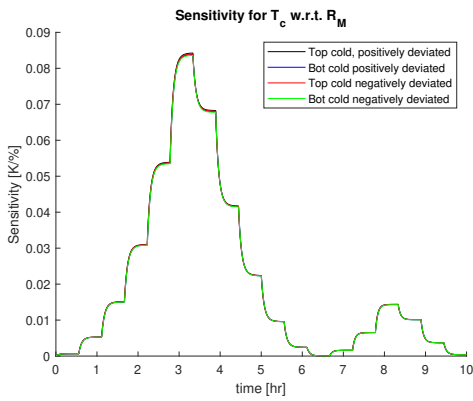


(a) Sensitivity analysis w.r.t. K_M for T_c .

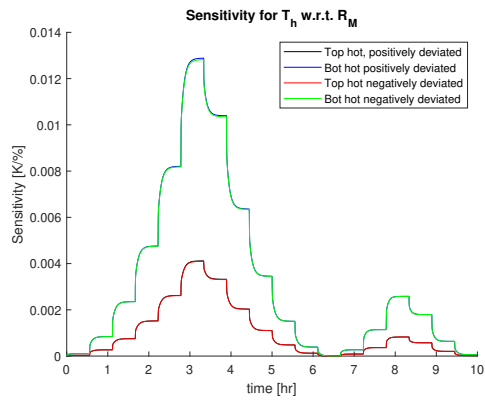


(b) Sensitivity analysis w.r.t. K_M for T_h .

Figure 57: Sensitivity analysis w.r.t. K_M for Peltier 1.

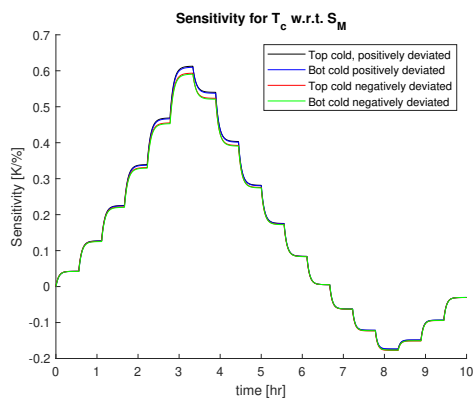


(a) Sensitivity analysis w.r.t. R_M for T_c .

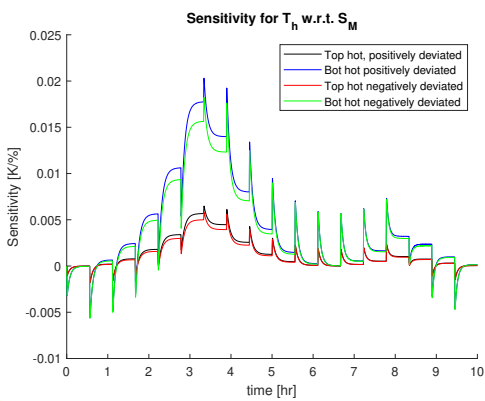


(b) Sensitivity analysis w.r.t. R_M for T_h .

Figure 58: Sensitivity analysis w.r.t. R_M for Peltier 1.



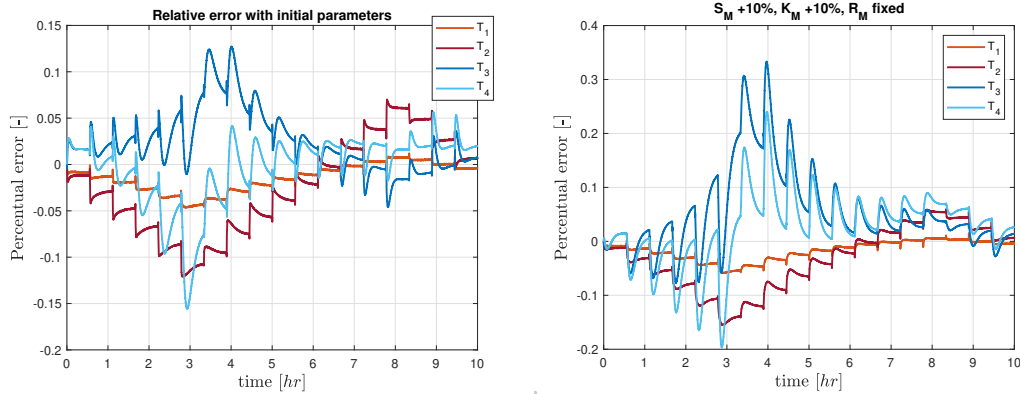
(a) Sensitivity analysis w.r.t. S_M for T_c .



(b) Sensitivity analysis w.r.t. S_M for T_h .

Figure 59: Sensitivity analysis w.r.t. S_M for Peltier 1.

As can be seen, the Jacobian for both S_M and K_M strongly correlate. This might denote multicollinearity. The combination S_M & K_M both being off by 10% might lead to compensation in the output. If both S_M and K_M are deviated by 10%, the error with respect to the experimental data is larger than the error for the original settings with respect to the experimental data, as can be seen in Figure 60.



(a) Error of simulated model with original parameters identified in [39]. (b) Error of simulated model with deviated parameters based on sensitivity analysis.

Figure 60: Error of simulated model for both original and deviated parameters for sensitivity analysis.

The sensitivity analysis shows that calibration of the parameters S_M , K_M , and R_M has been done adequately. The output of the experiment is strongly dependent on S_M and K_M being correct, but since S_M is separately identified, for the identified S_M , a fitting K_M can be found by the optimization algorithm. Note, there might be another set of S_M and K_M that is physically incorrect, but fits the IO-data.

B Determination time constant Peltiers

To determine the time-constants of the Peltiers in the Peltier-based setup, a set of simple experiments is done.

B.1 Dominant time constant

The first step to determine the time-constants, is to apply a step is to both Peltiers, after which a measurement of 50 minutes is done. The results can be found in Figure 61.

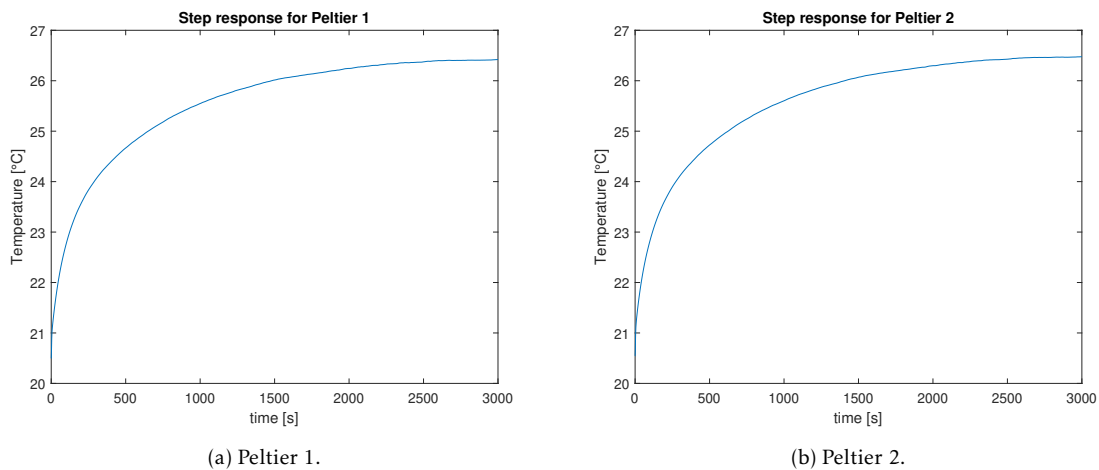


Figure 61: Step response of both Peltiers in the Peltier-based setup.

To determine the desired sampling frequency f_{s_d} , determine the dominant time constant τ_D of the Peltiers in the system. This is done by fitting a first order exponential decay function $y = y_0 + dy \cdot e^{-x/\tau_D}$ to the region of interest, that can be found in Figure 62.

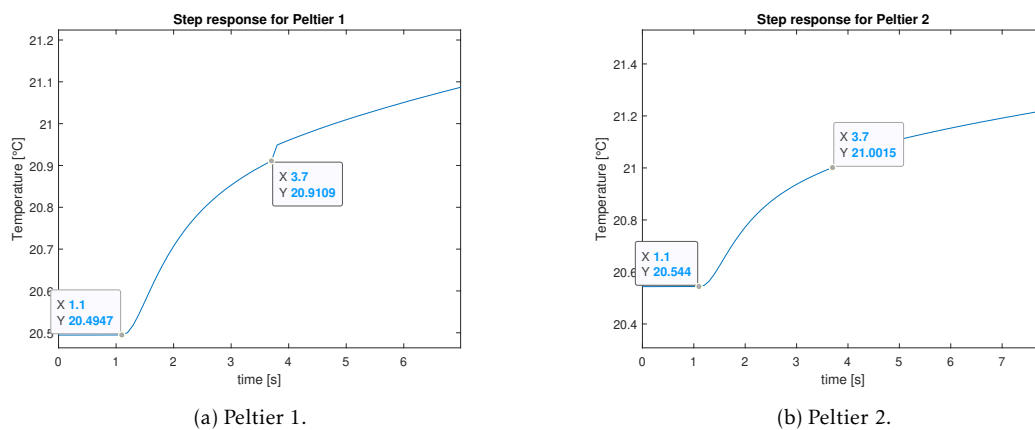


Figure 62: Step response of both Peltiers in the Peltier-based setup, zoomed.

By fitting the first order exponential decay function between $t=1.1$ and $t=3.7$ seconds for

both Peltiers, the resulting values for Peltier 1 and 2 are then given by $\tau_{D_1}=1.4004$ seconds for Peltier 1, and $\tau_{D_2}=1.4305$ seconds for Peltier 2.

The desired sampling frequency f_{s_d} then is determined by:

$$f_{s_d} = \max_i f_{s_d,i} = \max_i \frac{20}{\tau_{F_i} \cdot 2\pi}, \quad (138)$$

with $i \in \{1, 2\}$, resulting in $f_{s_d}=2.273$ Hz.

B.2 Slowest time constant

The slowest time constant τ_s indicates the time required for a thermal system to respond to a change in its ambient temperature. When the ambient temperature is changed from T_1 to T_2 , the relationship between the time elapsed during the temperature change t and the temperature T can be expressed by

$$T = (T_2 - T_1)(1 - e^{-\frac{t}{\tau_s}}) + T_1. \quad (139)$$

Then, assuming t and τ_s are equal, the equation can be expressed as

$$\begin{aligned} T &= (T_2 - T_1)(1 - e^{-1}) + T_1, \\ \frac{T - T_1}{T_2 - T_1} &= 1 - e^{-1} = 0.632, \end{aligned} \quad (140)$$

showing that the constant τ_s is defined as the time for the system to reach 63.2% of the total difference between its initial and final temperature. The slowest time constant τ_s is determined for both Peltiers from Figure 63. This results in $\tau_{S_1}=352$ seconds, and $\tau_{S_2}=350.7$ seconds. Accordingly, τ_s is determined by

$$\tau_s = \max_i \tau_{s_i}, \quad (141)$$

with $i \in \{1, 2\}$ resulting in τ_s of 352 seconds.

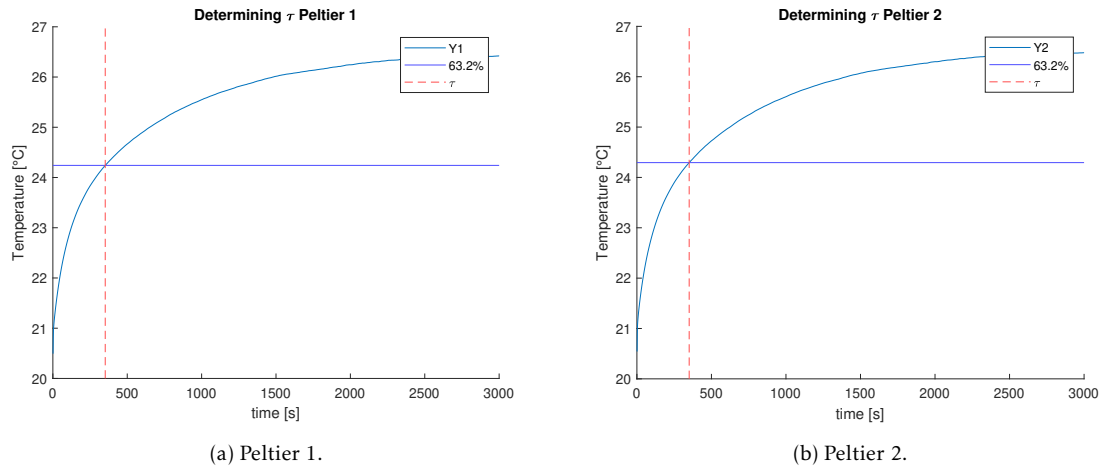


Figure 63: Step responses used to determine slowest time-constants of Peltier 1 and 2.

Declaration concerning the TU/e Code of Scientific Conduct for the Master's thesis

I have read the TU/e Code of Scientific Conductⁱ.

I hereby declare that my Master's thesis has been carried out in accordance with the rules of the TU/e Code of Scientific Conduct

Date

25-01-2021
.....

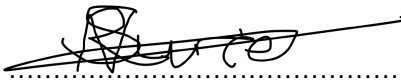
Name

Raoul Surie
.....

ID-number

0810262
.....

Signature


.....

Submit the signed declaration to the student administration of your department.

ⁱ See: <http://www.tue.nl/en/university/about-the-university/integrity/scientific-integrity/>

The Netherlands Code of Conduct for Academic Practice of the VSNU can be found here also.

More information about scientific integrity is published on the websites of TU/e and VSNU